UC Berkeley

UC Berkeley Electronic Theses and Dissertations

Title
Diffusion in SiGe and Ge

Permalink
https://escholarship.org/uc/item/0qj1q0fk

Author
Liao, Christopher Yuan Ting

Publication Date
2010

Peer reviewed|Thesis/dissertation

Diffusion in SiGe and Ge

by

Christopher Yuan-Ting Liao

A dissertation submitted in partial satisfaction of the

requirements for the degree of

Doctor of Philosophy

in

Engineering – Materials Science and Engineering

in the

Graduate Division

of the

University of California, Berkeley

Committee in charge:

Professor Eugene E. Haller, Chair
Professor Oscar D. Dubon
Professor Tsu-Jae King Liu

Fall 2010

Abstract

Diffusion in SiGe and Ge

by

Christopher Yuan-Ting Liao

Doctor of Philosophy in Engineering – Materials Science and Engineering

University of California, Berkeley

Professor Eugene E. Haller, Chair

Diffusion is the most fundamental mass transport process in solids characterized by point defect-diffusing atom interactions. In order to predict diffusion processes of impurities in a solid, the diffusion mechanisms, i.e., interactions between point defects and diffusing species, must be well understood. While the diffusion parameters and mechanisms are well known in silicon, very limited knowledge exists for diffusion parameters and mechanisms for Ge and SiGe alloys. As Ge and SiGe alloys are introduced in the new generations of microelectronic devices, the diffusion behavior in these materials must be studied.

The simultaneous diffusion of As, Si, and Ge in a $Si_{0.95}Ge_{0.05}$ alloy has been studied using a structure with an isotopically enriched SiGe layer. The diffusion in both intrinsic and extrinsic conditions was carried out between 900 to 1180°C. From the numerical fitting of the diffusion profiles, the diffusion mechanisms are determined. The simultaneous As and self-diffusion have been successfully modeled as a combination of the vacancy diffusion mechanism with doubly negatively charged vacancies, the interstitial-assisted mechanism with neutral self-interstitials, and a As_2V clustering process. The diffusion mechanisms are the same as those for As in pure Si except for the clustering process, which is common for donors in pure Ge. The effective equilibrium diffusion pre-exponential factor for As in $Si_{0.95}Ge_{0.05}$ is determined to be 129 cm^2/s while the diffusion activation enthalpy is 4.27 eV. The diffusion parameters for As in this alloy composition are very close to those in pure Si. Future experiments to study As diffusion in different alloy compositions are proposed. In this way, a transition from the As-in-Si-like diffusion mechanism to As-in-Ge-like diffusion mechanism can be identified.

Proton irradiation enhanced B diffusion in Ge has also been studied. The proton irradiation introduces excess self-interstitials which are virtually non-existing under equilibrium conditions. A molecular beam epitaxially grown structure with six B-doped layers was used for the radiation enhanced diffusion studies. We found B diffusion is enhanced by many orders of magnitude under this non-equilibrium condition. The effective B diffusion enthalpy under 2.5 MeV proton irradiation with 1.5 μA beam current is found to be 0.48 eV for temperatures from 400 to 500°C. This effective enthalpy is much lower than the 4.65 eV found under equilibrium conditions. From the radiation enhanced B and self-diffusion experiments, we conclude that the

1

interstitial-mediated diffusion mechanism is dominant under the proton irradiation condition. We can also conclude that B diffusion is indeed driven by self-interstitials under equilibrium conditions. We further propose some future experiments to help identify the exact B diffusion mechanism(s) and the charge states of the B-defect pairs in Ge.

Table of Contents

Acknowledgments

Chapter 1 Introduction

Germanium, discovered in 1886 by Clemens Winkler, was the semiconductor material of choice at the birth of solid-state electronics. The material was used in the first point-contact transistor invented at Bell Labs in 1947 [1]. While the historic importance of germanium cannot be ignored, it quickly gave way to silicon as the semiconductor material used in transistors in the late 50s. The larger bandgap, stable oxide, and lower surface state density of Si proved to be crucial for transistors; hence Si completely replaced Ge in microelectronic devices since the early 60s. Recently, however, Ge with higher charge carrier mobilities has regained vast attention in the Si microelectronics community due to a slowdown in improving Si device performance solely by scaling. In Section 1 of this chapter, the historic role of Ge in transistors will be discussed. Section 2 will address the need to reintroduce Ge into Si-based devices. The importance and the lack of understanding of the diffusion behaviors in silicon-germanium alloys and in germanium will be discussed in Chapter 2.

1.1 History of Ge in transistors

The birth of the multidisciplinary field of materials science, which broadly includes knowledge in metallurgy, physics, and chemistry, can arguably be linked to the invention of solid-state electronics. In 1920s and 1930s, most physicists refused to study solids as they were dominated by impurities. "Physics of dirt," as it was disparagingly called, was not a fit subject for respectable theory [2]. This perspective changed when J. Bardeen and W. Brattain at Bell Labs invented the point-contact transistor in 1947 with a piece of polycrystalline germanium. Shortly after, W. Shockley, also of Bell Labs, created the first junction transistor, made from germanium. The invention of these triodes, solid-state amplifiers, revolutionized modern technologies and started the information age, as it is often called today. In subsequent years, metallurgists, experimental and theoretical physicists, chemists, and electronic experts at Bell Labs and many other places worked tirelessly to improve the understanding of this new field of solid-state electronics. They soon realized that the control of impurities or "dirt" was essential to the electrical properties of the triodes. Hence the idea of understanding and controlling of microstructures in tuning physical materials properties, the central theme of the field of materials science, was developed. Naturally, the material of the focus at that time was germanium, the semiconductor used in the first transistor.

Germanium was discovered in late 19th century. An element called eka-silicon was predicted by D. I. Mendeleev in 1871 as the missing element with atomic weight of 72 between known elements silicon and tin in the group IV column of the table of elements. In 1886, C. A. Winkler discovered the eka-silicon predicted in the silver-rich mineral argyrodite and named it "germanium" in honor of his home country. Since germanium was only found in small portions of some minerals, it was rare and expensive. Due to scarcity of this material, not many applications or scientific findings were established immediately after its discovery. In fact, it was merely known as a poor metal for decades following its discovery [1].

The research on electrical properties of semiconductors did not intensify until World War II. Before the War, the British had pushed secretly the development of rectifying metal-

1

semiconductor diodes to be used as effective high frequency mixers in radio waves and radar technology [3]. Once the WWII broke out in Europe, a high-level decision from the United Kingdom to share their secret knowledge of rectifying semiconductors with the United States led to the creation of the Radiation Laboratory at the Massachusetts Institute of Technology [3]. The Radiation Laboratory became the focal point for all radar related research with other industrial and academic laboratories contribute on different parts of the research, including purification and understanding of silicon and germanium semiconducting crystals. Particularly, the Physics Department at the Purdue University led by its chair, Karl Lark-Horovitz, deserves special mention. In 1942, Lark-Horovitz and colleagues decided to concentrate their work on germanium because he reasoned that the lower melting temperature and smaller chemical reactivity when compared with silicon meant a better chance of purifying germanium to sufficiently low defect concentration levels crucial for high frequency radar applications [1]. Further, the researchers at Purdue focused as much on the fundamental understanding of germanium properties as on its practical rectifying characteristics, differentiating themselves from application-driven studies done in most other laboratories. Lark-Horovitz had the insight that the semiconductor held a great promise for the future of science and technology and wanted to establish a firm fundamental knowledge base as much as possible during the wartime [3]. The work at Purdue eventually paid off, leading to a great number of publications after the war, enhancing fundamental understandings of semiconductors, particularly, of germanium.

For more than a decade, from the end of World War II to the early 60s, germanium had been the material of choice for solid-state electronics. The pioneering work done at Purdue contributed to a large degree to advance the understanding of fundamental properties of germanium; setting it apart from other semiconductors. In fact, the first point-contact transistor invented by Bardeen and Brattain at the Bell Labs at the end of 1947 was built on a piece of polycrystalline germanium obtained from Purdue University [1, 4]. Figure 1 shows the first point-contact transistor from Bell Labs with two cat's whiskers and a piece of poly-germanium. At that early stage, the two fine-point metal contacts pressed on a germanium crystal were mechanically unreliable and were not able to carry large currents. The invention of germanium junction transistor by W. Schockley soon followed and resolved many drawbacks of point-contact transistors [5]. Needless to say, the invention of the solid-state transistors has changed modern day life forever.
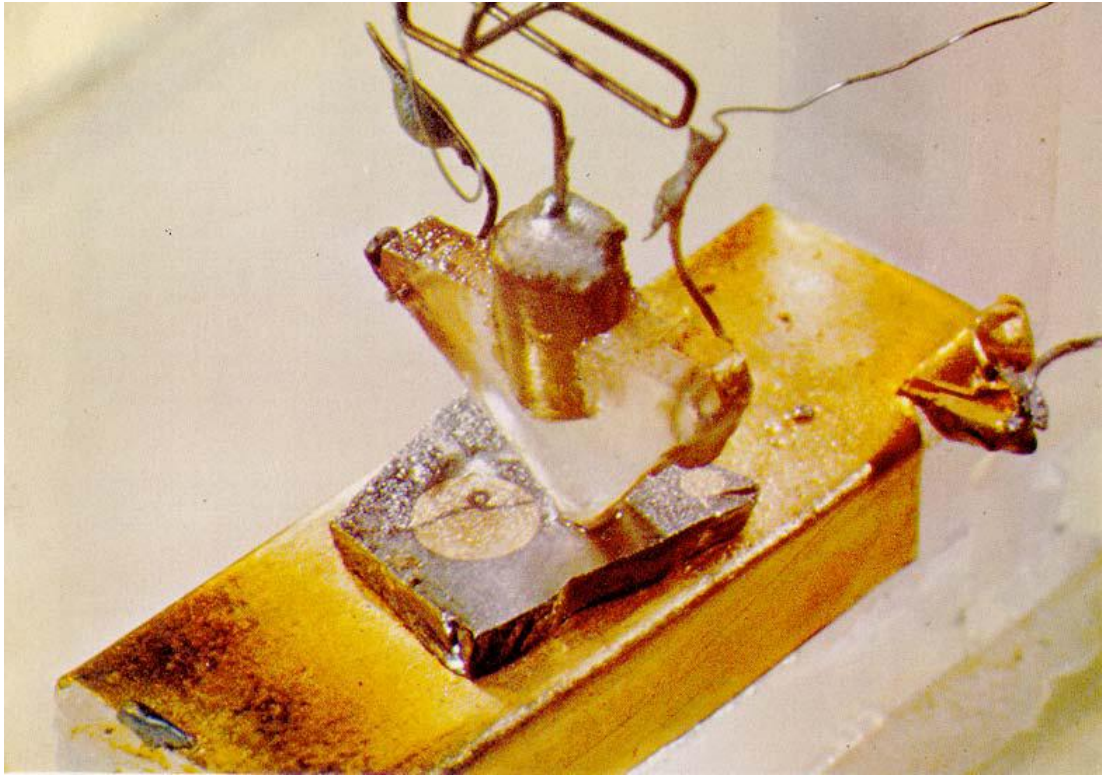
Figure 1.1 First point-contact transistor fabricated by Bardeen and Brattain of Bell Labs on a piece of polycrystalline germanium obtained from Purdue University (from Ref. [1]).

The invention of the transistor started an explosion of research focused on improving germanium materials and transistor properties. Another team of Bell Labs scientists soon realized that the growth of single crystalline germanium was necessary to counter undesirable effects of grain boundaries on charge carriers and, therefore, electrical properties. G. K. Teal and colleagues reported their efforts in using the Czochralski method to grow single crystalline germanium just a few years after the invention of the transistor [6-7]. Many other processing technologies including zone refining, alloying, and diffusion doping were developed during that decade to commercialize germanium solid-state transistors. The crest of germanium-based transistor technology was reached when J. Kilby at Texas Instruments invented the integrated circuit (IC) when he incorporated different electronic components on a single diffused Ge wafer in 1958 [8]. The research focus shifted soon after to silicon and it eventually replaced germanium as the core semiconductor material for transistors.

More desirable properties of silicon make it the dominating material for modern integrated circuit devices. In 1961, R. Noyce at Fairchild Semiconductors was awarded a patent in using silicon dioxide as a natural mask in integrating different circuit components and electric leads on a single silicon chip [9]. Noyce is credited, along with Kilby, as independent inventors of integrated circuits. This stable silicon dioxide turned out to be the game changer for silicon to replace germanium as the core material for the integrated circuit technology. In addition to stable native silicon dioxide, silicon's higher band-gap and lower surface defect states density (and therefore lower leakage current) proved to be superior to germanium for integrated circuit

3

applications. As a result, the research focus has shifted away from germanium to silicon starting in the 60s. Today's IC technology is built predominantly on silicon while germanium mainly finds its use in niche markets such as nuclear radiation detectors, infrared detectors, and substrate for epitaxial growth of III-V photovoltaic cells. Since Ge studies have been virtually abandoned for 40 years, knowledge of many Ge properties is fragmentary. Recently, however, germanium has reentered the mainstream of IC devices because the scaling of silicon-based devices is reaching its limit. Section 1.2 will discuss the details of the reintroduction of germanium in IC devices.

1.2   Reintroduction of germanium in modern devices

Germanium is reintroduced to silicon-based devices to enhance device speed. The silicon-based device industry has been following the Moore's Law since the mid 60s. The phenomenological law, named after one of Intel Corp.'s founder, describes the long term trend of doubling the number of transistors on a single chip in roughly 18-24 months. For the most part, this is achieved by miniaturizing the dimensions of individual silicon transistor. The dimension reduction not only increases the density of transistors per chip, it also increases the transistor speed by reducing the length that the charge carriers have to travel and the capacitance associated with smaller gates. However, reduction in the channel length does not affect the inherent charge carrier transport properties in the channel. More recently, the scalability of silicon-based metal-oxide-semiconductor field effect transistors (MOSFETs) has reached a limit; further scaling does not lead to device performance improvement. This limitation is due to various undesirable effects caused by channel length reduction. Collectively, they are called the short-channel effects and will be discussed qualitatively in Section 1.2.1. More quantitative descriptions can be found in textbooks such as Ref [10]. To counter the adverse short-channel effects on device performance, engineering solutions are developed to increase the inherent carrier mobilities in the channel. One effective solution is to induce strain in the channel. This can be done by incorporating germanium in the source and drain regions of the MOSFET forming an alloy of silicon and germanium which are completely miscible over the entire composition range. Due to the larger lattice parameter of silicon-germanium alloys, the channel is compressively strained. The detail of this strain engineering is discussed in Section 1.2.2. Finally, Section 1.2.3 describes the idea of replacing the silicon channel entirely with higher mobility germanium to further enhance device performance. After idling for 40+ years in the integrated circuit industry, the development of germanium-incorporated devices has once again taken the center stage.

1.2.1   Limitation of scaling and short-channel effects

Silicon-based MOS field effect transistors have proven to be remarkably scalable to sustain Moore's Law in doubling the number of transistors on a chip every 18-24 months. In fact, the intrinsic device performance has improved, on average, about 17% per year up to 130-nm technology node, following an inverse gate-length dependence [11]. The performance improvement is due in part to the reduction of channel length, the actually distance the charge carriers have to travel between source and drain, and many doping innovations such as super-steep retrograde channel doping and highly doped halo around very highly doped source and drain. The reduction in channel length increases source-to-drain current, effectively lowering the

resistance, R, while the reduction in the gate area reduces the capacitance, C. As a result, the RC delay is lowered and the device switches at faster speed. However, the scaling of Si-based devices cannot be sustained without limit. It is generally accepted that beyond the 45-nm technology node, scalability of Si-based MOSFETs can only be continued with very limited gain in device performance even with strain engineering [12]. The limitations are attributed collectively to short-channel effects. To continue the performance improvement of the microelectronic devices, novel transistor structures, such as non-planar FinFET, and novel high mobility channel materials such as germanium are needed [13-14].

As channel length decreases in a MOSFET, a few undesirable effects such as shifts in threshold voltage and an increase in the subthreshold current can be observed. The depletion of channel under the gate in a MOSFET is balanced by charges from three electrodes, the gate, the source, and the drain. Ideally in a long channel device, the depletion of the channel is fully supported by the electric field induced from the charges at the gate. However, in short channel devices, the proportional contributions from source and drain are higher. Since source-body and drain-body are p-n junctions, built-in depletion layers are present even with no applied biases. Worse yet, since source and drain are usually heavily doped to reduce contact resistance, built-in depletion layers are mostly located in the channel. Therefore, proportionally, the control of gate decreases as channel length decreases; less gate charge is needed to reach inversion in the channel. The gate lost its ability to control the device when source depletion and drain depletion merge (i.e. when source depletion + drain depletion = channel length) as channel shrinks. This condition is known as punchthrough and the device is no longer useful as a switch.

The applied drain voltage also reduces the ability for the gate bias to control the channel current flow. The charge carrier flow path in the channel is confined within the narrow inversion layer created by the electric fields in the channel. In the long-channel geometry, this electric field is induced from the applied gate bias. The gate bias needed to overcome the potential barrier of inverting the surface region of the channel is known as the threshold voltage. However, in short-channel geometry, the field from source to drain also plays a role. If the drain to source voltage is increased, the potential barrier for inversion in the channel decreases, leading to drain-induced-barrier-lowering (DIBL). The consequence is that the threshold voltage, the gate voltage needed to turn on a device, becomes dependent on the drain voltage in the short channel dimension. This threshold voltage roll-off can be seen in Figure 1.2, reproduced plotting of the threshold voltage as a function of gate length for different drain voltages. The dependence of the threshold voltage on gate length and on drain voltage are undesirable because inevitable slight variations in device dimensions due to the manufacturing process in millions of transistors on a chip can lead to different threshold voltages and the reliability of the devices will suffer.
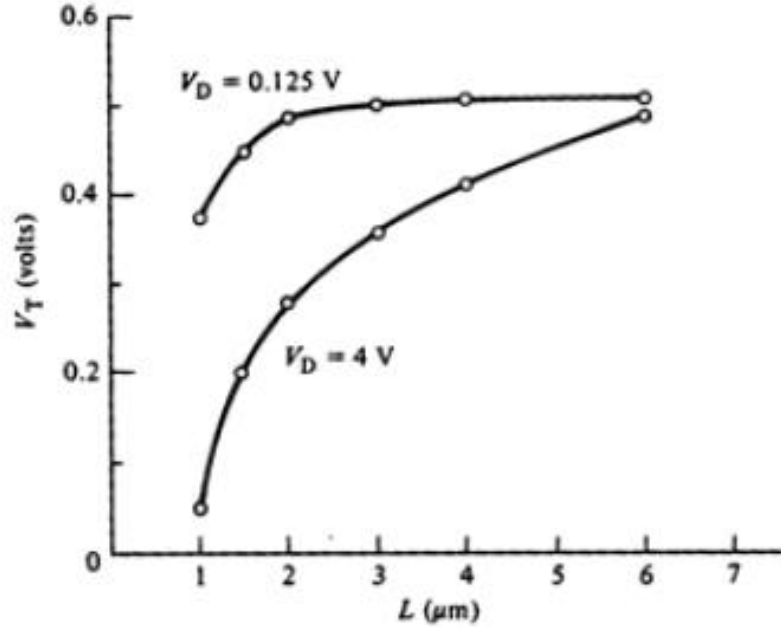
Figure 1.2 Threshold voltage variation as a function of gate length and applied drain voltage (reproduced from ref. [10]).

Shrinking channel length also leads to numerous other detrimental effects due to the large horizontal source to drain electric field. For instance, the large horizontal electric field caused by the short channel distance made the charge carriers reach very high velocity. These energetic charge particles can then ionize silicon lattice atoms and generate electron-hole pairs. As a result, the substrate leakage current is increased. Similarly devastating, high-energy hot electrons can enter and be trapped in the oxide, leading to charge retention in the oxide layer, permanently damaging the dielectric. Essentially, this will limit the lifetime of the device.

Various channel engineering techniques can be exploited to counter short-channel effects. First, the SiO_2 gate oxide can be thinned down to increase the control of the gate field over the channel. However, a thinner oxide will cause a larger leakage current. It has been shown that traditional SiO_2 gate oxide would reach its quantum mechanical tunneling barrier at about 2 nm for 100 nm gate-length device, short-circuiting the gate and the body of the device [15]. To continue scaling down the device and oxide thickness, modern generation of devices exploit dielectrics with high permittivity (high-κ) so a larger gate field can be applied with a physically thicker dielectric layer avoiding high leakage and tunneling breakdown. The introduction of high-κ dielectrics also necessitates the use of metal gate because the traditional heavily doped poly-silicon gate is not compatible with high-κ technology. It has been shown that high-κ dielectric/poly-silicon gate transistors exhibit severely degraded the electron mobility in the channel under inversion condition [16-17]. The high-κ dielectrics, by definition, have soft (usually metal-oxide) bonds which are highly polarizable. The electrons at the inversion layer in the semiconductor channel tend to couple with these soft surface longitudinal optical phonon modes at the surface of the dielectric material [18]. This coupling will effectively cause electrons in the inversion layer to be scattered by the ionic polarization in the dielectric layer [18]. This coupling is less severe in the harder and less polarizable (hence, lower κ) Si-O bonds in SiO_2. In addition, the surface plasmons of the gate material are also coupled with the dielectric

6

surface phonons, which in term, are coupled with electrons in the inversion layer in the channel. It has been shown that metal gate is better at screening the coupling between dielectric surface phonons and channel inversion layer electrons than the standard poly-silicon gate [18-19]. Therefore, to prevent the degradation of electron mobility in the inversion layer, a metal gate has to be used along with high-κ dielectric layer.

Secondly, source and drain junction depths can be decreased to reduce the depletion into the channel under the gate. The drawback of this approach is an increase of parasitic contact resistance due to a shallower source/drain junction. A compromise is reached by introducing a lighter-doped ultra-shallow junction right between the source/drain and the channel called source/drain extension. The shallow source/drain extension with light doping ensures minimal depletion into the channel by source/drain while a deeper and more heavily doped source/drain maintains a low contact resistance.

Another channel engineering solution to reduce short-channel effects is to increase the channel doping to deter channel depletion due to charges from the source/drain region. This approach, however, leads to the degradation of carrier mobilities in the channel due to impurity scattering. The remedy is to introduce a high concentration of halo doping near the interface between the source/drain extension and the body. Figure 1.3 depicts a schematic of halo doping and other complex channel doping engineering techniques used in modern devices to counter short-channel effects. The complex and stringent doping requirements for modern devices show the importance of controlling the precise location of dopants. Therefore, knowledge of diffusion mechanisms of these dopants and the effect of native point defects on diffusion is crucial for the processing of modern devices.

Channel strain engineering, which will be discussed next, to increase inherent carrier mobility is effective in conjunction with channel engineering to counter the short-channel effects. However, straining cannot be continued indefinitely. A change of transistor geometry or higher intrinsic mobility material (e.g. germanium) for the device active layer is needed to continue the trend of device performance improvement.
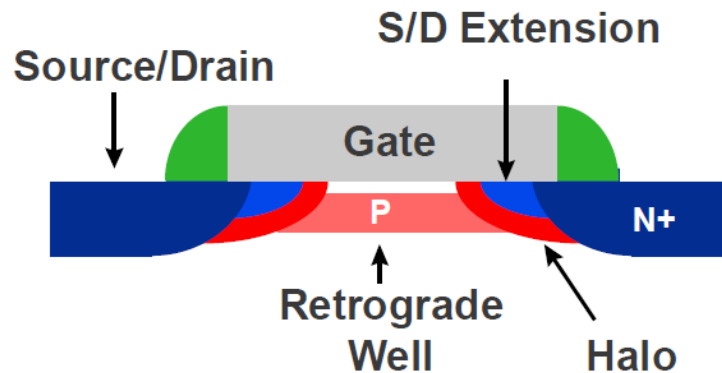
Figure 1.3 Schematic representation of different channel engineering to counter short-channel effects (from ref. [15]).

1.2.2   Strain engineering

Along with channel engineering, strain engineering of the channel is also used to enhance device performance while dimensions scale down. Straining the channel can improve carrier mobility, therefore, device performance, by altering the local band structure of the channel. With engineering optimization, the electron mobility can be enhanced by ~2x while hole mobility can be enhanced by ~10x in a strained silicon channel [20]. Techniques to strain the channel can be divided into two major types, global wafer-level straining and local device-level straining. The wafer-level straining typically provides biaxial stress by using different substrates while device-level straining typically induce uniaxial stress from device processing. Regardless of the type of strain engineering, incorporation of germanium with its complete miscibility with silicon and larger lattice constant, is the most important method in inducing strain in a silicon channel. In this section, wafer level strain engineering by epitaxial growth of strained Si on a SiGe alloy virtual substrate and device level channel strain engineering by using SiGe alloy in the source/drain regions will be discussed briefly. More detailed descriptions can be found in refs. [20] and [21].

Pseudomorphically grown Si on $Si_{1-x}Ge_x$ shows enhanced electron mobility. During the mid 1980s, improvements in epitaxial film growth techniques led to studies of band alignments of Si/SiGe heterostructures. In 1985, Abstreiter *et al*. determined that tensile strained Si grown on relaxed SiGe forms a two-dimensional electron gas (2DEG) containing a type II band alignment [22]. Abstreiter *et al*. further showed that the six-fold degeneracy at the relaxed silicon conduction band is lifted and split into a lower energy two-fold valley and a higher energy four-fold valley [22]. This split of degeneracy at the conduction band can lead to higher electron mobility due to less inter-valley scattering at the conduction band minimum. In subsequent years, efforts were focused on reducing the formation of defects such as threading dislocations for this heterostructure by using compositionally graded buffer layers [23-24]. While early applications were focused on modulation-doped field-effect transistors to take the advantage of the high mobility 2DEG, Welser *et al*. showed for the first time in 1992 the fabrication of a strained traditional n-channel MOSFET with enhanced electron mobility [25]. The same group later quantified the electron mobility enhancement to be 80% more than that of a unstrained n-MOSFET while no significantly different hole mobility was observed at room temperature [26].

Biaxial tensile strain also enhances the hole mobility in silicon. Nayak *et al*. reported the first strained Si p-channel MOSEFT with 50% increase in hole mobility in 1993 [27]. They reasoned that the biaxial strain lifts the degeneracy of heavy-holes (HH) and light-holes (LH) at the Γ point of the valence band, resulting in a lighter effective mass of holes in the valence band and less inter-valley scattering, therefore, higher hole mobility. Figure 1.4 depicts a simplified valence band structure of silicon under strained and unstrained conditions. The strained valence band not only splits the degeneracy of HH and LH bands, it also pushes the split-off (SO) band down. Further, the effective masses of the holes become highly anisotropic [28]. Theoretically, the enhancement of hole mobility due to strain is more pronounced than that of electrons, however, it is later shown that at high vertical field conditions, i.e., high gate voltage, the hole mobility can actually be lower than in unstrained devices due to scattering with Si/SiO_2 interface

[29-30]. Uniaxially strained devices, however, do not suffer this performance problem [31]. Therefore, the research focus quickly switched to uniaxially strained channels.
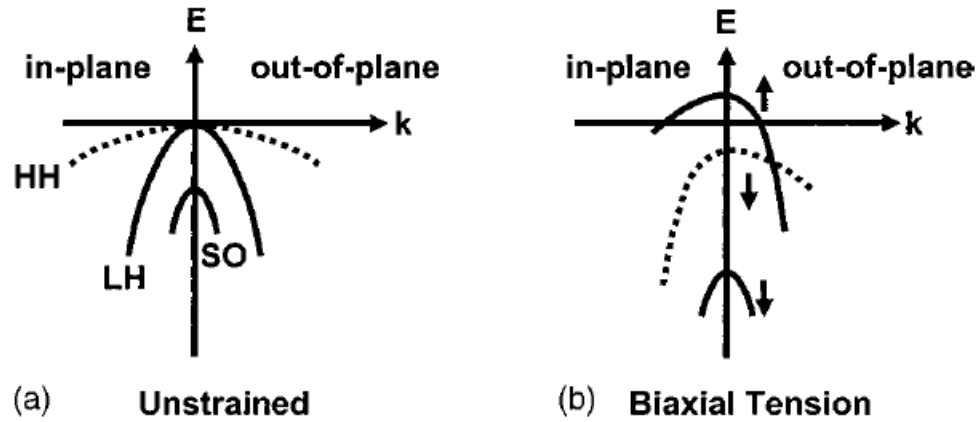
Figure 1.4 Simplified schematics of the silicon valence band structure near the Γ point for (a) unstrained and (b) biaxial tensile strained channel showing anisotropy (from refs. [20] and [28]).

Uniaxial strain has proven to be better in enhancing mobilities of both electrons and holes with less strain required for the same level of mobility enhancement [31]. The difficulty, however, is to improve the mobility simultaneously for both n- and p-channel MOSFETs on the same chip with wafer-level uniaxial strain. For this reason, process-induced local uniaxial strain is the preferred method in applying uniaxial stress. Further, process-induced strain is commercially more viable because of less integration challenges and process complexities when compared with introducing SiGe alloy virtual substrates. In addition, strain levels can be individually tuned for p-channel and n-channel devices.

Intel Corp. has successfully mass-produced process-induced locally strained Si channel logic chips for its 90 nm technology node product line [32-33]. They use heteroepitaxial growth of SiGe in the source/drain regions to induce uniaxial compressive strain on p-channel and silicon nitride high stress capping layer for inducing uniaxial tensile strain on n-channel devices. Figure 1.5 shows transmission electron microscopy (TEM) micrographs of the Intel design. Through detailed studies, it has been determined that uniaxial compressive strain is better in enhancing hole mobility than biaxial tensile strain [31]. Nevertheless, even with a highly strained channel, the mobility is still nowhere near that of the intrinsic mobility of Ge, especially for holes. Once again, the incorporation of Ge into modern devices demands for more studies of fundamental properties such as diffusion in SiGe alloys and Ge.

9
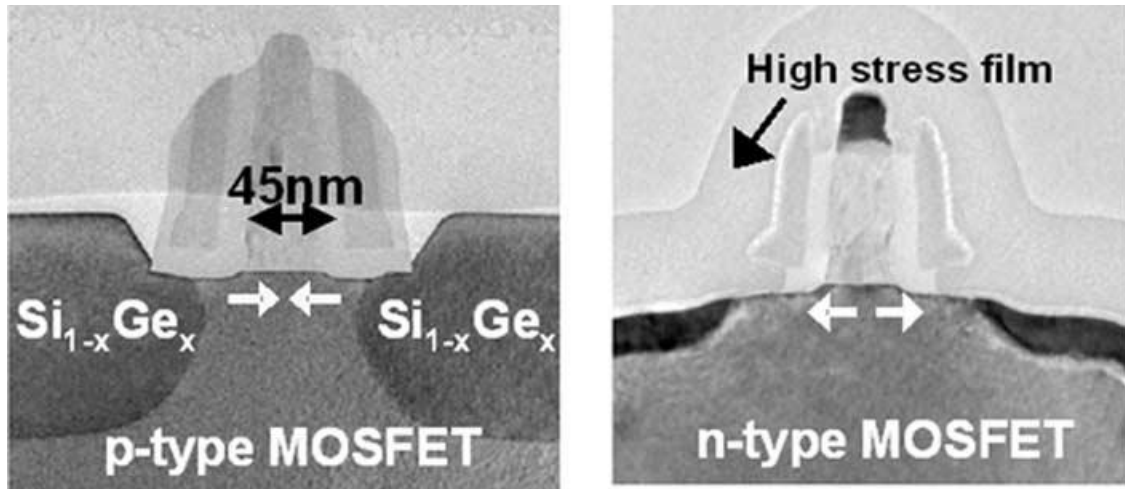
Figure 1.5 TEM micrographs of Intel 45-nm physical gate length p-channel and n-channel MOSFETs (from ref. [33]).

1.2.3 Germanium as channel material

Continuing device performance improvement below the 32-nm technology node necessitates the introduction of novel non-planar geometry (e.g. FinFETs and tunneling FETs) and/or new high mobility channel materials [13]. As discussed in previous sections, the scaling of Si based devices, even with strain engineering, complex channel doping engineering, and high-κ dielectric with metal gate technology, has reached its limit in raising device performance. Besides novel device structures, an obvious materials engineering solution to improve performance is to use high mobility channel materials such as Ge, the semiconductor used in the first transistor. Most important advantages and disadvantages of Ge as channel material will be highlighted in the following paragraphs. Detailed discussions are elucidated elsewhere such as in refs. [14, 34].

The main advantage of Ge is its high electron and hole mobilities in comparison with Si. Under intrinsic conditions at room temperature, the Ge electron and hole mobilities are ~3x and ~4x that of Si respectively. Table 1.1 below shows some material properties for Si, Ge, and GaAs. The more symmetric electron and hole mobilities of Ge are also beneficial for real estate planning of n- and p-channel MOSFETs on a chip because they would occupy more symmetric footprints. Further, the lower bandgap of Ge not only enables lower voltage operation, it is also closer to the ideal low-loss 1.3 to 1.55 μm wavelength range important in optical communication applications for possible optoelectronic integration [35]. In addition, the lower melting point of Ge implies lower overall processing temperatures which has been demonstrated to be more compatible with high-κ dielectrics and metal gate technology [36]. With many advantages in comparison with Si, Ge p-channel MOSFETs have been successfully produced by many research groups [37-40]. Ge p-channel devices, in general, show better performances than Si-based devices; a 65 nm channel length device demonstrated a 40% increase in on-current compared to Si devices [39]. The development of Ge channel technology, especially for p-channel, has clearly been established to replace Si for new generations of devices as projected by the International Technology Roadmap for Semiconductors (ITRS) [13].

10

Table 1.1 Some materials properties of Si, Ge, and GaAs

	Si	Ge	GaAs
Electron Mobility (cm^2/V-s)	1400	3900	8500
Hole Mobility (cm^2/V-s)	450	1900	400
Bandgap (eV)	1.12	0.66	1.42
Melting Point (°C)	1414	938	1240

A Ge channel is not without limitations and drawbacks in comparison with Si. Many of the same limitations that first drew the attention away from Ge as the material of choice for solid-state electronics 50 years ago are still hindering the use of Ge. For instance, the lower bandgap and higher surface defect density result in higher leakage current. Also, Ge is more expensive than Si and the crystal growth technique for large wafers is not mature. As a result, large resources are being focused on growing thin-film Ge on existing Si substrates or on an insulator layer on a Si substrate to minimize Ge usage. One of the most challenging limitations of Ge is, however, the difficulty in forming ultra shallow and high electrically activated n-type junctions. The processing of n-channel MOSFETs remains to be a challenge due to high donor diffusivity in Ge and donor deactivation for concentrations above mid 10^{19} cm^{-3} [41-43].

With proper defect engineering, donor diffusion may be suppressed and electrical activation may be enhanced. To do this, the first step is to establish a firm understanding of defect behavior and diffusion mechanisms of impurities in Ge. Although indirectly, studying diffusion is, arguably, the best way to probe the behavior of point defects at elevated temperatures. Therefore, studying diffusion is essential for the realization of n-channel Ge MOSFET devices. The diffusion and deactivating mechanisms of donors in Ge and possible ways to suppress donor diffusion are discussed in Chapter 5. The next chapter will elaborate on the importance of studying diffusion and explain some diffusion basics.

Chapter 2 Fundamentals of Diffusion

The previous chapter describes the need to reintroduce germanium into modern devices to continue scaling of device dimensions and improving performance. Needless to say, the introduction of Ge into devices requires a firm understanding of impurity diffusion behavior in Ge. The first section of this chapter will elaborate on the importance of understanding diffusion. A discussion of common diffusion mechanisms and diffusion equations in semiconductors will then follow in Section 2.2.

2.1   Importance of understanding diffusion

The understanding of defect reactions and dopant diffusion is crucial for the fabrication of new generation of germanium-containing devices. The diffusion data on impurities in Ge largely predate the availability of pure crystals and more sensitive characterization techniques such as secondary ion mass spectrometry (SIMS). Therefore, the Ge diffusion data available in the literature are unreliable. New and more accurate diffusion parameters are needed to enable Ge-based device processing.

Further, the study of diffusion will yield not only diffusion coefficients of various technologically important impurities in Ge but also impurity-defect interactions and diffusion mechanisms. A detail knowledge of defect reactions, charge states of the defects, and formation and migration enthalpies of defect-impurity pairs is crucial for device process simulators, an important component of the methodology of design for manufacturability (DFM) for the IC industry. Additionally, by knowing these interactions, challenges such as high electrical activation for donors in Ge may be resolved by proper defect engineering. Specific deactivation mechanisms of donors due to defect-donor interactions will be discussed in Chapter 5.

The study of diffusion is not only essential technologically but also important scientifically. Diffusion is the most fundamental mass transport process in a solid characterized by impurity-defect interactions. Although indirect, diffusion is perhaps the only experimental technique to study point defect dynamics in solids at elevated temperature [44]. Various techniques such as electron paramagnetic resonance (EPR), infrared (IR) spectroscopy, and deep level transient spectroscopy (DLTS) can be used to characterize point defects in solid. However, these techniques are usually limited to the cryogenic to room temperature range, far from diffusion temperatures. An exception is positron annihilation spectroscopy (PAS). However, PAS can only probe vacancy-like defects and is not sensitive enough to study the relatively low equilibrium concentration of vacancies. Through the study of diffusion at various temperatures, dopant concentrations, defect concentrations, and extensive modeling, the fundamental properties of these native point defects can be studied at high temperature.

In short, the comprehensive understandings of dopant diffusion mechanisms and the properties of native point defects, including their charge states, generation, recombination, and their interactions with dopant atoms are of fundamental significance from both a scientific and device fabrication points of view. There is currently a lack of diffusion coefficients, fundamental understanding of defect reactions, and diffusion mechanisms of dopants in SiGe and Ge. Therefore, it is the aim of this research work to clarify and identify diffusion mechanisms of As

in SiGe (Chapter 4) and other dopants in Ge (Chapter 5). Particular attention is focused on identifying the role of self-interstitials on the diffusion in Ge in Chapter 5.

2.2   Diffusion basics

Fundamentals of diffusion in semiconductor will be discussed in this section. In subsection 2.2.1, a brief history of Adolf Fick's diffusion equations will be presented. Section 2.2.2 will describe different diffusion mechanisms in solids with emphasis on semiconductors. Finally, in Section 2.2.3, a thermodynamic description of diffusion will be presented.

2.2.1   A brief description of Fick's diffusion equations

The basis of the current description of mass transport by diffusion is derived from the experimental work by Adolf Fick, a German-born Swiss physiologist. Fick was a professor at the medical school of the University of Zürich and had a professional interest in the diffusion of salt in the human body. In 1855, he published a paper entitled "On liquid diffusion" describing his experiments on the diffusion of salt in aqueous solution [45]. In his experiments, a steady state concentration gradient was achieved by placing a piece of solid salt on the bottom of a water column and a large reservoir of pure flowing water on the top end. This setup ensured one end of the column was saturated with salt while the other end maintained a zero salt concentration. He then measured the concentration of salt painstakingly by measuring the specific density of the solution along the column by suspending a glass bulb attached to one side of a balance. From the specific density, he could back calculate the concentration of salt in the solution as a function of position in the column. From this, he proposed a phenomenological equation describing the mass transport of salt. In modern notation, the equation has the form:

$$J = -D\nabla C \tag{2.1}$$

where J is the flux of the mass and C is the volume concentration of the mass. The proportional constant between the flux and the negative of the gradient of concentration is D, the diffusion coefficient or diffusivity. Equation (2.1) is now known as Fick's First Law of diffusion.

Fick generalized the description of matter transport to consider non-steady state concentrations. If the concentration of salt is a function of time, he proposed another equation to describe the transport process:

$$\frac{\partial C}{\partial t} = -\nabla J = \nabla(D\nabla C) \tag{2.2a}$$

If the diffusivity, D, does not depend on the position, then Equation (2.2a) can be rewritten as:

$$\frac{\partial C}{\partial t} = D\nabla^2 C \tag{2.2b}$$

Equations (2.2a) and (2.2b) are now called Fick's Second Law of diffusion.

It is important to note that Fick's Second Law has a general form that resembles equations that describe diffusion of heat (Fourier's heat equation) and electricity (Ohm's law). A more detailed discussion of differential equations of this type is given in the review article by T. N. Narasimhan [46].

Although Fick's diffusion equations were developed to describe diffusion in a liquid, the same form can be used to describe mass transport in gases, liquids, and solids. However, it should be stressed again that Fick's equations are phenomenological in nature, true diffusion is governed by statistical random walk processes. A concentration gradient is not the driving force for diffusion. In fact, for Fick's equations of diffusion to work in solids, one has to assume that the solutes are at the dilute limit and that there is no interaction between solute and solvent atoms. Nevertheless, equations describing solid state diffusion still have the general form of Fick's Second Law with added components to describe various solute-solvent interactions. For instance, the differential equation describing the vacancy diffusion mechanism, where a substitutional impurity A_S combines with a vacancy V and moves as an impurity-vacancy (AV) pair during diffusion:

$$A_S + V \Leftrightarrow AV \tag{2.3}$$

can be written in one dimension as:

$$\frac{\partial C_{AV}}{\partial t} = \frac{\partial}{\partial x}\left(D_{AV}\left[\frac{\partial C_{AV}}{\partial x}\right]\right) + k_f[A_S][V] - k_r[AV] \tag{2.4}$$

where C_{AV} is the concentration of AV pairs, D_{AV} is the diffusivity of the defect pair, and k_f and k_r are the formation and recombination rate constants for reaction (2.3), respectively. Clearly, Equation (2.4) has the general form of Fick's Second Law with extra terms describing impurity-vacancy interactions; differential equations of similar form can be written for different diffusion mechanisms. Section 2.2.2 will elaborate on common diffusion mechanisms in solid.

2.2.2 Diffusion mechanisms in solids

Diffusion in solids is mainly mediated by interactions between diffusing species and native point defects. Unlike diffusion in gaseous and liquid states, simple Fick's Laws, which describe diffusion of dilute solutes in non-interacting solvent, often do not describe the diffusion in solids fully. The interactions between diffusing species and native point defects cannot be neglected due to the close proximity of the atoms. Detailed analysis and descriptions of these interactions and diffusion mechanisms in solid can be found in refs. [44, 47].

Different from purely random walk diffusion processes as occurring in gaseous and liquid states, diffusion in solids has six generally accepted mechanisms. The mechanisms can be further broken down into two main types: direct and indirect. Direct diffusion mechanisms are the ones that do not require the assistance of native point defects while indirect diffusion mechanisms involve either vacancies or self-interstitials. Two types of direct diffusion mechanisms, pure interstitial and direct exchange, are shown schematically in Figure 2.1.

14

Pure interstitial   Direct exchange
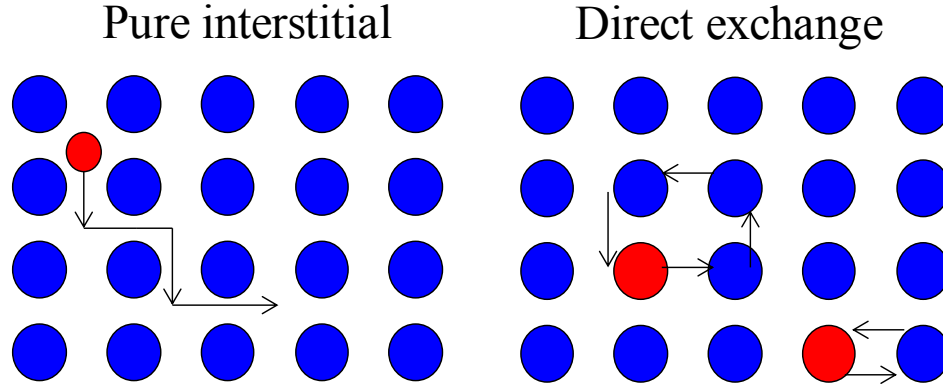
Figure 2.1 Schematic diagrams of the direct diffusion mechanisms in solids: pure interstitial and direct exchange. The blue circles represent host atoms while red circles are diffusing species. Arrows indicate diffusion motion.

The pure interstitial mechanism involves diffusion of small species through the interstitial sites within the lattice of host atoms. The motion of the diffusing species in this mechanism consists of a purely random walk process; therefore, this is the only solid state diffusion mechanism that can be accurately described by Fick's Laws of diffusion. Because the diffusing species move entirely in the interstices, only very small atoms such as H and Li diffuse via this process. 3d transition metals in Si have also been found to diffuse by a pure interstitial mechanism due to their small size in the ionized states [48]. Because of their small size and lack of interactions with the host lattice, impurity diffusion by the pure interstitial mechanism usually has a very high diffusivity.

The direct exchange describes substitional foreign atoms exchange position with adjacent host atoms. This can be done either by direct exchange with the adjacent atom or by a ring exchange mechanism as depicted in Figure 2.1. The direct exchange mechanism requires simultaneous motion of two or more atoms therefore is energetically very costly. So far, this mechanism has only been proposed theoretically; no convincing experimental evidence has been found for this diffusion mechanism because it is energetically unfavorable.

The indirect diffusion mechanisms can also be categorized into two types, vacancy-assisted and self-interstitial-assisted mechanisms, depending on the native point defects involved in the process. Vacancy-assisted mechanisms can further be divided into two types: vacancy mechanism and dissociative mechanism. The two vacancy-assisted mechanisms are schematically shown in Figure 2.2. The vacancy mechanism involves a substitional impurity, A_S, interacting with a vacancy, V. If a vacancy happens to diffuse to the adjacent site of the substitutional impurity, the two form a pair. The diffusion step is complete when the A_S exchanges position with V and V diffuses away a minimum of three lattice sites. The reaction with charge states can be written as:

$$A_S^m + V^k \Leftrightarrow AV^j + (j-k-m)e^-\qquad(2.5)$$
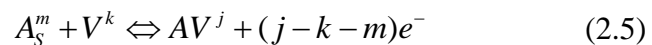
Here, the superscripts (j,k, and m) are ± integers representing the charge states. Sb diffusion in Si is an example of diffusion via vacancy mechanism. In addition, it is important to note that most diffusion in Ge, including self-diffusion and common dopants diffusion, is believed to occur via vacancy mechanism. Diffusion in Ge will be discussed in greater length in Chapter 5.
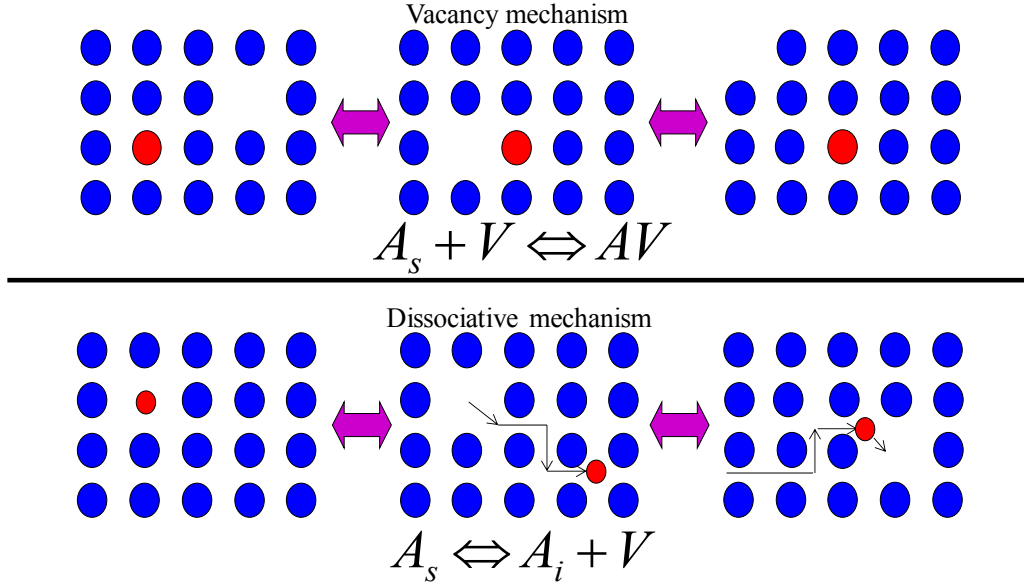
Figure 2.2 Schematics of vacancy-assisted diffusion mechanisms in solids: vacancy mechanism (top) and dissociative mechanism (bottom). As before, blue circles represent lattice atoms whereas red circles represent diffusing impurities.

The dissociative diffusion mechanism occurs when the substitional foreign atom, A_S, leaves the substitional site, thereby creating a vacancy, and diffuses through interstitial sites of the lattice. The diffusion step is complete when the dissociated foreign atom in interstitial site (A_i) recombines with another vacancy and therefore becomes a substitional impurity again. The reaction with charge states can be described as:

$$A_S^m \Leftrightarrow A_i^q + V^k + (q + k - m)e^- \qquad (2.6)$$

Again, q, k, and m are ± integers describing charges on the impurity or vacancy. The dissociative mechanism is one of the two hybrid diffusion mechanisms where the impurity occupies a substitional site but moves as interstitial defect, A_i, resulting in a larger diffusion length per diffusion step when compared to the vacancy mechanism. Cu diffusion in Ge is an example for this diffusion mechanism.

Self-interstitial assisted mechanisms can also be subdivided into two types: interstitialcy mechanism and kick-out mechanism. Figure 2.3 shows the schematics representing the two self-interstitial assisted mechanisms. The interstitialcy mechanism involves an impurity, A, and a self-interstitial, I, forming a pair (AI) occupying one lattice site (an interstitialcy). The diffusion

species, A, can move by forming interstitialcy pairs with other neighboring atoms. The diffusion step is complete when the interstitial has moved away, forming an interstitialcy with a neighboring self-atom, leaving the diffusing impurity fully substitional. The diffusion reaction with charge states can be expressed as:

$$A_S^m + I^u \Leftrightarrow AI^v + (v - m - u)e^-$$ (2.7)
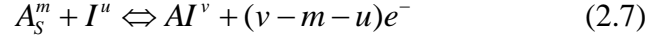
Phosphorus diffusion in Si is a typical example for the interstitialcy diffusion mechanism.

Interstitialcy mechanism

$$A_s + I \Leftrightarrow AI$$

Kick-out mechanism

$$A_s + I \Leftrightarrow A_i$$
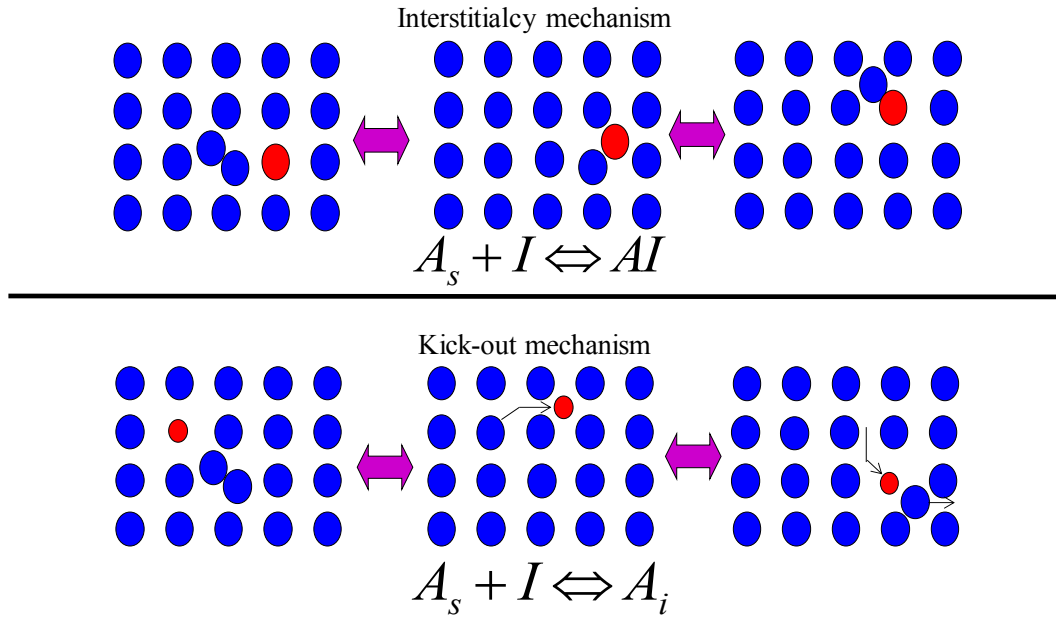
Figure 2.3 Schematics of self-interstitial-assisted diffusion mechanisms in solids: interstitialcy mechanism (top) and kick-out mechanism (bottom). Here, blue circles represent lattice atoms whereas red circles represent diffusing impurities.

Finally, the kick-out mechanism involves an interstitial with a nominally substitional impurity. The self-interstitial, I, moving in the lattice can approach a substitional foreign species, A_S, and kicks A_S out of the substitional site. As a result, A_S becomes interstitially moving, A_i, until it kicks another lattice atom out, completing the diffusion step. The diffusion reaction with charge states can be described as:

$$A_S^m + I^u \Leftrightarrow A_i^q + (q - m - u)e^-$$ (2.8)
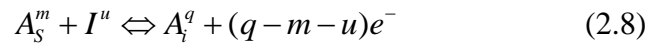
The kick-out mechanism is the other hybrid diffusion mechanism in which the motion of diffusing species occurs while they are moving interstitially. Boron diffusion in Si is a classic example of the kick-out diffusion mechanism.

In addition to reactions (2.5)-(2.8), reactions between point defects and defect pairs should also be considered. First of all, vacancies and self-interstitials can annihilate each other. This Frenkel-pair reaction can be written as:

$$V^k + I^u + (k+u)e^- \Leftrightarrow \phi \qquad (2.9)$$
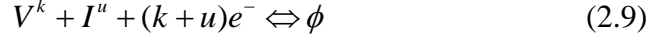
Here, φ represents a self-atom on a regular lattice site. Other reactions describe annihilation of vacancies or self-interstitials with impurity-defect pairs:

$$AI^v + V^k + (v = k - m)e^- \Leftrightarrow A_s^m \qquad (2.10)$$

$$AV^j + I^u + (j + u - m)e^- \Leftrightarrow A_s^m \qquad (2.11)$$
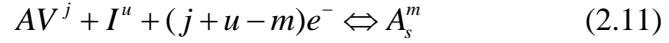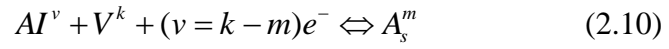
In theory, reactions (2.5)-(2.11) can be represented by differential equations of the type similar to Fick's Second Law (e.g. Equation 2.4). Diffusion simulation, then, can be performed by solving all these coupled differential equations simultaneously to fit experimentally measured diffusing impurity profiles. Once a self-consistent fitting is found, the dominating diffusion mechanism for the given diffusion species can be identified. However, this is impractical because of the sheer number of independent variables. The number of independent variables can be greatly reduced if multiple species and self-diffusion profiles can be measured in the same sample. The availability of stable semiconductor isotopes enables such experiments [49]. As a result, detailed studies of B, P, As and Si self-diffusion in Si have been performed [44, 50-51]. The same approach can be extended to study diffusion in SiGe and Ge in order to determine diffusion mechanisms of important impurities. Chapter 3 will describe the details of this experimental technique while Chapter 4 will show the results of As diffusion in SiGe using the this methodology.

2.2.3   Thermodynamic description of diffusion

Diffusion in solids is a thermally driven process; therefore, the diffusion coefficients can be described by thermodynamic terms. It can be expressed empirically as an Arrhenius or activation type of equation:

$$D = D_0 \exp\left(\frac{-H^M}{k_B T}\right) \qquad (2.12)$$

Here, D is the diffusivity, H^M the migration enthalpy, k_B the Boltzmann's constant, and T the absolute temperature. The pre-exponential factor, D_0, is defined as:

$$D_0 = g a v_0 \exp\left(\frac{S^M}{k_B}\right) \qquad (2.13)$$

where g is a geometric factor depending on the crystal structure and the diffusion mechanism, a is the lattice constant, v_0 is the attempt frequency and S^M is the migration entropy. The geometric factor $g = \frac{1}{2} \times \frac{1}{4} = \frac{1}{8}$ for the vacancy mechanism in the diamond cubic structure. This is because for the vacancy mechanism in the diamond cubic structure there are four possible equivalent vacancy sites due to the tetrahedral bonds. The factor ½ takes into account that only half of the jump should be counted because the other half is jumping back into the original site. The attempt frequency, or jump frequency, is the number of attempts for the diffusing impurity to jump to one of the 1/g available and equivalent sites per second. Thus, the jump frequency is the vibrational frequency of the diffusing species in the lattice. One should note that the jump frequency, v_0, varies as $m^{-1/2}$; therefore, the slight differences in mass for different isotopes can affect diffusivity. In practice, however, the difference is often too small to be accurately measured except for very light elements; diffusivities of different isotopes of matrix self-atoms and of typical dopant elements can be assumed to be the same.

By combining Equations (2.12) and (2.13), the diffusion coefficient can be expressed as:

$$D = g a^2 v_0 \exp\left(\frac{S^M}{k_B}\right) \exp\left(\frac{-H^M}{k_B T}\right) = g a^2 v_0 \exp\left(\frac{T S^M - H^M}{k_B T}\right) \qquad (2.14)$$

Since the total Gibbs free energy of migration is given by:

$$G^M = H^M - T S^M \qquad (2.15)$$

Equation (2.14) can be reduced to:

$$D = g a^2 v_0 \exp\left(\frac{-G^M}{k_B T}\right) \qquad (2.16)$$

The derivation thus far only applies to the pure interstitial diffusion mechanism. For defect-assisted diffusion mechanisms, the formation of those native point defects must also be considered. At thermal equilibrium, the concentrations of native point defects are given by:

$$C_{I/V}^{eq} = C_0 \exp\left(\frac{S_{I/V}^F}{k_B}\right) \exp\left(\frac{-H_{I/V}^F}{k_B T}\right) \qquad (2.17)$$

where C_0 is the atomic concentration of the host element, and S^F and H^F are the formation entropy and formation enthalpy of the native point defect, respectively.

Considering for example self-diffusion in Si, where both vacancy-assisted and self-interstitial-assisted diffusion mechanisms are important, the total self-diffusion coefficient is given by:

$$D_{Total}^{SD} = f_V \frac{C_V^{eq}}{C_0} D_V + f_I \frac{C_I^{eq}}{C_0} D_I \qquad (2.18)$$

where f_V and f_I are correlation factors for vacancy-mediated and interstitial-mediated diffusion mechanisms, respectively, and D_V and D_I are the diffusivities of vacancies and self-interstitials, respectively. D_V and D_I have the form described in Equation (2.16) above. By substituting the expression in Equation (2.17) into (2.18) and by considering Equation (2.13), self-diffusivity can be written as:

$$D_{Total}^{SD} = f_V D_{0,V} \exp\left(\frac{-H_V^{SD}}{k_B T}\right) + f_I D_{0,I} \exp\left(\frac{-H_I^{SD}}{k_B T}\right) \qquad (2.19)$$

Here, $H^{SD} = H^F + H^M$; the total activation enthalpy is the sum of formation enthalpy for the given defect and the migration enthalpy.

It is important to note that Equation (2.18) can be generalized. In most cases, total diffusion of a species is always the sum of the contributions from vacancy-mediated diffusion mechanisms and self-interstitial-mediated diffusion mechanisms. The fact that only one Arrhenius law is observed experimentally at a given temperature range indicates that one diffusion mechanism (vacancy- or interstitial-mediated) is dominant at that temperature range. In germanium, on the other hand, it has been firmly established that only the vacancy mechanism is observed for all common impurities for the full temperature range under thermal equilibrium condition [41, 52-53]. Thus, the germanium self-diffusion coefficient is given by:

$$D_{Ge}^{SD} \approx f_V \frac{C_V^{eq}}{C_o} D_V \qquad (2.20)$$

20

Then, for germanium, the follow condition holds true:

$$C_I^{eq} D_I << C_V^{eq} D_V \qquad (2.21)$$

For this reason, very little is known of the properties of self-interstitials in Ge because their participation is mostly absent from diffusion in Ge. One of the main goals for this research work is to understand the role of self-interstitials for diffusion in Ge by intentionally introducing excess interstitials with concentrations well above the equilibrium value. A detail description is provided in Chapter 5.

The correlation factor, f, measures the reversibility of a diffusion reaction base on the crystal structure. A correlation factor of 1 represents a pure random walk process where the probability of reverse diffusion reaction is 50%. The correlation factors for diffusion via vacancy-mediated mechanisms, f_V, and interstitial-mediated mechanisms, f_I, for the diamond cubic structure have been calculated to be 0.5 and 0.73 respectively [54-55].

As mentioned in Section 2.2.2, the native point defects and defect pairs assisting the diffusion can also be charged. If these defects are charged, the diffusivity becomes highly dependent on the position of the Fermi level at the diffusion temperature. Under extrinsic doping conditions, i.e., the Fermi level is not at the mid-gap, the concentrations of charged point-defects become not only a function of temperature, but also of their defect charge state energy levels according to Fermi-Dirac statistics. Figure 2.4 shows the experimentally determined defect charge state levels within the silicon energy bandgap obtained either by electron paramagnetic resonance (EPR) [56] or by analyzing Au diffusion in p-type Si [57]. It is evident from Figure 2.4 that for a heavily doped n-type Si where Fermi level lies close to the conduction band edge at the diffusion temperature, the concentrations of V^-, V^{--}, and I^0 are higher, resulting in higher diffusivity for species that are assisted by those charged defects. Similarly, for a heavily doped p-type Si, species that are assisted by V^+, V^{++}, and I^+ will have higher diffusivities. To quantity the effect of doping on Si self-diffusion, Equation (2.18) can be generalized into:

$$D_{Si}^{SD} = \frac{f_V}{C_0} \left(C_{V^0}^{eq} D_{Si}^{V^0} + \sum_{r=1} C_{V^{r-}}^{eq} D_{Si}^{V^{r-}} \left(\frac{n}{n_i} \right)^r + \sum_{s=1} C_{V^{s+}}^{eq} D_{Si}^{V^{s+}} \left(\frac{n_i}{n} \right)^s \right) +$$

$$\frac{f_I}{C_0} \left(C_{I^0}^{eq} D_{Si}^{I^0} + \sum_{t=1} C_{I^{r-}}^{eq} D_{Si}^{I^{r-}} \left(\frac{n}{n_i} \right)^t + \sum_{u=1} C_{I^{u+}}^{eq} D_{Si}^{I^{u+}} \left(\frac{n_i}{n} \right)^u \right) \qquad (2.22)$$

Here n is the electron concentration, n_i is the intrinsic carrier concentration, r, s, t, and u are the charge states for negative vacancies, positive vacancies, negative interstitials, and positive interstitials, respectively. Because the mass action law, $pn = n_i^2$, applies, Equation (2.22) can be rewritten in terms of hole concentration, p, as well. If Si self-diffusion were to be mediated by

the vacancy mechanism with doubly negatively charged vacancies only, according to Equation (2.22), the self-diffusivity would depend on the electron concentration squared (n^2).
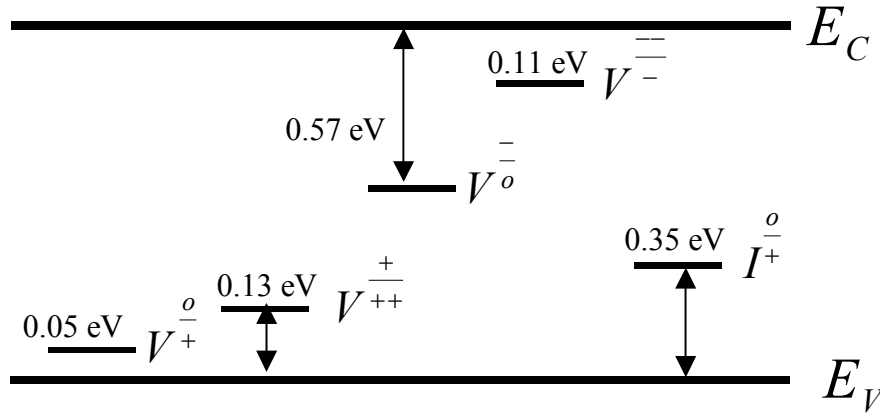
Figure 2.4 Energy levels of known defect charge states in Si. The energy values are either in reference to the valence band edge (E_V) or the conduction band edge (E_C) (from ref. [47]).

A similar energy level diagram for charge states of point defects in Ge is also available. Figure 2.5 depicts such energy level diagram as determined by perturbed angular correlation spectroscopy (PACS) [58]. Haesslein *et al*. deduced a vacancy acceptor level at 0.204 eV above the valence band edge and tentatively assigned a self-interstitial donor level at 0.042 eV below the conduction band edge [58]. This is, yet, another example demonstrating that rather limited fundamental knowledge is available for point defects, especially self-interstitials, in germanium. The fundamental understanding of self-interstitials and their role in diffusion in Ge is crucial to future Ge-based device processing. An equation similar to that of Equation (2.22) can be proposed to describe the doping concentration dependence of Ge self-diffusion. Since the interstitial contributions can be ignored for the equilibrium conditions, the equation becomes [53]:

$$D_{Ge}^{SD} = \frac{f_V}{C_0}\left(C_{V^0}^{eq} D_{Ge}^{V^0} + \sum_{r=1} C_{V^{r-}}^{eq} D_{Ge}^{V^{r-}}\left(\frac{n}{n_i}\right)^r + \sum_{s=1} C_{V^{s+}}^{eq} D_{Ge}^{V^{s+}}\left(\frac{n_i}{n}\right)^s \right) \qquad (2.23)$$

The ultimate goals for this research work are two-fold: first, to show the method of using isotopically enriched heterostructures in simultaneous studies of dopants and self-diffusion can be extended to SiGe alloys; second, to study the roles of self-interstitials in Ge by intentionally introducing excess point defects in concentrations above that of equilibrium values. The first goal is achieved by studying As diffusion simultaneously with self-diffusion in $Si_{0.95}Ge_{0.05}$ isotopically enriched heterostructures. Although the work is done with As in only one alloy composition, the method can be extended to study other dopants for all alloy compositions depending on the availability of isotopically enriched structures in the future. The second goal is, in general, to study dopants and self-diffusion in Ge. More specifically, the focus will be on the role played by the self-interstitials for diffusion in Ge. The excess self-interstitials can be intentionally created by in-situ proton irradiation during diffusion anneals to circumvent the

condition described in Equation (2.21) above. The details of experimental setups and techniques are discussed in the next chapter.
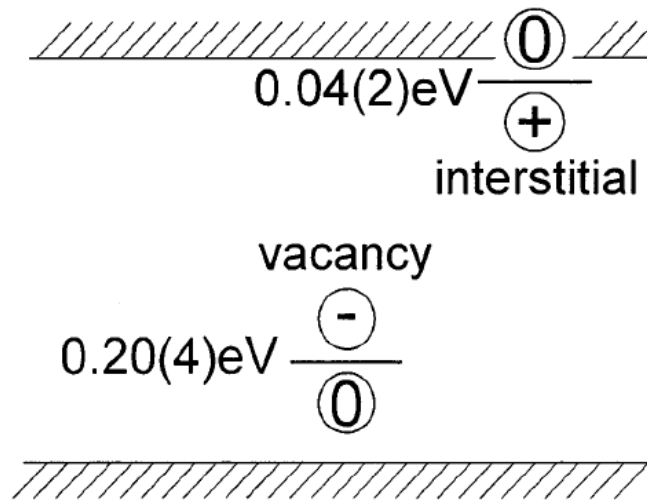
Figure 2.5 The energy levels of charged vacancies and self-interstitials in Ge as determined by PACS. The interstitial energy level assignment is tentative (from ref. [58]).

Chapter 3 Experimental Techniques

Two experimental techniques will be discussed in this chapter. In Section 3.1, isotopically enriched SiGe heterostructures with As doping will be discussed. The structure is used to study As, Si and Ge self-diffusion simultaneously in order to identify the As diffusion mechanisms. The technique and the structure will be described in Section 3.1 while the results and the discussion will be in Chapter 4. In Section 3.2 I will explain the second technique to study the role of self-interstitials for diffusion in Ge. This can be done by creating excess vacancies and self-interstitials in-situ by proton beam irradiation during diffusion annealing. A detailed experimental setup is discussed below in Section 3.2.

3.1   Isotopically controlled structures for diffusion studies

The availability of highly enriched stable isotopes of semiconductors has led to a dramatic increase of interest in scientific studies and technological applications of isotopically engineered semiconductors [49]. Almost all semiconductor materials have more than one stable isotope. For instance, Si has ^{28}Si, ^{29}Si and ^{30}Si with abundances of 92.2%, 4.7%, and 3.1%, respectively, while Ge has ^{70}Ge, ^{72}Ge, ^{73}Ge, ^{74}Ge and ^{76}Ge with abundances of 20.8%, 27.5%, 7.7%, 36.3%, and 7.6%, respectively. Although most material's properties are only very weakly dependent on the isotope composition, some isotope effects are strongly evident. For instance, out of all three stable Si isotopes, only ^{30}Si can be transmuted into ^{31}P with the capture of a thermal neutron, becoming a donor. It has been shown that, when exposed to thermal neutrons, isotopically enriched ^{30}Si crystals yield much higher P concentrations using the neutron transmutation doping (NTD) process [59]. Another application for the isotopically engineered semiconductor is in the field of spintronics or quantum computing. With the availability of highly isotopically enriched Si, the unpaired nuclear spin of ^{29}Si can be utilized in quantum computing or spintronics applications in a matrix of spin-free enriched ^{28}Si. These applications have the potential to revolutionize, once again, the computation and information technologies [60-63].

One of the most important and practical uses for isotopically enriched semiconductors is diffusion studies. Before enriched semiconductor isotopes became available, self-diffusion studies were carried out using the radioactive tracer technique. The technique involves diffusion of a radioactive tracer isotope from the surface into the bulk material. The diffusion profile is determined by mechanically sectioning the material and measuring the radioactivity of each section. The drawbacks for this technique lie in the very limited availability of appropriate half-lives of the available radioactive tracer isotope and the depth resolution of the mechanical sectioning. For isotopes with short half-lives, for example ^{31}Si with half-life of 2.6 hours for β-decay into ^{31}P, the diffusion temperature range and time of the diffusion experiments are extremely limited. The availability of high depth resolution and mass sensitivity profiling technique by secondary ion mass spectrometry (SIMS) and the availability of the stable semiconductor isotopes largely resolved these shortcomings. This new approach not only provides a mean for more accurate self-diffusion studies but also enables the possibility of studying self- and dopant diffusion simultaneously to determine the dopant diffusion

mechanisms. The technique of using isotopically enriched structures along with SIMS has been successfully exploited to study the self- and dopants diffusions in Ge, GaP, GaAs, and GaSb [64-67]. In addition, the molecular beam epitaxy (MBE) grown ^{28}Si/natural Si heterostructures have been very successfully used in extensive studies of Si self- and dopant diffusions which identified detailed defect-impurity interactions, defect charge states, and diffusion mechanisms for all common dopants in Si [44, 47, 50-51].

By way of an example, the simultaneous As and Si self-diffusion results using a isotopically enriched heterostructure are shown in Figure 3.1 below to demonstrate the distinct advantages of diffusion studies utilizing isotope engineering. Under intrinsic conditions, As diffusion is known to be enhanced by both vacancy and interstitial injection; therefore, both the vacancy-assisted mechanism and the interstitial-assisted mechanism need to be considered [68]. The diffusion can be modeled as a combination of the vacancy mechanism (Equation 3.1a and b) and the interstitialcy mechanism (Equation 3.2) [51]:

$$(AsV)^0 \Leftrightarrow As_s^+ + V^- \hspace{4cm} (3.1a)$$

$$(AsV)^- \Leftrightarrow As_s^+ + V^{--} \hspace{4cm} (3.1b)$$

$$(AsI)^0 \Leftrightarrow As_s^+ + I^0 + e^- \hspace{3.5cm} (3.2)$$

Here, AsV and AsI are arsenic-vacancy and arsenic-interstitial pairs, respectively, while the superscripts represent the charge states and the subscript "s" symbolizes substitutional arsenic. The As diffusion coefficient is, then, the sum of the diffusivities of all three mobile As-defect pairs.

The alternating ^{28}Si/natural Si isotopically enriched layers were grown using MBE and As was introduced by ion implantation. Figure 3.1 shows the ^{30}Si and ^{75}As profiles measured by SIMS after 950°C and 122 hours annealing under an argon atmosphere. Here, the highly enriched ^{28}Si layers are represented as the depletions in ^{30}Si profile. Thus, the self-diffusion of Si can be seen as ^{30}Si diffuses into the enriched ^{28}Si layers after annealing. The grey area in the figure represents layers under the extrinsic n-type doping condition at the annealing temperature, i.e., the As concentration is above the intrinsic carrier concentration, n_i, at the annealing temperature. As discussed in Section 2.2.3, under the extrinsic condition, the charge states of the defects play an important role. Indeed, it can observed in Figure 3.1 that Si self-diffusion in the first two ^{28}Si enriched layers is enhanced under extrinsic conditions, indicating that at least one of the native defects assisting the self-diffusion is negatively charged (from Figure 2.4). From other dopants diffusion experiments, this negatively charged defect is identified as the vacancy [51]. The charge states of the vacancy can be determined by simultaneously fitting the ^{75}As and ^{30}Si diffusion profiles. Three charge states, neutral (green solid line), singly negatively charged (red solid line), and doubly negatively charged (blue solid line) vacancies are considered in the fitting. As can be seen from the figure, while the As profile can be fitted independently of the charge states of vacancies, Si self-diffusion for the enhanced portion can only be fitted when V$^-$ is considered; neutral vacancies would lead to a self-diffusion independent of the doping level while V^{--} would overestimate the enhanced diffusion. Therefore, for the vacancy mechanism

contribution to the overall As diffusion, singly negatively charged vacancy defect (reaction 3.1a) dominates in this diffusion temperature. Clearly, one cannot discern the charge states of the vacancy defect by looking at the As diffusion alone; the isotope engineering technique enables the determination of the charge states by studying As and Si self-diffusion simultaneously.
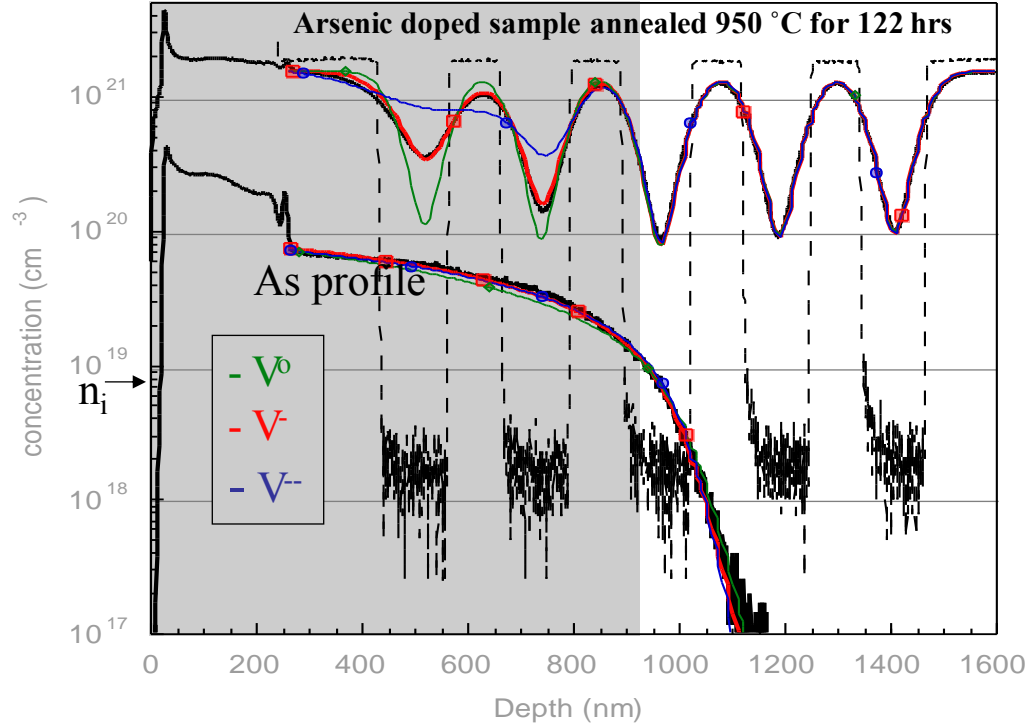
Figure 3.1 Concentration versus depth profiles for the As implanted Si isotope heterostructure after annealing at 950°C for 122 hours. The dashed line shows the ^{30}Si profile before annealing while the solid black line represents SIMS measured ^{30}Si profile after annealing. The measured As profile is also shown in solid black line. n_i denotes the intrinsic carrier concentration at the annealing temperature. The gray area represents the region of the sample that is under the extrinsic diffusion condition. Green, red, and blue curves are diffusion fittings assuming neutron, singly negatively charged, and doubly negatively charged vavancies, respectively, for the charge state of vacancies in the vacancy mechanism (Equation 3.1) contribution of As diffusion. (From refs. [51, 69]).

The same methodology is extended to the study of diffusion in SiGe alloys. $^{nat}Si_{0.95}^{nat}Ge_{0.05}$ / $^{28}Si_{0.95}^{70}Ge_{0.05}$ / $^{nat}Si_{0.95}^{nat}Ge_{0.05}$ heterostructure is grown by molecular beam epitaxy at 450°C on a Si substrate by our collaborators J. Lundsgaard Hansen, A. Nylandsted Larsen *et al.* at the University of Aarhus, Denmark. To reduce threading dislocations caused by the lattice mismatch of the $^{nat}Si_{0.95}^{nat}Ge_{0.05}$ layer and the underlying Si, a graded buffer layer is first grown. The buffer layer is followed by the deposition of a thick layer of $^{nat}Si_{0.95}^{nat}Ge_{0.05}$, 350 nm of isotopically enriched $^{28}Si_{0.95}^{70}Ge_{0.05}$, and finally, 150 nm of $^{nat}Si_{0.95}^{nat}Ge_{0.05}$ capping layer. Figure 3.2 shows the schematic drawing of such structure. The layer thicknesses and the alloy compositions are measured and independently verified by Rutherford backscattering spectrometry (RBS). ^{28}Si, ^{30}Si, ^{70}Ge, and ^{74}Ge concentration profiles as a function of depth are measured by the dynamic quadrupole SIMS at Evans Analytical Group in Sunnyvale, California and shown in Figure 3.3. In the isotopically enriched layer, one can observe that the ^{30}Si and

^{74}Ge concentrations are depleted while ^{28}Si and ^{70}Ge are enriched relative to the natural SiGe layers above and below the enriched layer. This structure is used in $Si_{095}Ge_{0.05}$ self-diffusion and As diffusion studies. More specific experimental setups, results, and discussion will be discussed in the next chapter.
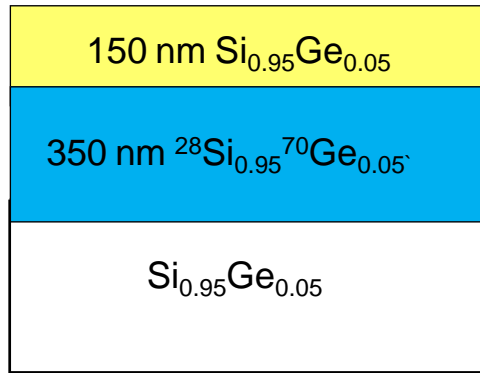
Figure 3.2 Schematic drawing of the isotopically enriched SiGe heterostructure with 5% Ge used in diffusion studies in SiGe. The isotopically enriched layer is sandwiched between two natural SiGe layers.
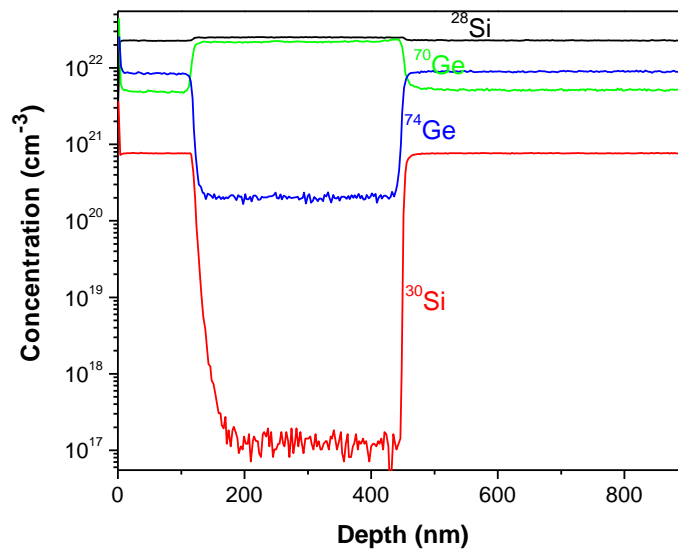
Figure 3.3 Concentration vs. depth for ^{28}Si, ^{30}Si, ^{70}Ge, and ^{74}Ge isotopes for the as-grown heterostructure used in $Si_{0.95}Ge_{0.05}$ diffusion studies.

3.2   Excess point defects generation by proton irradiation

A method to introduce excess self-interstitials in Ge by a highly non-equilibrium process of in-situ proton irradiation during diffusion anneals has been exploited to study the role of self-interstitials for diffusion in Ge. As mentioned in Section 2.2.3, Ge self- and dopant diffusion are known to be mediated predominantly by the vacancy mechanism under equilibrium condition. It has been firmly established from the Ge self-diffusion experiments that condition 2.21 holds true:

$$C_I^{eq} D_I << C_V^{eq} D_V \qquad\qquad (2.21)$$

Experimental evidences and theoretical predictions have shown that the formation enthalpy for Ge self-interstitials (3.2 – 5.7 eV) is much higher than for vacancies (1.9 – 2.3 eV) [70-73], hence C_I^{eq} is much lower than C_V^{eq} .   One the other hand, the migration enthalpy for self-interstitials has been derived to be 0.16 eV, much less than that of vacancies (0.52 – 1.2 eV) near room temperature [71]. As a result, D_I is much higher than D_V. Despite higher self-interstitial diffusivity, condition (2.21) above still holds true. This suggests that the low equilibrium concentration of the self-interstitials dominates the $C_I^{eq} D_I$ product. Excess self-interstitials with concentrations well above the equilibrium concentration must be intentionally introduced in order to study their effect for diffusion. It is well established in Si that ion implantation [74-75] and thermal oxidation [76] inject excess Si self-interstitials in the crystal to enhance interstitial-mediated dopants (e.g. boron) diffusion and to retard vacancy-mediated dopants (e.g. Sb) diffusion. However, these transient enhanced diffusion (TED) and transient retarded diffusion (TRD) effects are not observed in the case of Ge. Instead, it is generally believed that the implantation damage in Ge recovers fast even at low temperatures [77-79]. In order to study the effects of self-interstitials, a steady source of interstitials must be introduced.

Irradiation of materials with high-energy particles is known to create defects.   In particular, irradiation with light particles such as electrons and protons at high energy mainly creates vacancy-interstitial pairs, i.e., Frenkel defects, in a crystal. Very recently, individual Ge self-interstitials induced by electron bombardment were observed directly, for the first time, by researchers at the National Center for Electron Microscopy (NCEM) at the Lawrence Berkeley National Laboratory (LBNL) using the transmission electron aberration-corrected microscope (TEAM) with 0.5Å resolution [80]. The researchers found that Ge self-interstitials in the thinned and electron transparent samples occupy the hexagonal and tetragonal interstitial sites in the diamond cubic lattice [80]. They also found these defects to be short-lived and diffuse to the surface promptly [80].

At MeV energies, particles such as protons do not have much interaction with electrons in the crystal; only repulsive Coulomb potentials of the lattice atoms have to be considered. After the protons are slowed to a few keV range, interactions with lattice electrons start to play a role. These interactions create more recoil atoms and hence more defects, including extended defects. These end of range extended defects can introduce more complexity into the system, therefore, are avoided during our irradiation experiments by thinning down the samples.   The high energetic particles leave mostly point defects (Frenkel pairs) in the first tens of microns and their creation rates can be readily modeled by a Monte Carlo simulation software package, The

Stopping and Range of Ions in Matters (SRIM) [81]. Even though part of the created vacancies and self-interstitials will annihilate with each other and part of them will diffuse to sinks (in general, surfaces), steady-state sources of vacancies and self-interstitials can still be established in the crystal under constant proton bombardment.

To generate steady-state concentrations of vacancies and interstitials exceeding that of the equilibrium values, we irradiate the thinned Ge samples with 2.5 MeV protons with 1.5 µA from a dynamitron accelerator at the University of Bochum, Germany. MBE-grown, boron-doped Ge samples are the main focus of this work to study the role of excess self-interstitials on boron diffusion while our collaborators at the University of Münster, Germany, concentrate on the studies of isotopically enriched Ge multilayer structures for self-diffusion and P implanted Ge for donor diffusion. Detailed descriptions of the samples and experimental conditions are presented in Chapter 5. The proton beam in the experiments is defocused to achieve a homogeneously irradiated circular area with a diameter of 10 mm (flux = 1.91 µA/cm^2 or 1.18×10^{13} H$^+$/cm^2-s for a total beam current of 1.5 µA). From the SRIM simulation, this proton flux generates $\sim 2.1 \times 10^{16}$ vacancies/cm^3-s for the first 1.5 microns of the sample which contains the important structures. Also from the SRIM simulation, the range and straggle for the 2.5 MeV protons are 45.2 µm and 1.8 µm, respectively. Therefore, to avoid the end of range defects, the Ge samples are thinned to 30-40 µm by mechanical lapping and Syton (or Syton + diluted H$_2$O$_2$) polishing to achieve an optically polished surface. The scratch-free optically polished surface is important to avoid bowing due to residual stresses in the thinned samples.

The thinned sample, typically 5 mm $\times$ 5 mm in size, is mounted on a graphite block and covered with another graphite plate with a 3 mm diameter circular aperture. This way, only the part of the sample under the aperture is exposed to the proton beam; diffusion with and without proton irradiation can be studied on the same sample. The graphite block is then placed on a boron nitride *in-situ* vacuum heater. The temperature is monitored by a type K thermocouple embedded in the graphite block roughly 1 mm below the sample. To ensure accurate proton current counting, a stainless steel plate with -600 V potential applied relative to the graphite block is placed above the graphite block. The high negatively biased steel plate is to suppress the secondary electrons created from the high-energy proton irradiation from escaping the heater assembly. The entire heater assembly is then attached to a vacuum chamber at the end of the proton beamline. A schematic of the heater assembly built in the University of Münster used to perform the irradiation experiments is shown in Figure 3.4. A similar heater assembly is being built at Lawrence Berkeley National Laboratory (LBNL) to be attached to a tandem accelerator with 3.4 MeV proton energy. The description and a picture of the LBNL heater are disclosed in Chapter 6. In Chapter 5, the results of these proton radiation enhanced (or retarded) diffusion in Ge experiments performed in Bochum, Germany, will be discussed with emphasis on the B in Ge studies. The results for Ge self-diffusion and P diffusion under in-situ proton irradiation are also discussed for comparison with the boron results. These experiments intend to clarify the role of proton irradiation induced excess self-interstitials for diffusion in Ge.
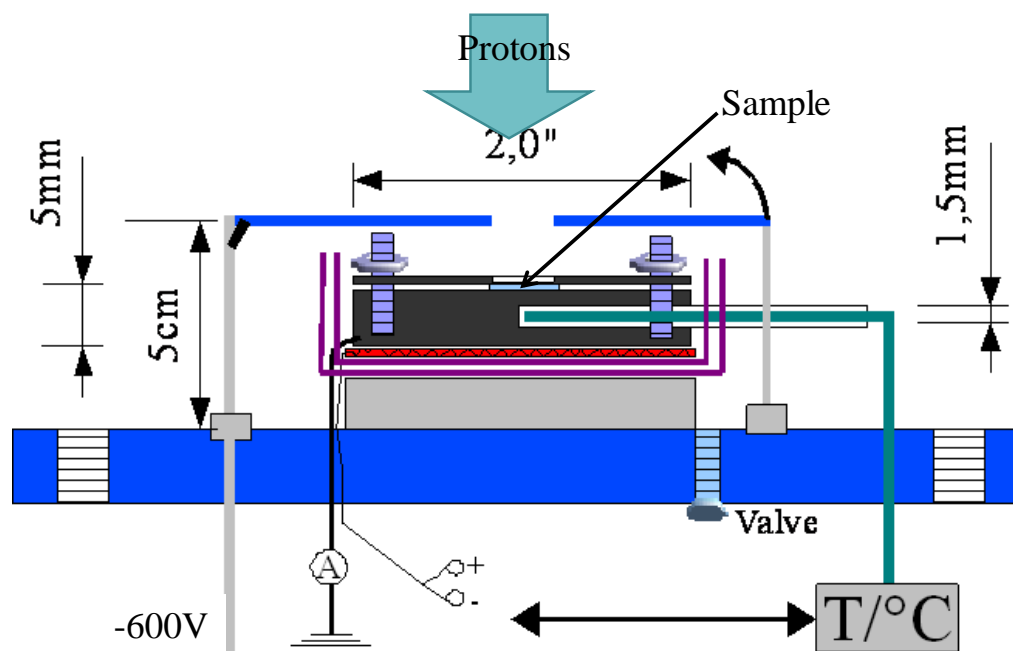
Figure 3.4 Schematic drawing of the heater assembly used in the proton irradiation diffusion experiments. The sample is sandwiched between a graphite block and a graphite plate. The top covering plate has a 3 mm aperture defining the proton irradiated area. The total proton dose is counted by measuring the current from the graphite block. A potential of -600 V is applied to a stainless steel plate above the graphite block to deflect the secondary electrons crated by proton bombardment of the sample to ensure accurate dose counting.

Chapter 4 Diffusion in $Si_{0.95}Ge_{0.05}$

There exists a great interest in using Silicon-Germanium ($Si_{1-x}Ge_x$) alloys in RF circuits with heterojunction bipolar transistors (HBTs) [82]. In RF communication technology, the $Si_{1-x}Ge_x$ HBT is the first practical example of bandgap engineering based on Si technology to achieve high switching speed [83]. On the other hand, as discussed previously, for MOSFET technology, $Si_{1-x}Ge_x$ alloys are used mainly in straining the Si channel material to increase both the electron and hole mobilities [84]. While $Si_{1-x}Ge_x$ enjoys the benefit of compatibility with current Si-based technology, the introduction of Ge into Si greatly alters many materials properties, including the self- and dopant diffusion behaviors. The determination of the diffusion parameters and the fundamental understandings of diffusion mechanisms is not only of scientific importance, but crucial for the processing of new generations of devices.

With the exception of boron [85-86], the diffusion of common dopants is enhanced with the incorporation of Ge in Si. The diffusivity of arsenic (As), one of the most widely used n-type dopants in Si, has been shown to increase with incorporation of Ge into Si [87-91]. While the diffusivities, the interactions with native point defects, and the diffusion mechanisms of As have been determined in pure Si [51] and pure Ge [41], the diffusion mechanisms of As in $Si_{1-x}Ge_x$ with varying Ge contents have not been studied. For As diffusion in Si, the diffusion mechanism is known to be a combination of a vacancy mechanism and an interstitialcy mechanism (with AsV^0, AsI^0, and AsV^- dopant-defect pairs) [51] whereas the vacancy mechanism (with AsV^- dopant-vacancy pair) is the predominant diffusion mechanism for As in Ge [41]. With different dominant diffusion mechanisms for As in Si and in Ge, there must be a transition in diffusion mechanisms for the alloy. This work is aimed at identifying this transition and to study the specific diffusion mechanisms for As in different SiGe alloy composition. In this chapter, the experimentally determined As diffusion parameters, interactions of As with native point defects, and diffusion mechanisms in $Si_{0.95}Ge_{0.05}$, close to the Si end of the composition, by considering simultaneous As, Si, and Ge diffusion under the intrinsic and extrinsic conditions using the established method with isotopically enriched layers described in Chapter 3 is presented. In Section 4.1, the experimental setup and conditions are discussed. Then, Si and Ge self-diffusion results are presented in Section 4.2. Finally, As diffusion results are elucidated in Section 4.3. Unfortunately, only samples with one alloy composition (SiGe with 5% Ge) were available due to difficulties in growing the specialized isotopically enriched samples. Chapter 6 will outline the future plans to study As diffusion in other alloy compositions.

4.1 Experimental conditions

The relaxed $^{nat}Si_{0.95}{}^{nat}Ge_{0.05}/^{28}Si_{0.95}{}^{70}Ge_{0.05}/^{nat}Si_{0.95}{}^{nat}Ge_{0.05}$ isotopically controlled multilayered structure described in Section 3.1 was used in the experiment. The schematic drawing of the structure and concentration profiles of Si and Ge isotopes as measured by secondary ion mass spectrometry (SIMS) have been shown previously in Figure 3.2 and 3.3. A Si-As alloy diffusion source was prepared by annealing a small piece of elemental As with a 15 mm x 5 mm high-resistivity float-zone (FZ) Si in a sealed quartz ampoule backfilled with 120 mTorr Ar at 1200°C for 1 hour. This Si-As alloy source was then placed in an evacuated quartz

ampoule (12 mm outer-diameter, 10 mm inner-diameter) backfilled with 120 mTorr Ar along with a 3 mm x 3 mm piece of SiGe sample. A piece of FZ Si with the same size as SiGe sample is also placed in the ampoule as references. The evacuated and Ar backfilled volume in the quartz ampoule is roughly 3-5 cm^3.

Diffusion anneals were performed at temperatures between 900°C and 1180°C for 8 days to 15 min in a Lindberg/Blue quartz tube furnace. A list of sample annealing temperatures and times is presented in Table 4.1. The diffusion temperatures were chosen such that they were close to equally spaced in one over the absolute temperature (1/T). The diffusion times were chosen such that the intrinsic diffusion lengths, $\sqrt{D_{As}^{Si}\, t}$, of As in Si were roughly the same. A type-S thermocouple placed right next to the ampoule was used to monitor the anneal temperature with ±2 K accuracy. The anneals were terminated by rapidly quenching the sealed ampoule under running water. Multiple uses of the same alloy source led to depletion of As in the source, thereby yielding different maximum As surface concentrations from above the intrinsic carrier concentration (n_i) to below n_i at diffusion annealing temperatures. After annealing, the diffusion profiles of ^{28}Si, ^{30}Si, ^{70}Ge, ^{74}Ge and ^{75}As were measured by dynamic SIMS at Evans Analytical Group in Sunnyvale, California and East Windsor, New Jersey or by time-of-flight SIMS (TOF-SIMS) at ION-TOF in Münster, Germany.

A typical diffusion profile after annealing as measured by SIMS is shown in Figure 4.1. ^{75}As in Figure 4.1 shows a typical box-shaped profile, indicating that diffusion occurred under extrinsic condition, i.e., As concentration at the surface is above that of the intrinsic carrier concentration at the annealing temperature (930°C). Similar to As in pure Si, the box-shaped diffusion profile in SiGe indicates that the point defects involved are negatively charged, thus, the diffusion is enhanced at high As concentration. As can be seen from Figure 4.1, Ge is depleted near the surface. This is possibly due to the surface decomposition and is often observed with extrinsic diffusion cases. The decomposition and its relation with surface As concentration is still under investigation. Self-diffusion and As diffusion results are presented and discussed in Section 4.1 and 4.2 below, respectively.

Table 4.1 Annealing temperatures and times for As in Si$_{0.95}$Ge$_{0.05}$. The third column indicates if the diffusion profile appears to be intrinsic (complimentary-error-function shaped) or extrinsic (box-shaped).

Annealing Temp (°C)	Annealing Time	Intrinsic/Extrinsic
900	192 hr	Intrinsic
900	192 hr	Intrinsic
930	96 hr	Extrinsic
930	100 hr	Intrinsic
930	102 hr	Extrinsic
950	114 hr	Intrinsic
965	45 hr	Extrinsic
980	24 hr	Intrinsic
1000	13 hr	Intrinsic
1000	17 hr	Extrinsic

1030	6 hr	Intrinsic
1035	8 hr	Extrinsic
1070	3 hr	Intrinsic
1150	30 min	Intrinsic
1180	15 min	Extrinsic
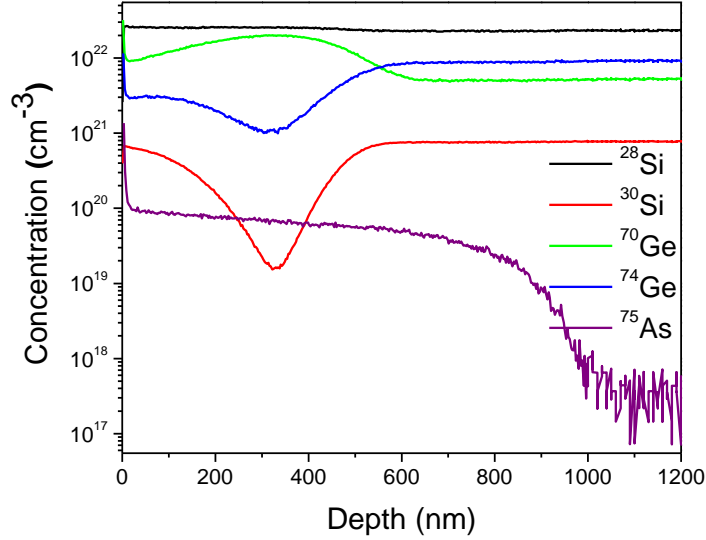
Figure 4.1 Concentration vs. depth profiles of ^{28}Si, ^{30}Si, ^{70}Ge, ^{74}Ge, and ^{75}As in the isotopically enriched heterostructure after 930°C 102 hr anneal as measured by SIMS. The box-shaped As profile indicates that the diffusion proceeded under extrinsic conditions. Ge is depleted near the surface, possibly due to surface decomposition.

4.2 Si and Ge self-diffusion in Si$_{0.95}$Ge$_{0.05}$

Self-diffusion of Si and Ge in SiGe alloys have been studied by various groups [92-95]. Here, we use the method established by our collaborators, R. Kube *et al*. [95], to analytically fit the diffusion broadenings of ^{30}Si and ^{74}Ge from the natural SiGe layers into the isotopically enriched layer. To demonstrate the analytical fitting method, the ^{74}Ge profile in the as-grown structure is reproduced in Figure 4.2 below. The concentration C_1 is defined as the concentration of ^{74}Ge in the top natural SiGe capping layer where as C_2 is the concentration in the isotopically enriched layer and C_3 is the concentration in the bottom natural SiGe layer. C_1 and C_3 are expected to be very similar if not the same. In addition, X_1 is defined as the depth of the start of the isotopically enriched SiGe layer and X_2 is the position of the end of the isotopically enriched layer where sample transition into the bottom natural SiGe layer. The diffusion profile of ^{74}Ge can then be analytically modeled as the sum of two error functions from the left and right sides of the isotopically enriched layer originally depleted with ^{74}Ge:

$$C_{^{74}Ge}(x) = \frac{C_3 + C_1}{2} + \frac{C_2 - C_1}{2} erf\left(\frac{x - X_1}{r_1}\right) + \frac{C_3 - C_2}{2} erf\left(\frac{x - X_2}{r_2}\right) \qquad (4.1)$$

Here, r_1 and r_2 are the absolute values of diffusion broadenings of ^{74}Ge at positions X_1 and X_2, respectively:

$$r_i = \sqrt{D_{Ge}(T)\, t} \qquad (4.2)$$

where $D_{Ge}(T)$ is the Ge diffusivity as a function of absolute temperature, T, and t is the annealing time. r_1 and r_2 are expected to be very similar in magnitude if the self-diffusivity is independent of the As concentration. This way, diffusivity of ^{74}Ge can be determined analytically by fitting the diffused profiles with Equations 4.1 and 4.2. Similarly, the diffusivity of ^{30}Si as a function of anneal temperature can be determined with the same method.
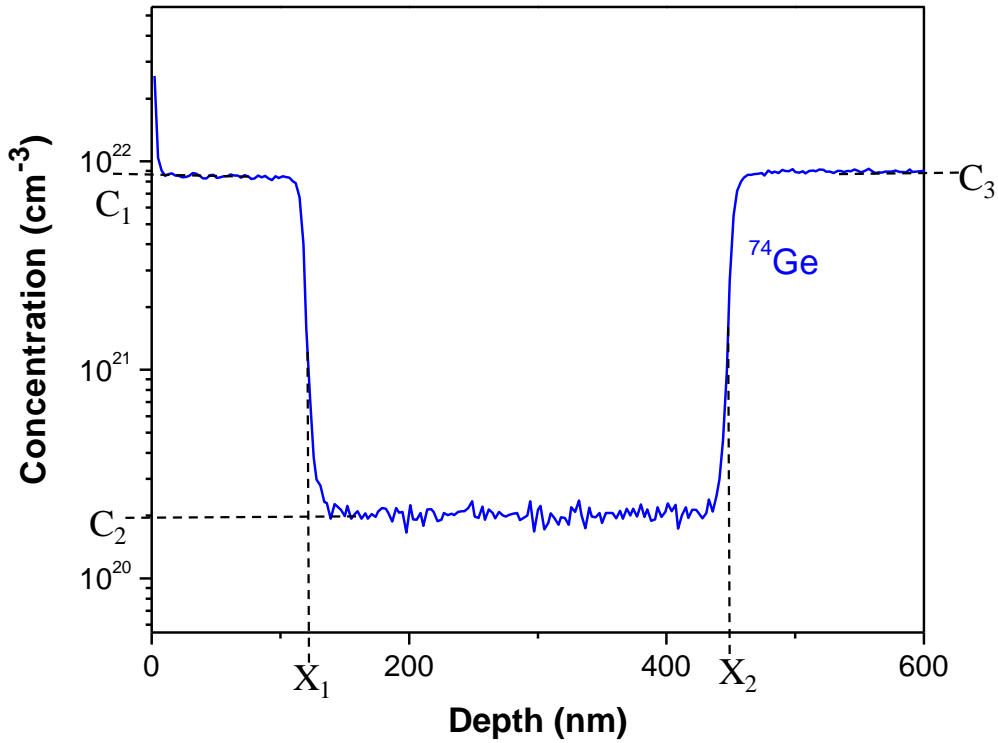
Figure 4.2 ^{74}**Ge concentration profile of the as-grown structure. Concentrations C$_1$, C$_2$, and C$_3$ as well as positions X$_1$ and X$_2$ are defined in the main text.**

The Arrhenius plot showing the analytically fitted and determined Si and Ge self-diffusivities is presented in Figure 4.3. The table in the figure shows the annealing temperature,

the annealing time, approximate annealing date, and approximate surface As concentrations. The SIMS profiles of the highlighted samples on the table were measured by dynamic SIMS at Evans Analytical Group (EAG) whereas the rest were measured at ION-TOF by TOF-SIMS. Si_r1 (Ge_r1) and Si_r2 (Ge_r2) represent diffusivities as determined from diffusion broadening at positions X_1 and X_2 from the ^{30}Si (^{74}Ge) concentration profiles, respectively. The data points shown in blue (Ge) and red (Si) are the self-diffusion results from R. Kube *et al.* [95] and can be directly compared with our results. Profiles of the samples with apparent surface Ge depletion were not fitted due to the breakdown of the analytical model. The temperature dependence of self-diffusivities of Si and Ge in $Si_{0.95}Ge_{0.05}$ as determined from the analytical fitting is found to be:

$$D_{Si\_analytical}(T) = 863 \exp\left(\frac{-4.82eV}{k_BT}\right) cm^2/s \qquad (4.3)$$

$$D_{Ge\_analytical}(T) = 1420 \exp\left(\frac{-4.82eV}{k_BT}\right) cm^2/s \qquad (4.4)$$

Here, k_B is the Boltzmann constant $= 8.617 \times 10^{-5}$ eV/K and T is the absolute temperature.
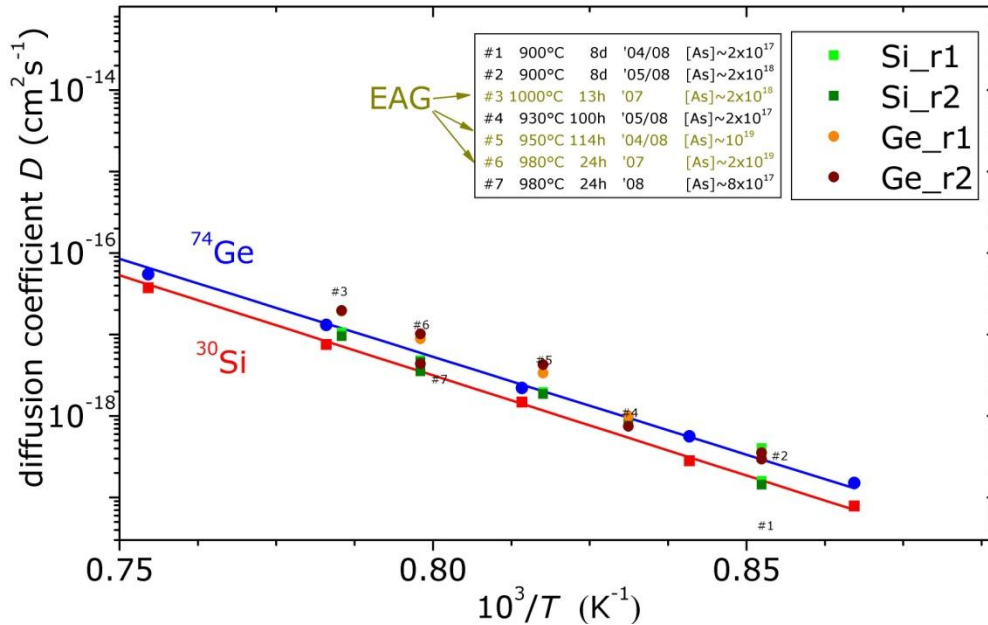

Figure 4.3 Diffusion coefficients of ^{74}Ge and ^{30}Si as a function of 1000/T. The blue and red data are from diffusivities determined without As from ref. [95].

The analytical model requires certain assumptions. First, the [74]Ge concentrations at X_1 and X_2 are assumed to be inexhaustible; the isotopically enriched layer is assumed to be sandwiched between two semi-infinite sources. Second, the transitions between natural SiGe layers and the enriched layer are assumed to be atomically abrupt, i.e., the dip in concentration profile shown in Figure 4.2 is a perfect box-shape. Given these assumptions, the self-diffusion parameters of $Si_{0.95}Ge_{0.05}$ with (this work) and without (ref. [95]) As doping seem to be very close; the effect of As doping on self-diffusion is minimal. Table 4.2 summarizes the diffusion enthalpy (H) and diffusion pre-exponential factor (D_0) of our results in comparison with the case of pure Si and that of $Si_{0.95}Ge_{0.05}$ without As doping as determined by R. Kube *et al*. [95].

Table 4.2 [30]Si and [74]Ge diffusion enthalpies and diffusion pre-exponential factors for pure Si, SiGe with 5% Ge, and As doped SiGe with 5% Ge.

	Si [95-96]		$Si_{0.95}Ge_{0.05}$ [95]		$Si_{0.95}Ge_{0.05}$:As [this work]	
	[30]Si	[74]Ge	[30]Si	[74]Ge	[30]Si	[74]Ge
H (eV)	4.76	4.83	4.82	4.77	4.82	4.82
D_0 (cm^2/s)	560	923	795	915	863	1420

Due to the limitations and assumptions, the analytical model may not be the best way to fit the experimentally measured profiles, especially for the samples with extrinsic As concentrations and surface Ge depletions. Numerical fitting was carried out by our collaborator, Professor Hartmut Bracht of University of Münster, and self-diffusivities as functions of temperature were obtained:

$$D_{Si\_numerical}(T) = 180^{+742}_{-145}\exp\left(\frac{-(4.63\pm0.18)eV}{k_BT}\right)cm^2/s \qquad (4.5)$$

$$D_{Ge\_numerical}(T) = 117^{+812}_{-102}\exp\left(\frac{-(4.54\pm0.22)eV}{k_BT}\right)cm^2/s \qquad (4.6)$$

The numerical model assumes no interactions between Si and Ge; a valid assumption because the two elements are completely miscible. Further, the numerical model includes an out flux of Ge to model the depletion of surface Ge observed for some of the samples with high As surface concentration. The details of the numerical fittings are beyond the scope of this work and will be published elsewhere. Some of the diffusion fittings will be presented in Apendix A. The fitting results show that the Ge self-diffusion activation enthalpy is lower than that obtained from the analytical model. This reflects the addition of an extra surface out flux term for Ge in

the numerical model due to surface degradation. Having a Ge flux leaving the material effectively lowers the Ge surface concentration, leading to a larger concentration gradient near the surface and therefore larger diffusivity and lower effective diffusion enthalpy.

It should be kept in mind that Ge diffusion is a random walk process; the larger concentration gradient is not a driving force for diffusion. Statistically, Ge in the high concentration region has a higher probability to diffuse and stay in the lower concentration region then the reverse process. The concentration gradient is just an easy way to describe the phenomenon empirically. The activation enthalpy obtained from numerical fitting for Si self-diffusion is similar to that obtained from analytical fitting within the experimental error. The self-diffusion activation enthalpies as determined from the numerical model are lower than those in pure Si; a trend that is expected for diffusion in SiGe. Further, the activation energies are determined to be slightly lower than those of the alloy samples without As doping; this suggests that the presence of As enhances self-diffusion slightly. However, this is difficult to prove using the existing structure because there doesn't seem to be any appreciable and obvious dependence of self-diffusivities on the initial surface As concentration. An isotopically enriched multilayer structure similar to the one shown in Figure 3.1 is needed to further understand the self-diffusion dependence on As concentration. In short, Si and Ge self-diffusivities in $Si_{0.95}Ge_{0.05}$ with As doping have been found to be very similar to those without As doping. Further, the self-diffusivities in $Si_{0.95}Ge_{0.05}$:As are slightly lower in magnitude than Si and Ge diffusivities in pure Si.

4.3   Arsenic diffusion in $Si_{0.95}Ge_{0.05}$

Arsenic diffusion profiles were measured by dynamic magnetic sector SIMS at Evans Analytical Group in New Jersey. The measuring conditions and beam dwell time were optimized to ensure high mass sensitivity needed to discern ^{75}As from ^{74}Ge + H. As mentioned in Section 4.1, both As diffusion profiles in the intrinsic and extrinsic conditions can be obtained by diluting the As-Si diffusion source. Figure 4.4 shows the As concentration profiles under the extrinsic diffusion condition. Under this condition, the As concentration profiles have the typical box-shape, indicating an enhanced As diffusion at high concentration. As with the case of As diffusion in pure Si demonstrated in Section 3.1, the box-shaped profiles is observed when As diffusion is enhanced by negatively charged defects because the concentrations of these defects are higher when the Fermi level lies close to the conduction band. From the dashed lines in Figure 4.4, one can clearly see that the diffusivity of As in pure Si is lower than that in $Si_{0.95}Ge_{0.05}$, following the trend observed in almost all impurity diffusions in $Si_{1-x}Ge_x$. To determine the intrinsic diffusivity, As diffusion profiles under intrinsic conditions are first analyzed.
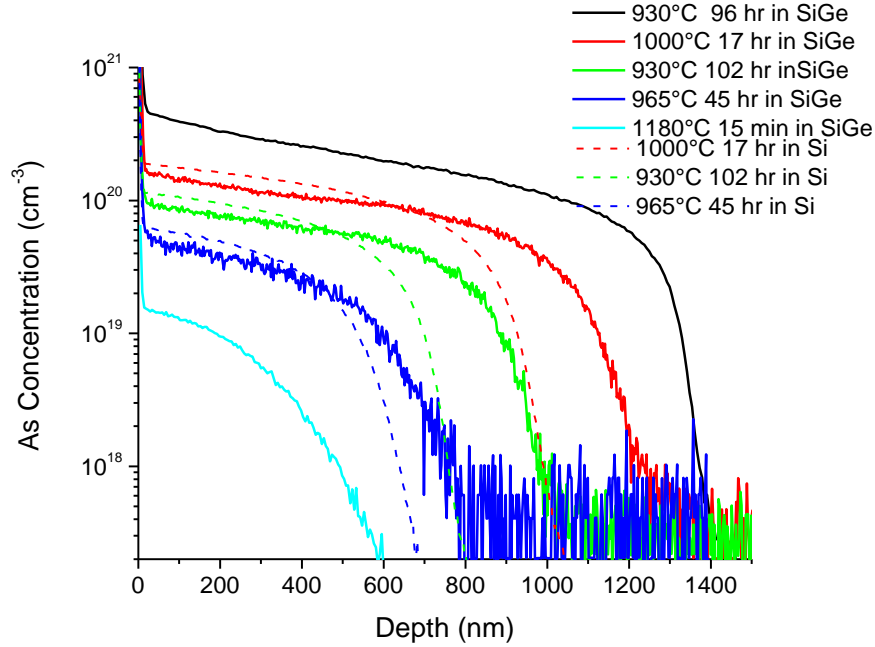
Figure 4.4 As concentration as a function of depth as measured by SIMS with magnetic sector mass spectrometer under the extrinsic diffusion condition. The solid lines are profiles of As in $Si_{0.95}Ge_{0.05}$ whereas the dashed lines are As in pure Si annealed in the same ampoule as the SiGe sample for a annealing temperature. The profiles are box-shaped typical for extrinsic diffusion. The diffusion temperatures and times are summarized in Table 4.1 above.

Contrary to the extrinsic As diffusion profiles shown in Figure 4.4, diffusion profiles under the intrinsic condition are much shallower and have complementary-error-function-like (erfc) shapes. The As concentration profiles as measured by magnetic sector SIMS after diffusion under intrinsic conditions are plotted in Figure 4.5. Only every fourth data point is plotted for clarity. The As concentration as a function of depth, x, and absolute temperature, T, can be analytically described by an erfc-type equation with the following form:

$$C_{As}(x,T) = C_0 erfc\left(\frac{x}{2\sqrt{D_{As\_analytical}(T)\,t}}\right)$$
(4.7)

Here, C_0 is the initial surface As concentration, $D_{As\_analytical}$ is the intrinsic As diffusivity, and t is the annealing time. This erfc-type equation is the solution to the Fick's Second Law of diffusion with inexhaustible source at x = 0. This is a good analytical model for the current experimental setups because the surface As concentration is controlled and maintained by the As partial pressure at the annealing temperature in the sealed ampoule. The As partial pressure is in turn dictated by As content in the original As-Si alloy diffusion source. The As partial pressure is believed to stay relatively constant throughout the annealing experiment to provide an inexhaustible As gas phase source.

a)
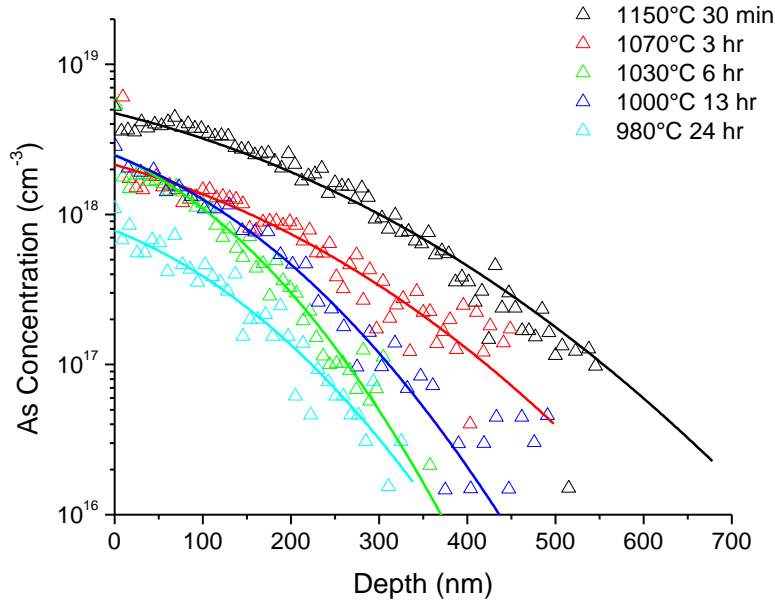
b)
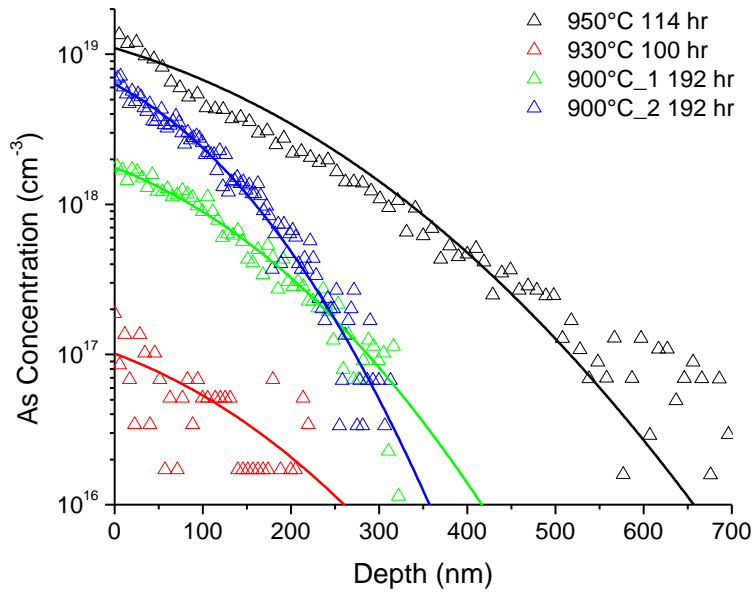
Figure 4.5 As concentration as a function of depth for intrinsic diffusion cases for diffusion temperature ranging from (a) 1150°C to 980°C and (b) 950°C to 900°C. The symbols are experimentally measured data by SIMS while the solid lines are analytical fittings with complementary error functions with the form described by Equation 4.7. Only every fourth experimentally measured data point is shown for clarity.

Equation 4.7 is used to fit experimentally measured As profiles using MathCAD with C_0 and $D_{As\_analytical}$ as the fitting parameters. The solid lines in Figure 4.5 show the analytically fitted complementary error functions. As can be seen from the figure, the complementary error functions fit the data very closely; validating the assumed infinite surface diffusion source model. Least-squares fittings with the Equation 4.7 yield $D_{As\_analytical}$ for each sample annealed at different temperatures. The As diffusivity as determined analytically as a function of 1000/T can be plotted.
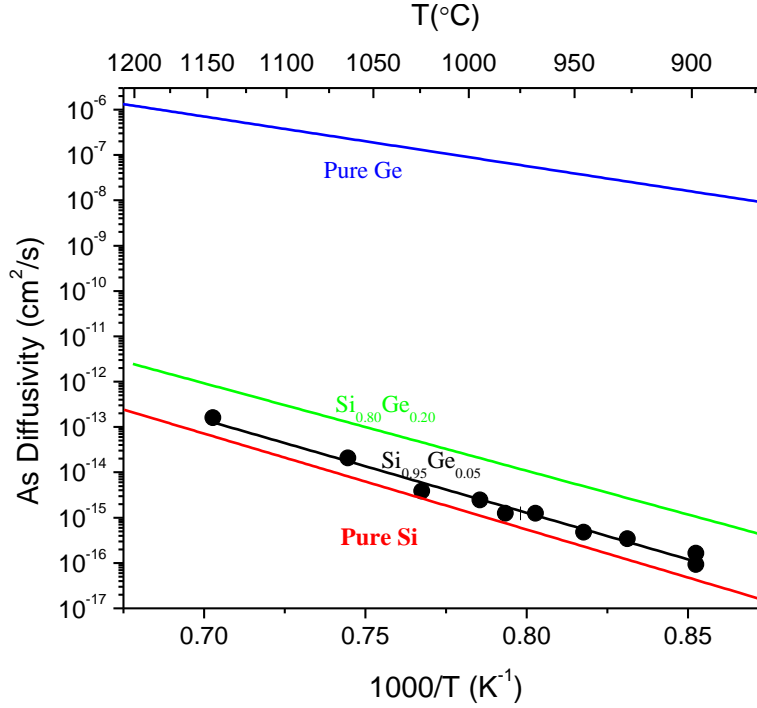
Figure 4.6 Intrinsic As diffusivity as a function of 1000/T in pure Si [51], Si$_{0.95}$Ge$_{0.05}$ (this work), Si$_{0.80}$Ge$_{0.20}$ [91], and pure Ge [41]. The black circles are D$_{As}$ as determined from analytical fitting of intrinsic As diffusion profiles in Si$_{0.95}$Ge$_{0.05}$ while the black solid line is the fitting for D$_{As}$ data points.

In Figure 4.6, one can observe that the intrinsic As diffusivity in SiGe with 5% Ge as determined from our analytical fittings falls nicely in the trend of increasing diffusivity as Ge content increases. The $D_{As\_analytical}$ data shown in Figure 4.6 from analytical fitting can be fitted with an Arrhenius relationship (black solid line):

$$D_{As\_analytical}^{Si_{0.95}Ge_{0.05}}(T) = 153\exp\left(\frac{-4.23eV}{k_BT}\right) cm^2/s \qquad (4.8)$$

The intrinsic As diffusion pre-exponential factor, D_0, and activation enthalpy, H, can be compared with those in pure Si, SiGe with 20% Ge, and pure Ge, as summarized in Table 4.3:

Table 4.3 Intrinsic As activation enthalpies, H, and pre-exponential factor, D_0, for $Si_{1-x}Ge_x$ for x=0 (Si), x=0.05, x=0.2, and x=1(Ge).

	Si [51]	$Si_{0.95}Ge_{0.05}$	$Si_{0.80}Ge_{0.20}$ [91]	Ge [41]
H (eV)	4.20	4.23	3.83	2.71
D_0 (cm²/s)	47	153	30	32

The activation enthalpy, 4.23 eV, obtained from the experiment in $Si_{0.95}Ge_{0.05}$ is slightly higher than that in pure Si. However, the difference is within the experimental error typical in diffusion experiments. It shows that the As migration barrier with the addition of 5% Ge into a Si lattice remains largely unchanged. However, the diffusion pre-exponential factor, D_0, is slightly higher in $Si_{0.95}Ge_{0.05}$. As can be seen from Equation 2.14, a higher D_0 indicates higher formation and migration entropy, intuitively consistent with the introduction of Ge into the Si matrix. It should be noted, however, that experimentally determined D_0 values can easily vary by an order of magnitude depending on the fitting of the slope, or the activation enthalpy, of the Arrhenius plot. Therefore, over-interpretation of the physical meanings of D_0 value must be avoided. The analytically determined results are compared with those obtained by numerical fittings below.

As with self-diffusion, numerical fitting is also performed by our collaborators in Münster, Germany. In the numerical model, As diffusion mechanisms similar to those in pure Si are used. Namely, mobile dopant-defect species $(AsV)^0$, $(AsV)^-$ and $(AsI)^0$ are considered. Reactions to describe these mobile species are exactly the same as in Equations (3.1ab) and (3.2), the ones used to describe As diffusion in Si:

$$(AsV)^0 \Leftrightarrow As_s^+ + V^- \tag{4.9a}$$

$$(AsV)^- \Leftrightarrow As_s^+ + V^{--} \tag{4.9b}$$

$$(AsI)^0 \Leftrightarrow As_s^+ + I^0 + e^- \tag{4.10}$$

$$(As_2V)^0 \Leftrightarrow 2As_s^+ + V^{--} \tag{4.11}$$

One other clustering reaction (4.11) is also considered. It is found in As diffusion in pure Ge that As_2V clustering is important for high As concentrations [97]. A. Chroneos *et al*. has also shown that, theoretically, it is favorable for the formation of such clusters in Ge [98]. Although the charge state of this cluster defect is still unverified, here we assume it to be neutral. For comparison, the As diffusion in pure Ge, known to diffuse via the vacancy-mechanism, can be

accurately described by reactions (4.9b) and (4.11) alone [41]. Again, the assignment for the charge states is tentative; however, some experimental evidences from the works by our collaborators in studying simultaneous self- and As diffusion in Ge isotope structures suggest that vacancies in Ge are doubly negatively charged [41, 99-100], at variance with an earlier study on self-diffusion [101].

The details of the numerical fitting are beyond the scope of this work and will be published elsewhere. Here, the profiles and the numerical fitting results of the 1035°C 8 hours annealed sample is shown in Figure 4.7 to represent a typical numerical fitting result. The solid black lines in the figure are the experimentally measured ^{30}Si, ^{74}Ge, and ^{75}As profiles. The colored solid lines are numerical fittings obtained by considering reactions (4.9a)-(4.11). The two dashed lines represent numerical As profile fitting without the consideration of As$_2$V clustering and the contribution from the clustering. Obviously from the figure, As$_2$V clustering needs to be considered to accurately fit the As profile near the surface. Overall, the numerical analysis modeling reactions (4.9a)-(4.11) fit the experimentally measured profiles very closely.
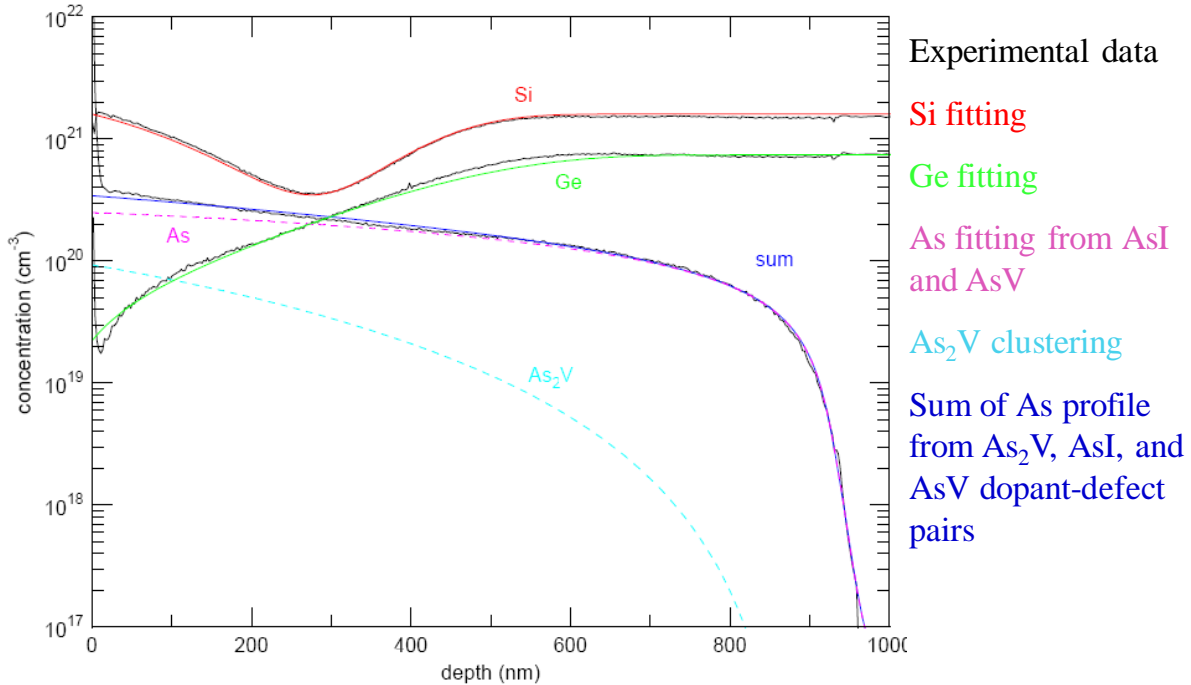
Figure 4.7 Concentration vs. depth of experimentally determined ^{30}Si, ^{74}Ge, and ^{75}As profiles along with numerical fitting results for As in Si$_{0.95}$Ge$_{0.05}$ sample annealed at 1035°C for 8 hours under the extrinsic diffusion condition.

The intrinsic As diffusion coefficient can be obtained from the numerical fitting by summing the diffusivities of $(AsV)^0$, $(AsV)^-$, $(AsI)^0$, and $(As_2V)^0$ mobile dopant-defect species for each temperature. The resulting intrinsic As diffusion coefficients obtained from the numerical fitting are plotted in an Arrhenius plot in Figure 4.8. A line can be least-squares fitted through the data points which yield one Arrhenius relationship for the intrinsic As diffusivity as a function of temperature:

$$D_{As\_numerical}^{Si_{0.95}Ge_{0.05}}(T) = 129_{-107}^{+628} \exp\left(\frac{-(4.27 \pm 0.19)eV}{k_B T}\right) cm^2 / s \qquad (4.12)$$

The relatively large error is a result of the scattering in the numerically determined As diffusivities which include errors from the uncertainties in SIMS measured data. It is especially difficult to distinguish ^{74}Ge+H and ^{75}Ge, resulting in large noise and high baseline for SIMS measured As profiles. The As diffusivity obtained from the sample annealed at 1035°C shows a large deviation from the overall results shown in Equation (4.12). This particular experimental condition will be repeated in the future. Nevertheless, the intrinsic As diffusivity in $Si_{0.95}Ge_{0.05}$ as a function of temperature obtained numerically (Equation 4.12) and analytically (Equation 4.8) agree with each other very well. The agreement boosts the confidences in both of the two very different analysis methods.
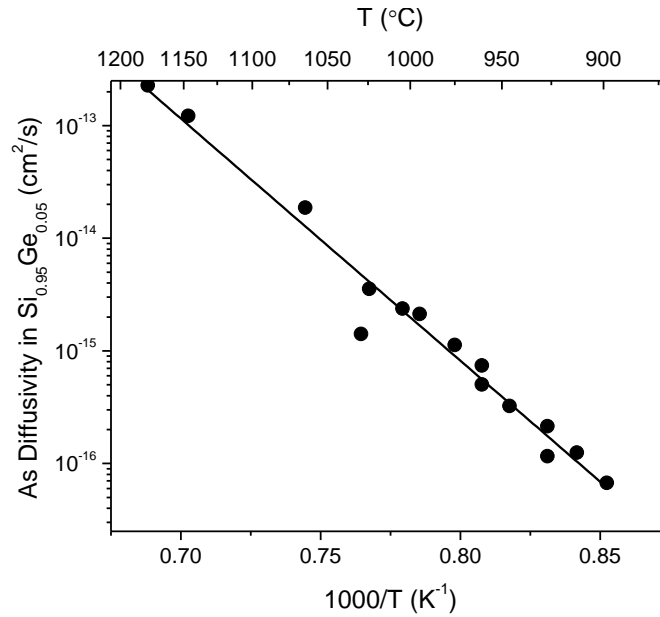
Figure 4.8 Intrinsic As diffusion coefficients as a function of 1000/T as determined from the numerical fittings.

In summary, As in $Si_{0.95}Ge_{0.05}$ diffuses very similar to As in pure Si. The diffusion mechanisms are virtually the same: a combination of vacancy mechanism and interstitialcy mechanism. The charge states for the defect pairs are the same as well. The only difference is a slight contribution from the $(As_2V)^0$ clustering. The clustering is observed in As diffusion in pure Ge; therefore, it is expected that the contribution will increase as Ge content increases in As diffusion in SiGe alloys. The As diffusion activation enthalpies of different alloy compositions are plotted in Figure 4.9 for comparison. Considering errors, our As diffusion in $Si_{0.95}Ge_{0.05}$ study falls in the trend of decreasing activation enthalpy as Ge content increases. As discussed above, to see the transition from the combination of vacancy mechanism and interstitial

mechanism of As diffusion in Si to the predominantly vacancy mechanism of As diffusion in Ge, isotopically enriched multilayer samples with other alloy compositions are needed. A similar method can also be extended to study other common dopants in Ge.
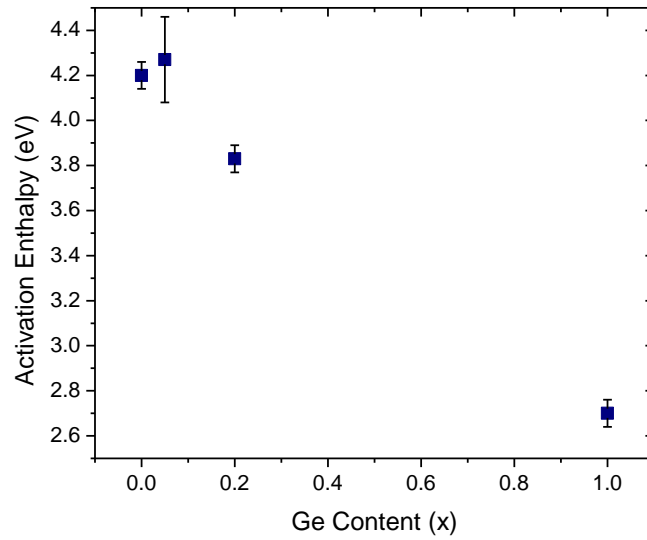
Figure 4.9 As diffusion activation enthalpies as a function of Ge content in Si$_{1-x}$Ge$_x$ for pure Si [51], Si$_{0.95}$Ge$_{0.05}$ [this work], Si$_{0.80}$Ge$_{0.20}$ [91], and pure Ge [41].

Chapter 5 Diffusion in Germanium

This chapter focuses on the diffusion in germanium under equilibrium and non-equilibrium conditions. As discussed in Chapter 1, Ge has the potential to replace Si in the new generations of microelectronic devices because of its higher electron and hole mobilities. As in the case of Si, successful implementation of Ge-based devices demand the precise control of dopant distributions during fabrication and any subsequent thermal processing steps. This precise engineering control requires a thorough understanding of the atomic diffusion mechanisms in Ge.

As mentioned in Chapter 2 and 3, diffusion in Ge is predominantly mediated by the vacancy mechanism while the role of the self-interstitials is largely unknown. This is most likely due to the low equilibrium concentration of self-interstitials that is well below the detection limits of the spectroscopic techniques usually employed to study point defects in semiconductors. Nevertheless, being an equilibrium intrinsic point defect, thermodynamically, the self-interstitials must exist at any finite temperature. The goal of this work is to study the effects of self-interstitials for diffusion in Ge by intentionally introducing excess point defects with concentrations well above that of the equilibrium values by proton irradiation. In this chapter, Section 5.1 provides a brief literature survey of self- and impurity diffusion and diffusion mechanisms in Ge under the equilibrium condition. This section will also show that, because of the dominance of the vacancy mechanism for diffusion in Ge, the size and the charge state of substitutional impurities can provide clues for their diffusion coefficients relative to each other. Section 5.2 will discuss our work on proton radiation enhanced self- and impurities diffusion with focus on boron diffusion in Ge.

5.1   Equilibrium diffusion in Germanium

Under equilibrium conditions, the diffusion of self atoms and most substitional impurities are mediated by the vacancy mechanism [34, 53, 102]. In 1985, M. Werner *et al.* showed with a radioactive [71]Ge tracer diffusion experiment that the self-diffusivity of Ge depends on the doping of the crystal [101]. They showed the Ge self-diffusion coefficient is the lowest for p-type Ge and increases with n-type doping ($D_{Ge}^{SDp} < D_{Ge}^{SDi} < D_{Ge}^{SDn}$). This clearly implies that vacancies in Ge are negatively charged. When the crystal is doped, say, n-type, the Fermi level shifts closer to the conduction band due to the increase in the electron concentration. This shift in the Fermi level also affects the concentration of the charged vacancies. As a result, the concentration of negatively charged vacancies will increase while the concentration of neutral (and therefore unaffected by the Fermi level) vacancies remains unchanged. Thus, the Ge self-diffusion is enhanced by the increased negatively charged vacancy concentration. Werner *et al.* concluded that the self-diffusion process was mediated by neutral (V^0) and singly negatively charged (V^-) vacancies in Ge [101].

More recent experiments, however, show that the vacancy diffusion mechanism is predominantly assisted by doubly negatively charged vacancies. Experiments using isotopically enriched layers to study simultaneous dopant and Ge self-diffusion show that the charge state

difference in the dopant-vacancy pairs and the vacancies is one [99-100]. From the experiments, the researchers determined that the dopant-vacancy pairs are singly negatively charged, therefore the vacancies involved in the diffusion process must be neutral (V^0) and doubly negatively charged (V^-) [99-100]. Other studies of donors and acceptors diffusion in Ge also confirm that the dominant charge state for vacancies in Ge is doubly negative [41, 103-105].

Figure 5.1 below shows the intrinsic diffusivities of common impurities in Ge relative to the self-diffusivity as a function of temperature in an Arrhenius plot. The solid lines indicate the diffusivities of substitutional impurities where as the short-dashed lines represent small impurities (H and Fe) diffuse by the pure interstitial mechanism. The long-dashed lines represent impurities diffusing by the hybrid mechanism of dissociative diffusion where the foreign atoms occupy substitional sites but diffuse interstitially. The upper short-dashed line shows the diffusivity of interstitial Cu_i deduced from Cu diffusion experiments [106]. Diffusion of Cu_i appears to be the fastest, even faster than H diffusion in Ge. It is evident from Figure 5.1 that Si and B appear to diffuse more slowly than self-diffusion in Ge, contrary to the case in Si where the diffusivity of impurities always exceeds self-diffusion for a given temperature [51]. This can be explained by the fact that both interstitial- and vacancy-mediated mechanisms contribute to the self-diffusion in Si [44, 51, 96]. For a given impurity in Si, either interstitials or vacancies or both can be assisting the diffusion causing it to diffuse faster than Si self atoms. Assuming only the vacancy mechanism dominates the diffusion processes in Ge, the lower diffusivities of B and Si relative to the self-diffusion suggests a repulsive force between the vacancy and the impurity atom [107]. It is noted that B diffusion coefficients are the lowest among all common impurities by several orders of magnitude, suggesting a very different diffusion mechanism may be dominant [78].
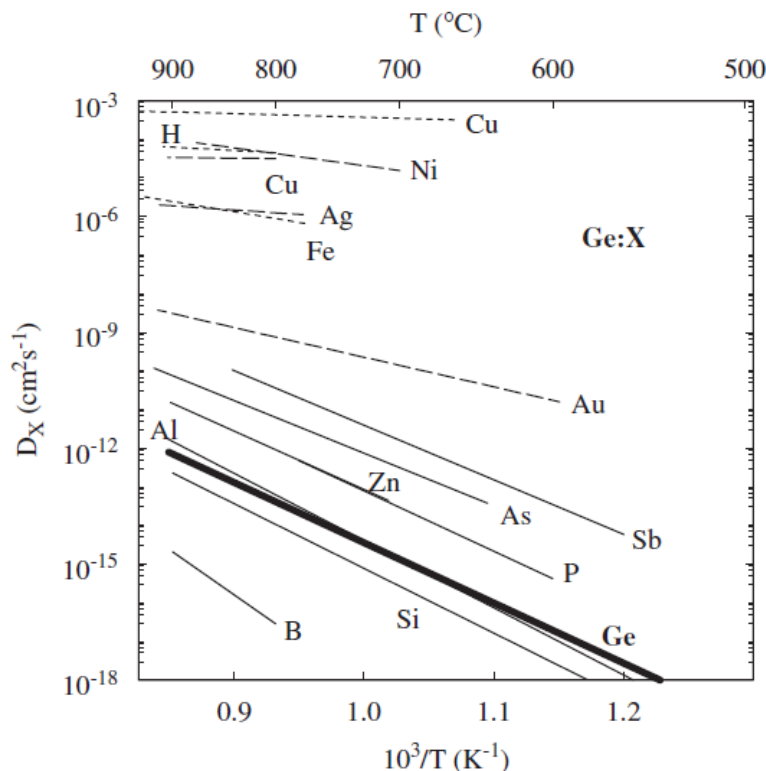
Figure 5.1 Temperature dependence of the diffusion coefficient of common impurities in Ge (thin lines) compared with the self-diffusion (thick line). (from ref. [107] and refs therein).

To compare diffusion in Si and Ge, it is useful to plot the diffusivities of impurities as a function of homologous temperature (T_m/T). In this way, the effect due to the difference in the melting temperatures of Ge ($T_m = 1210$ K) and Si ($T_m = 1685$ K) is eliminated. Figure 5.2 shows such a plot with some common impurities in Si and Ge. The diffusivities of impurities in this normalized homologous temperature Arrhenius plot provide rough clues of the underlying diffusion mechanisms for the impurities. As can be seen from Figure 5.2, the diffusivities of purely interstitial diffusers such as Fe and Cu_i in Si and Ge are of similar magnitude. This is also true for As in Si and Ge, suggesting that the diffusion mechanisms are similar [107]. On the other hand, the diffusivity of Zn in Si and Ge differ by orders of magnitude. This can be explained by the difference in mechanisms mediating the Zn diffusion. Zn is a deep acceptor in Si which diffuses by the hybrid kick-out and dissociative mechanisms [108]. As stated before in Chapter 2, hybrid diffusion mechanisms usually lead to fast diffusion because the impurities diffuse interstitially once they are out of the substitutional lattice site. In contrast, Zn in Ge is a semi-shallow double acceptor which diffuses, as with other substitional impurities, by the slow vacancy mechanism [107]. In this context, it is interesting to note, again, the difference between the diffusivity of B in Ge and Si. Boron acts as a shallow acceptor in both Si and Ge but diffuses considerably more slowly in Ge. B diffusion in Si is known to be assisted by Si self-interstitials via the interstitialcy mechanism [51]. On the other hand, it is well-established that Ge self-interstitials play a minimal role for diffusion in Ge under thermal equilibrium conditions. The high activation enthalpy of B diffusion in Ge suggests that self-interstitial assisted interstitialcy mechanism must be considered [78].
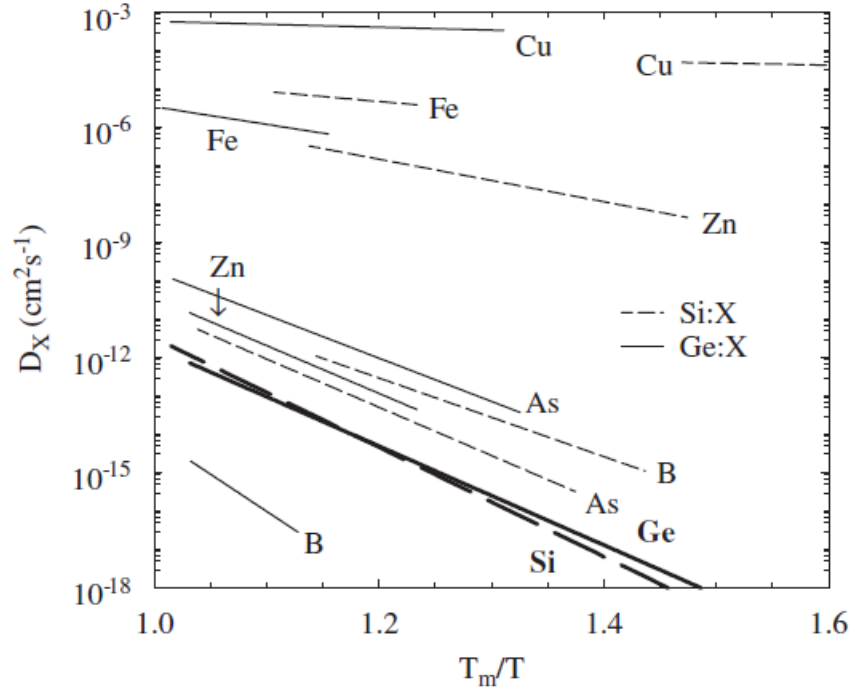
Figure 5.2 Self- and impurities diffusivities in Si and Ge as a function of normalized homologous temperature T_m/T. The solid lines show the diffusivities in Ge whereas the dashed lines represent diffusivities in Si. (from ref. [107] and refs therein).

Because of the predominant vacancy diffusion mechanism in Ge, the charge state and the size of the diffusing impurity atom can also provide insights into the diffusion activation enthalpy and the diffusivity of the diffusing species. It is practical to separate the interactions of a substitutional atom and a vacancy into two categories, Coulomb and elastic [105]. At typical diffusion temperatures, the charge state of group III ionized acceptors is -1 and of group V donor impurities is +1. Given that the vacancies assisting diffusion are mainly negatively charged in Ge, the columbic force between an ionized donor and a vacancy is generally attractive whereas the force is repulsive between an ionized acceptor and a vacancy.

This can be seen from the general trend that the activation enthalpies of group V donors are lower than the activation enthalpies of isovalent group IV impurities which are lower than the activation enthalpies of group III acceptors. Table 5.1 below summarizes the activation enthalpies of common impurities in Ge clearly showing the trend: $H_{GroupV} < H_{GroupIV} < H_{GroupIII}$. The fast diffusion of group V donors along with deactivation at high concentrations are some of the leading problems for the difficulty in making n-type Ge based MOSFETs. Similar to diffusion, the electrical deactivation of dopants is found to be dependent on dopant-defect interactions [109]. The deactivation of donors is believed to be caused by the clustering with vacancies to form neutral donor-vacancy pairs: $(DV)^- + D_S^+ \leftrightarrow (D_2V)^0$ where D is a donor and D_S a donor on a substitutional site [100]. This provides yet another motivation to study and understand the native point defects in Ge for defect engineering in order to decrease donor diffusion and increase electrical activation.

Table 5.1 Diffusion activation enthalpies of common impurities in Ge

	Group III			Group IV			Group V		
	B	**Al**	**Ga**	**Si**	**Ge**	**Sn**	**P**	**As**	**Sb**
Ref.	[78]	[110]	[105]	[111]	[112]	[105]	[100]	[100]	[100]
H (eV)	4.65	3.45	3.31	3.32	3.05	2.90	2.85	2.71	2.55

The elastic contribution for the diffusion activation enthalpy can be qualitatively explained by the size of the substitutional impurity. The elastic interaction originates from the elastic strain caused by the substitutional impurity and the vacancy on the otherwise perfect Ge lattice. For instance, an impurity smaller than Ge sitting on a lattice site would cause local tensile strain around the site, therefore, it tends to repel vacancies (voids on the lattice sites) which would distort the local lattice further. Because of this repulsion, the diffusion activation enthalpy is higher for a smaller impurity atom in the same group. This trend is apparent from Table 5.1 above. The temperature dependent diffusivities for common group III acceptors, group IV atoms, and group V donors are plotted in Figure 5.3 (a), (b), and (c), respectively, to further demonstrate this trend.

b)

c)
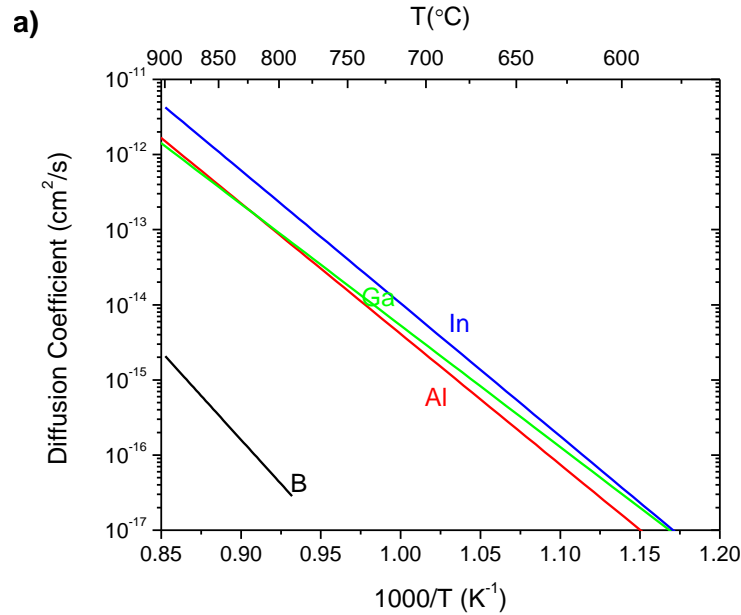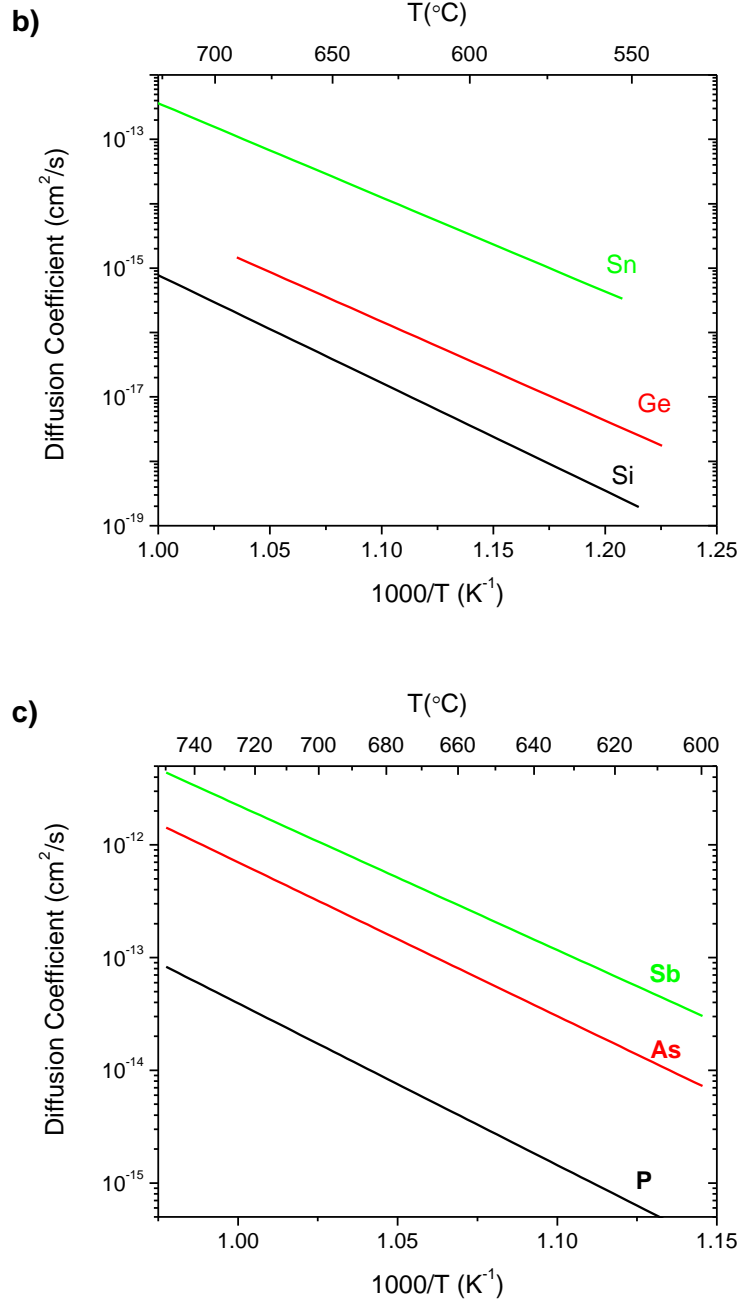
Figure 5.3 Diffusion coefficients as a function of 1000/T for (a) group III acceptors (b) group IV atoms and (c) group V donors in Ge. Indium results are from [103]. The references for other impurities are given in Table 5.1.

From Figure 5.3b and 5.3c, lower diffusivity for smaller atoms can clearly be observed for group IV ($D_{Si} < D_{Ge}^{SD} < D_{Sn}$) and group V ($D_P < D_{As} < D_{Sb}$) impurities. In fact, Brotzmann *et al.* found that carbon, the smallest group IV impurity, appears to be immobile up to 750°C (~85% of Ge melting temperature) [100]. The trend is less clear for group III acceptors. As can be seen, even though the trend still persist for most part, namely larger atoms diffuse faster at a given

temperature, Al, Ga, and In diffusion coefficients in Ge are all very similar. This may be due to the fact that the columbic repulsion interaction between the negatively charged ionized acceptors and the negatively charged vacancies are dominant, leaving the elastic interactions a secondary effect.

Boron diffusion in Ge is a unique case worthy of special attention. With a diffusion activation enthalpy of 4.65 eV, it is the slowest diffusing species among common impurities in Ge. The diffusion coefficient is several orders of magnitude lower than other acceptors and Ge self-diffusion. Both experimental [78] and theoretical [113-114] studies of B diffusion in Ge suggest that self-interstitial mediated diffusion mechanisms may be dominant. This is also supported by the theoretical results of the study by Carvalho *et al*. [70] identifying that the self-interstitials in Ge are positively charged; thus, the columbic interaction between the self-interstitials and the negatively charged B is energetically more favorable. Further, from the size argument, a self-interstitial is more favorable in relieving the local tensile strain created by the small substitutional boron in the lattice. However, as mentioned in Section 2.2 and 3.2, the equilibrium concentration of Ge self-interstitials is too low. Therefore, to test the hypothesis that boron diffusion is mediated by self-interstitials in Ge, excess interstitials well above the equilibrium concentration must be introduced. Section 5.2.2 will describe and discuss our work in studying boron diffusion in Ge under proton irradiation to intentionally introduce self-interstitial concentrations well above the equilibrium value.

5.2   Non-equilibrium diffusion in Ge under proton irradiation

In order to investigate the impact of self-interstitials on diffusion in Ge, diffusion experiments under a constant proton beam are performed. Unlike in the case of Si, implantation damage does not contribute any significant transient enhanced diffusion (TED) in Ge [115-116]. In fact, it is generally believed that the implantation damage recovers fast even at low temperatures in Ge [115-116]. Therefore, in order to study interstitial-impurity diffusion interactions, diffusion experiments must be carried out under a constant proton irradiation such that a steady source of self-interstitials can be maintained. This radiation enhanced diffusion experiment has been established as a practical way to study point defect-impurity diffusion interactions normally not available under equilibrium conditions [42, 117-119]. Section 5.2.1 will elucidate the radiation enhanced Ge self-diffusion experiments performed by our collaborators in Münster [42, 118] while Section 5.2.2 will discuss our work of radiation enhanced boron diffusion in Ge. The results of the radiation effect study performed in Münster on P diffusion in Ge will also be discussed briefly.

5.2.1   Radiation enhanced self-diffusion

This section describes the radiation enhanced self-diffusion experiments in Ge performed by our collaborators, S. Schneider, H. Bracht, *et al*., at the University of Münster in Germany. The experiments and the analysis are briefly presented because they form the basis for the study of proton irradiation enhanced B diffusion. More detailed descriptions are found in ref. [118] and [42].

For the experiments, an isotopically enriched multilayer structure consisting of [70]Ge and natural Ge grown by MBE was utilized. The structure has 20 alternating layers of 96% enriched

[70]Ge and natural Ge where each layer is about 15 nm thick. The distribution of [74]Ge in the as-grown multilayer structure as measured by SIMS is illustrated as the short dashed line in Figure 5.4. Part of the sample is then subjected to proton irradiation with 2.5 MeV in energy and 1.5 μA beam current through a 10 mm circular aperture. As discussed in Section 3.2, this beam condition yields a proton flux of 1.18×10^{13} H$^+$/cm^2-s and a vacancy-interstitial pair creating rate of 2.1×10^{16} vacancies/cm^3-s for the irradiated region. The sample with a 3 mm diameter circular irradiated area was heated to 600°C for 90 min by the in-situ vacuum heater. The [74]Ge profiles from the annealed and irradiated part of the sample is plotted as red circles whereas the covered (therefore non-irradiated) and annealed part is shown in blue squares in Figure 5.4.
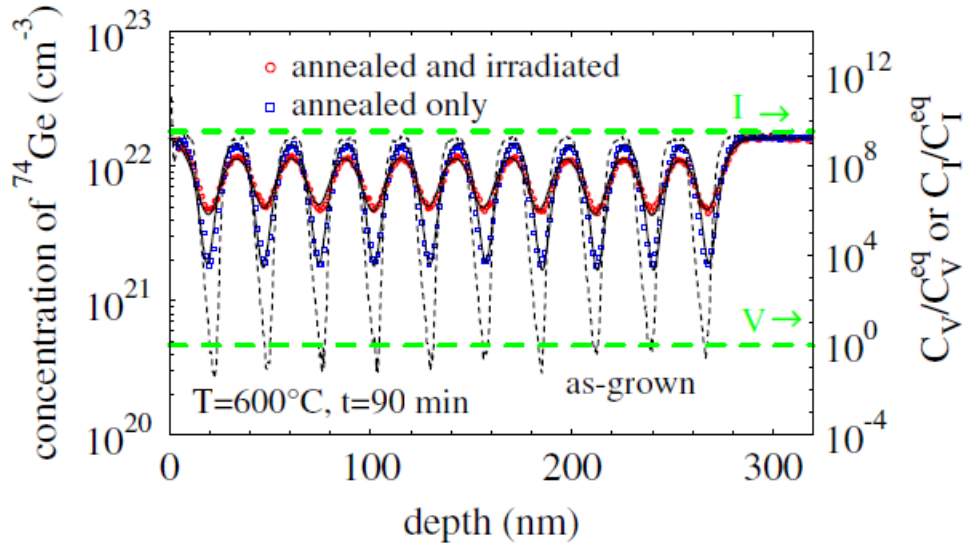
Figure 5.4 Concentration profiles of [74]Ge measured by SIMS for the as-grown structure (short dashed-line), the part of the sample annealed and irradiated (red circles) by the proton beam, and the part covered and annealed only (blue squares). The black solid lines are diffusion simulations considering differential equations (5.1)-(5.3). The green dashed-lines are the supersaturation concentrations of self-   interstitials and vacancies as determined from the simulation. The right y-axis is for the supersaturation values. (from ref. [42]).

It is obvious from Figure 5.4 that the part of the sample exposed to the proton beam shows larger diffusion broadening (red circles). This unambiguously demonstrates an enhanced self-diffusion under proton irradiation. To analyze the enhanced diffusion, the following Fick's-Second-Law-type differential equations describing the self-diffusion are proposed to numerically simulate the experimental results:

$$\frac{\partial C_I}{\partial t} = D_I \frac{\partial^2 C_I}{\partial x^2} + k_0 - k_{IV} C_V(x,t) C_I(x,t) \tag{5.1}$$

52

$$\frac{\partial C_V}{\partial t} = D_V \frac{\partial^2 C_V}{\partial x^2} + k_0 - k_{IV} C_V(x,t) C_I(x,t) \qquad (5.2)$$

$$\frac{\partial C_{Ge}}{\partial t} = \frac{\partial}{\partial x} D_{Ge} \frac{\partial C_{Ge}}{\partial x}. \qquad (5.3)$$

In Equations (5.1) and (5.2), k_0 is the point defect generation rate calculated from SRIM to be 2.1 $\times 10^{16}$ defects/cm^3-s and k_{IV} is the defect annihilation rate. k_0 is the same for self-interstitials (I) and vacancies (V) since the proton irradiation creates V and I simultaneously. Assuming Equation (2.9) holds true, the annihilation rate, k_{IV} is given by:

$$k_{IV} = 4\pi r(D_I + D_V)C_0 \qquad (5.4)$$

where r is the capture radius, assumed to be one lattice constant of Ge in the analysis, and C_0 is the Ge atomic density (4.41×10^{22} cm^{-3}). From Equation (2.18), D_{Ge} in Equation (5.3) can be written as:

$$D_{Ge}(x,t) = f_V C_V D_V + f_I C_I D_I = 0.5 S_V \frac{C_V^{eq} D_V}{C_o} + 0.73 S_I \frac{C_I^{eq} D_I}{C_o}. \qquad (5.5)$$

Here, S_V and S_I are defined as the local supersaturation of V and I, respectively:

$$S_{V,I} = \frac{C_{V,I}(x,t)}{C_{V,I}^{eq}} \qquad (5.6)$$

Substituting in Equation (2.20), Equation (5.5) can be rewritten in terms of Ge equilibrium self-diffusivity:

$$D_{Ge}(x,t) = S_V D_{Ge}^{eq} + 0.73 S_I \frac{C_I^{eq} D_I}{C_o}. \qquad (5.7)$$

To solve the differential equations, a few boundary conditions are imposed:

$$C_{V,I}(x,0) = C_{V,I}^{eq} \qquad\qquad (5.8)$$

$$C_I^{eq}D_I << C_V^{eq}D_V \qquad\qquad (2.21)$$

Equation (5.8) simply states that at time zero, the local concentrations for V and I are at their equilibrium values. The second boundary condition (2.21) is the result from the equilibrium self-diffusion studies. While C_V^{eq} at 600°C can be obtained from the literature [53], C_I^{eq} is not available in the literature and is used as the free fitting parameter. Finally, since $C_I^{eq}D_I$ is inseparable, the following assumption is made for this analysis:

$$\frac{C_I^{eq}D_I}{C_o} = 5 \times 10^{-22} \, cm^2 s^{-1} \qquad\qquad (5.9)$$

The assumption is made for the sake of analysis and has no real physical basis. This reflects one of the difficulties in studying Ge diffusion: the lack of knowledge about the equilibrium concentration of self-interstitials. With the assumptions and boundary conditions, the diffusion profiles can be numerically simulated (shown as black lines in Figure 5.4) and supersaturation values (S_V and S_I) obtained (green dashed-lines) using a differential equation solver software package, ZOMBIE [120], specifically designed for diffusion simulations.

From the simulation, one of the most striking results is the fact that the supersaturation for self-interstitials (S_I) is much higher than that of the vacancies. Obviously, the exact supersaturation values depend on assumptions made in Equation (5.9). Nevertheless, the supersaturation of interstitials is expected to be high because of the presumably low equilibrium self-interstitial concentration. On the other hand, the supersaturation of vacancies (S_V) is close to unity. A surprising observation is the homogenous broadening of all [74]Ge peaks in the isotopically enriched structure regardless of the location. This homogeneous broadening is reflected in the numerical simulations of the supersaturation values being independent of the depth for both vacancies and interstitials. This indicates that no gradient in the concentration of the native point defects versus depth exists. In the case of Si, the surface acts as a sink for both vacancies and interstitials created under the proton irradiation [117]; in other words, the concentrations of vacancies and interstitials approach that of the equilibrium values at the surface. If that were true for Ge, a slower diffusion and therefore less diffusion broadening of the peaks near the surface would have been observed. The homogeneous broadening suggests that the surface is not at the equilibrium state and may acts as a reflecting boundary for interstitials and/or vacancies. In order to identify the surface condition, additional experiments with impurities diffusing predominantly by interstitial assistance are needed. Boron diffusion experiments are ideal to identify the dominant impurity in assisting diffusion as well as clarifying the surface boundary conditions. Regardless of the surface conditions, a conclusion can be reached: self-diffusion is enhanced by the excess interstitials. In other words, as in the case of Si self-diffusion, Ge self-diffusion is assisted by both vacancies and interstitials. The contribution

from self-interstitials is negligible in equilibrium conditions because the equilibrium interstitial concentration is too low to be effective in mediating diffusion.

5.2.2   Radiation enhanced boron diffusion

For the proton irradiation enhanced boron diffusion experiment, we utilized a molecular beam epitaxy (MBE) grown boron doped Ge structure. The structure contains six boron doped layers each about 25 nm thick, each of the layers is separated by 100 nm undoped Ge. The structure was then capped with a 100 nm undoped Ge top layer, bringing the total thickness of the structure close to 800 nm. Figure 5.5 below shows the concentration profile of B in Ge for the as-grown structure measured with secondary ion mass spectrometry (SIMS). As can be observed from the figure, the B concentration in the doped layers reaches close to 3×10^{19} cm^{-3}, at least two orders of magnitude above the background doping level, providing a good dynamic range in concentration for the diffusion broadening studies. As in the case of Ge self-diffusion, the samples are thinned to 30-40 µm to avoid the end-of-range defects induced by proton bombardment. Part of the samples, defined by the circular aperture with 3 mm in diameter on the top graphite plate of the sample holder, is exposed to 2.5 MeV protons with current given in Table 5.2. Sample annealing and irradiation conditions are summarized in Table 5.2.
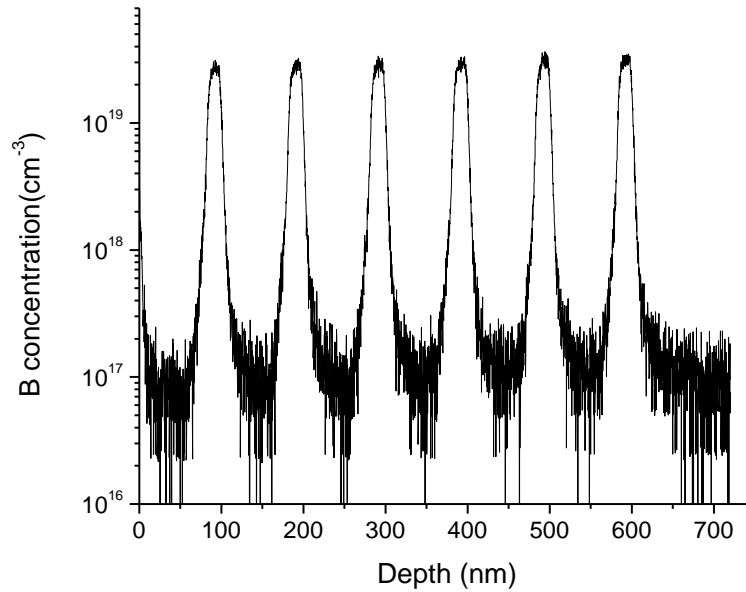
Figure 5.5 Concentration of B as a function of depth for the as-grown B-doped Ge structure.

Table 5.2 The annealing and irradiation conditions for radiation enhanced B diffusion in the Ge study. The last column shows the effective diffusivities under the proton irradiation as determined by profiles fitting with the solutions of the simple Fick's Second Law differential equation.

Temp (°C)	Proton Current (µA)	Anneal Time (hr)	D_{eff} (cm^2/s)
400	1.5	1	8.50×10^{-17}
450	1.5	1	1.25×10^{-16}
500	1.5	1	2.50×10^{-16}
500	1.5	3	3.50×10^{-16}
550	1.5	1	1.30×10^{-16}
748	3.2	1	8.00×10^{-17}

Boron profiles after annealing and proton irradiation are plotted along with the as-grown profile in Figure 5.6. The profiles for the non-irradiated and annealed only part of the samples are not plotted because the B distribution is virtually the same as the as-grown structure. This is an expected result as the equilibrium diffusion length [78] of B in Ge at 748°C for 1 hour anneal is only ~0.8 nm, below the detection resolution of the SIMS. All the profiles in Figure 5.6 were measured with TOF-SIMS at ION-TOF (Münster, Germany) except for the sample annealed and irradiated at 748°C. That sample was measured with quadrupole-mass SIMS at Evans Analytical Group (Sunnyvale, CA); hence the noise level is different from other profiles.
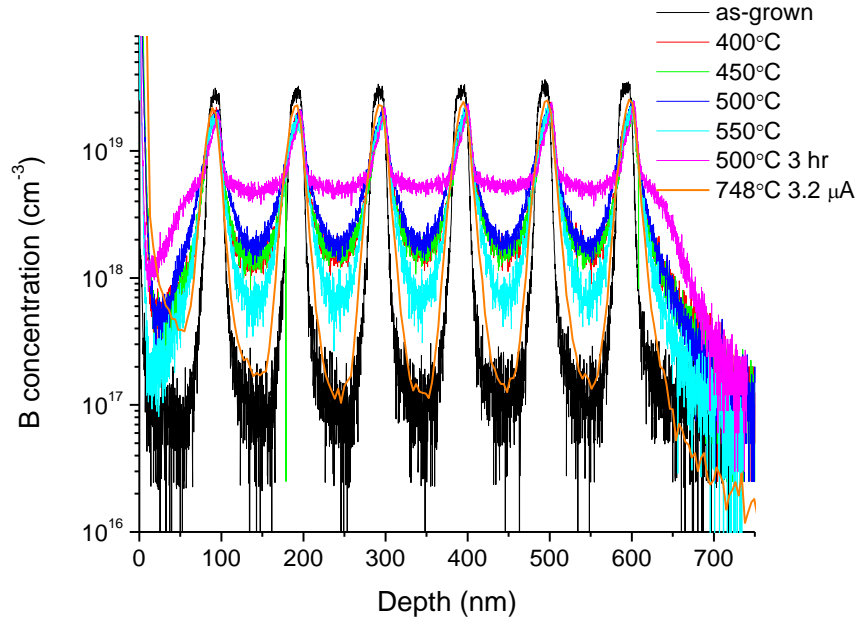
Figure 5.7 Concentration of B as a function of depth as measured by SIMS for the as-grown structure and samples irradiated at a temperature ranging from 400 to 748°C. Except for the one labeled 3 hr, all irradiated samples were annealed for 1 hour. The 748°C sample was irradiated with 3.2 μA of proton current whereas others were irradiated with 1.5 μA.

Clearly, the diffusion broadenings are observed for all samples annealed under proton irradiation. This indicates orders of magnitude enhanced diffusion relative to the equilibrium condition. Boron seems to be immobile above ~ 7×10^{18} cm^{-3}, likely due to clustering. This will be verified in the future structural analysis of the samples. It is important to note that the broadenings are due to diffusion enhancement from irradiation induced point-defects rather than the direct knock-on phenomenon on B atoms from the proton beam. Bruno *et al*. has concluded from their irradiation experiments that proton beam mixing is only possible if the flux is increased by a few orders of magnitude [119]. The effective B diffusion coefficients can be determined by numerically fitting the diffusion profiles assuming no interactions between the native point defects, the diffusing boron, and the Ge lattice atoms. With this assumption, the diffusion profiles are fitted using Mathematica with a simple Fick's Second Law differential equation (Equation 2.2b). For the numerical fitting, only the first B doped layer from the surface is fitted as the diffusion broadenings are homogenous; in other words, the broadenings are virtually the same for all B doped layers regardless of the depth. More details of the fitting are described in Appendix A. The determined effective diffusion coefficients are summarized in Table 5.2. The effective diffusion coefficients are also plotted against inverse temperature in an Arrhenius plot in Figure 5.7.

From Figure 5.7a, it is obvious that the effective diffusion coefficients under proton irradiation are many orders of magnitude higher than the equilibrium diffusivities extrapolated to a lower temperature range from ref. [78]. One trend that can be observed is that as the irradiation temperature increases, the enhancement for the effective B diffusivity over the equilibrium

diffusivity decreases. The effective diffusivity of B at 400°C under a 1.5 µA proton current is 13 orders of magnitude ($10^{13}\times$) higher than the equilibrium value whereas the enhancement factor for the sample irradiated with roughly twice the beam current (3.2 µA) at 748°C is only 36×. This can be explained by the fact that the annihilation rate (k_{IV} from Equation 5.4) of the radiation created interstitials and vacancies are higher at higher temperatures. The annihilation rate increases exponentially as the temperature increases because k_{IV} depends on thermally activated vacancy and interstitial diffusion. As a result, the concentration of the point defects is lower and therefore less effective in enhancing diffusion at higher temperatures. It is also expected based on Equation (5.2) that increasing the proton current will increase the diffusivity enhancement because the defect creation rate k_0 is linearly proportional to the beam current. This will be verified in the future by isothermal experiments with varying proton currents.

a)
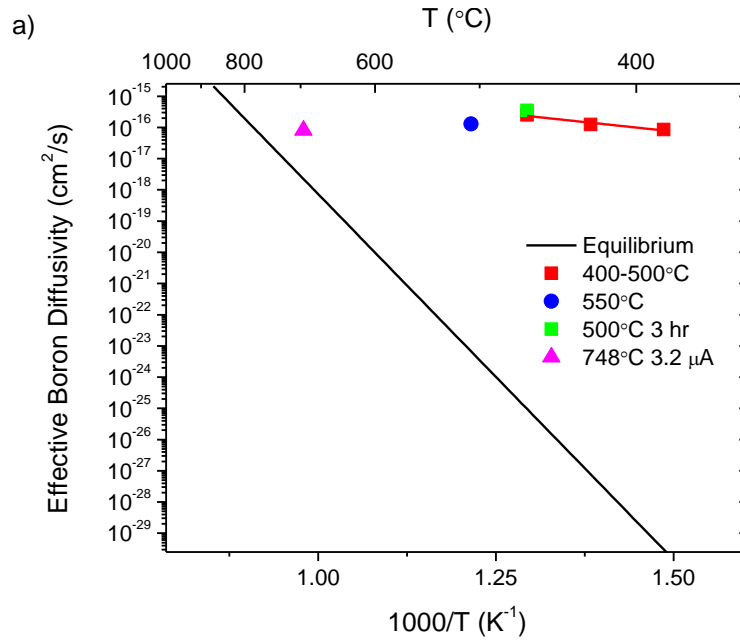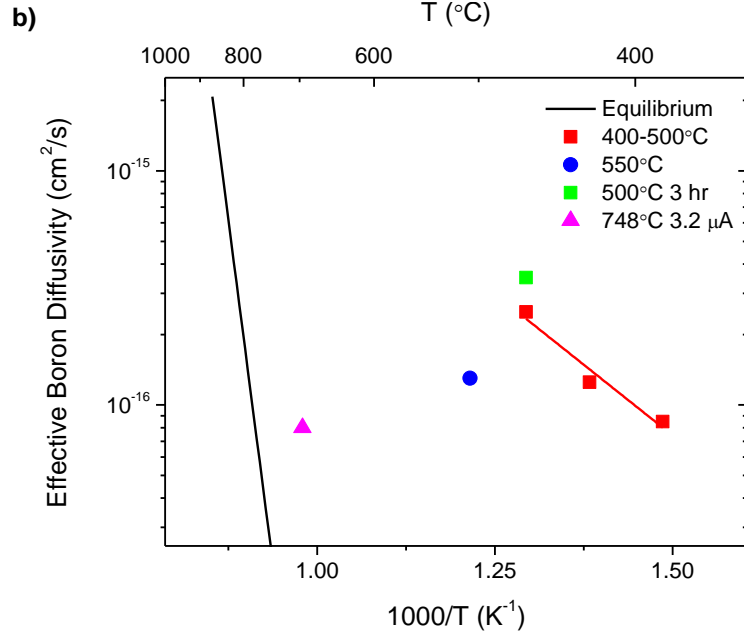
Figure 5.7 The effective boron diffusivity as a function of 1000/T. (a) The effective diffusivities of the samples irradiated at 400-500°C with 1.5 μA proton current for 1 hour are plotted in red squares. The 500°C sample irradiated with the same beam current for 3 hours is plotted in green square. The effective diffusivity determined for the sample irradiated at 550°C with 1.5 μA proton current for 1 hour is shown as blue circle. The effective diffusivity determined for the sample irradiated at 748°C for 1 hour with 3.2 μA proton beam current is shown in magenta triangle. The solid black line indicates the equilibrium diffusivity as extrapolated from the results from ref. [78]. The solid red line is a linear fit through the red squares. (b) shows the same information as (a) with a smaller range on the y-axis.

From Figure 5.7b, one can see the B diffusivities of samples annealed at 400°C, 450°C and 500°C follow a single Arrhenius relationship, suggesting a single dominant diffusion mechanism. The sample irradiated at 500°C for 3 hours has an effective diffusivity slightly higher than the same irradiation condition annealed for 1 hour. This is believed to be due to uncertainties in diffusion profile fitting. The diffusion coefficient as a function of temperature for this temperature range is determined by fitting a straight line through the three data points to be:

$$D_B(T = 400 - 500\degree C) = 3 \times 10^{-13} \exp\left(\frac{-0.48eV}{k_B T}\right) cm^2/s \qquad (5.10)$$

Here, k_B is the Boltzmann constant. The activation enthalpy of 0.48 eV is in sharp contrast to the 4.65 eV for the equilibrium diffusion case obtained by Uppal *et al*. [78]. This activation enthalpy can also be compared with the 0.10 eV obtained by E. Bruno *et al*. in a similar experiment [119]. However, in their experiment, a much lower proton energy (300 keV) is used; therefore complex end-of-range defects may also contribute to the observed diffusion enhancement. This low activation enthalpy for the non-equilibrium condition under proton irradiation suggests the diffusion is mediated by the point defect that has the highest non-equilibrium/equilibrium concentrations ratio, or the supersaturation. From the radiation

enhanced self-diffusion results showing high S_I, it can be concluded that the boron diffusion is mediated by the self-interstitials. As with the case in radiation enhanced self-diffusion, the B profiles are homogenously broadened and independent of the sample depth. Again, this suggests that the surface is not a sink for the point defects. Rather, the surface appears to be reflecting the self-interstitials such that the concentration stays constant even at the near surface region.

From the discussion above, it can be clearly established that boron diffusion is mediated by the self-interstitials. However, to identify the specific interstitial-mediated diffusion mechanism, numerical simulations with proposed differential equations to describe the interactions such as B-I, B-V, B-Ge, and I-V in different charge states are necessary. This task is in progress with our collaborators in Münster. With conditions such as S_I and S_V obtained from the self-diffusion studies and slow equilibrium B diffusion, we are proposing differential equations base on the assumption of the interstitialcy mechanism (see Figure 2.3 and Equation 2.7) to simulate the radiation enhanced B diffusion profiles. While the analysis will likely identify the dominant diffusion mechanism, information such as C_I^{eq} and the charge states of BI pairs are still unverifiable. Ultimately, one has to study the self-diffusion and dopant diffusion simultaneously in the same sample in order to reduce the number of unknown variables and deduce a more accurate explanation and description of the interstitial-mediated diffusion mechanism.

It is interesting to compare the results of the radiation enhanced boron diffusion to those of the impurity diffusion known to be mediated by vacancies only. The phosphorus diffusion, which is known to be vacancy-assisted under the equilibrium condition, under proton irradiation was carried out by our collaborators in Münster. The Ge sample was implanted with P at 30 keV to a dose of 3×10^{15} cm^{-2}. In order to prevent out diffusion at the surface, a 10 nm thick SiO$_2$ was sputter deposited on the Ge sample before the implantation. The sample was then exposed to protons at 570°C for 1 hour under 2.5 MeV and 1.5 µA beam conditions. The P concentration profiles of the as-implanted (dashed line), annealed only (blue squares) and annealed and irradiated (red circles) conditions were measured by SIMS and plotted in Figure 5.8. Preliminary numerical simulations were performed with a reflecting boundary condition for self-interstitials at the surface. The results of the numerical simulation are also plotted in Figure 5.8 as solid black lines.
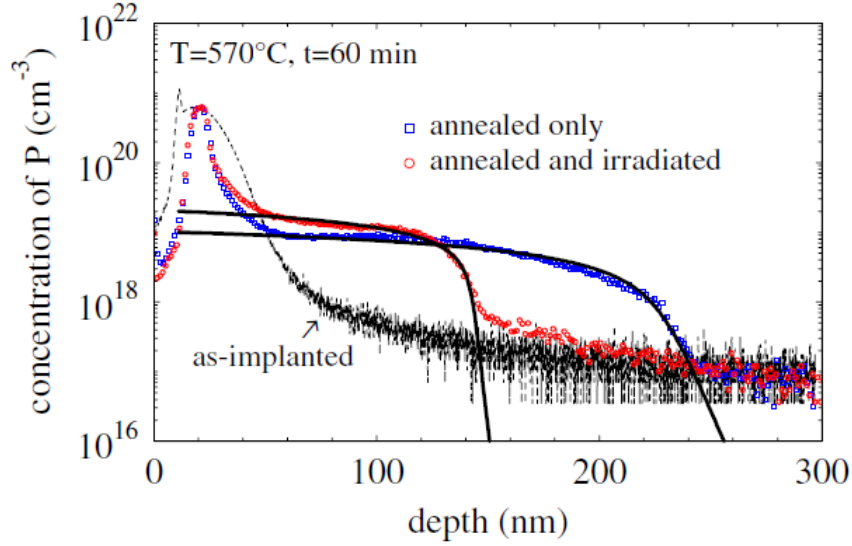
Figure 5.8 P concentration profiles of P implanted Ge measured with SIMS before (dashed line) and after diffusion annealing (symbols). The annealed only (blue squares) profile is obtained from the sample that is covered and therefore not irradiated with protons whereas the annealed and irradiated (red circles) profile is obtained from the part of the sample exposed to the proton beam. The solid black lines are numerical fitting results. The figure is reprinted from ref. [42].

Unlike the radiation effects on self-diffusion and B diffusion, the proton irradiation leads to a reduced diffusivity. The effective diffusivity for this specific experimental condition is calculated to be about 20× less than the equilibrium diffusivity. At first glance, the result seems consistent with excess self-interstitials enhancing self-diffusion and B diffusion under proton irradiation. P diffusion proceeds with the vacancy mechanism with singly negatively charged donor-vacancy (PV)⁻ pairs [100]. With excess self-interstitials created by the proton irradiation, the diffusion of P should be retarded because fewer vacancies are available. However, this explanation may be flawed as the proton bombardment creates vacancies and interstitials in equal numbers. The self-interstitial mediated component of diffusion is dominant under proton irradiation for the cases of self-diffusion and B diffusion only because the proton induced self-interstitial concentration is much higher relative to its equilibrium value. Similarly, under the proton irradiation, the vacancy concentration is expected to exceed that of the equilibrium concentration. Thus, although the effect is small in comparison with interstitial-assisted diffusion, vacancy-mediated diffusion is expected to be enhanced as well. In order to have a retarded diffusion, the vacancy concentration under the proton irradiation has to be lower than that of the equilibrium value ($S_V<1$), which is counter-intuitive and seems unlikely. Therefore, the fact that P diffusion is retarded under proton irradiation suggests that the surface may be a strongly reflecting boundary for the self-interstitials. This way, the vacancies near the surface are annihilated by the reflected self-interstitials resulting in local vacancy concentration lower than that of the equilibrium concentration. One other possible explanation for the retarded P diffusion is that, despite the presence of the SiO_2 capping layer, P is still leaving the surface, creating an artificial sink for P diffusion. Our collaborators in Münster are currently examining the possibility of P being depleted near the surface and exploring different capping layers in preventing P depletion.

In conclusion, the diffusion studies performed under proton irradiation clearly demonstrate that self-interstitial mediated diffusion is favored under this highly non-equilibrium condition. The radiation enhanced self-diffusion experiments establish the frame work in analyzing B and P diffusion experiments. The enhanced B diffusion under proton irradiation confirms that interstitial-mediated diffusion mechanism is dominant for this small acceptor in Ge. Although the true cause for the retarded P diffusion under proton irradiation is still under investigation, the effect is real and reproducible. This may provide a solution for the fabrication of shallow junctions in n-channel Ge-based MOSFETs by defect engineering to reduce undesirable donor diffusion. Finally, to fully identify the interstitial-mediated diffusion mechanism for B diffusion in Ge, numerical simulation is needed. However, for an accurate numerical simulation, the surface boundary conditions must be well understood. We are in the process of performing additional experiments that may provide a better understanding of the surface and its effect on the excess point defects induced by the proton beam.

Chapter 6 Future Work

From the discussions in chapters 4 and 5, it is clear that more experiments must be done in order to understand diffusion in SiGe alloys and in Ge fully. Section 6.1 focuses on the future work in identifying the transition in the diffusion mechanism of As in SiGe alloys. This is followed by the discussion of future planned experiments in exploring the role of self-interstitials for diffusion in Ge by radiation enhanced diffusion in Section 6.2.

6.1   Future work in As diffusion in $Si_{1-x}Ge_x$

To identify the dominant diffusion mechanism of As in SiGe alloys transitioning from the roughly equal contributions from vacancy- and interstitial-mediated diffusion in Si to the vacancy-mediated diffusion in Ge, samples with other SiGe compositions are required. By continuing finding the As diffusion activation enthalpy as a function of Ge content in the alloy, in other words, by filling more data points in Figure 4.9, one can observe the switch of the dominant diffusion mechanism by looking at the change of the activation enthalpies as a function of Ge content. In fact, it has been predicted theoretically that the binding energy between a vacancy and As in forming the AsV pair does not depend linearly on the Ge content in the SiGe alloys [121]. Based on the theoretical prediction, one would expect bowing to be observed in the activation enthalpy vs. Ge content plot as well because the diffusion activation is intimately linked with the formation energy of AsV pair.

The main difficulty in the experiment is to obtain high quality MBE-grown isotopically enriched multilayer structures similar to the one depicted in Figure 3.2 with varying Ge content. Due to carbon contamination in our collaborators' MBE chamber at the University of Aarhus in Denmark, the growth of the isotopically enriched structures with higher Ge contents have been delayed indefinitely. The requirement for highly isotopically enriched Si and Ge sources makes their system unique in growing the desired structure for further experiments. The study will proceed when the SiGe alloy samples with higher Ge content become available.

6.2   Future work in radiation enhanced diffusion in Ge

To reiterate, one of the main goals for this work is to identify and understand the self-interstitials in Ge and their role in diffusion. By knowing the fundamental properties of self-interstitials during diffusion, defect engineering to reduce donor diffusion and increase donor electrical activation can be exploited. As mentioned in Chapters 3 and 5, the study of the diffusion of the impurities believed to be assisted by self-interstitials alone under the non-equilibrium condition of constant proton bombardment is important in determining the fundamental properties of the self-interstitials. To perform further experiments more conveniently, we have constructed a vacuum heater with a design similar to the system in Münster to be attached to a tandem accelerator at Lawrence Berkeley National Laboratory (LBNL). The accelerator has a base accelerating voltage of 1.7 MeV. The proton can be accelerated twice, in the first stage as H^-, then the two electrons are stripped away by a thin graphite layer and H^+ is accelerated again at the second stage, bringing the total proton energy to

3.4 MeV. The vacuum heater has the same general design as the one in Münster which is schematically shown in Figure 3.4. The heater assembly is built on a 6-inch ConFlat flange with feedthroughs for the thermocouple, power supply, current measurements and high voltage secondary electron suppression. The heating element is a one-inch resistive heater with ceramic coatings from Heat Wave Labs (Watsonville, CA) capable of reaching 1200°C. The sample holder has a base of a 5 mm thick graphite piece with a 1 mm thick covering plate. At the center of the top plate, a 3 mm hole is drilled for the protons to go through. The thermocouple is placed in the thick graphite piece about 1 mm below the sample surface. To measure the incident proton current, a tantalum wire is attached to the graphite block. Pictures of the heater assembly are attached in Figure 6.1. The accelerator is capable in generating about 1 μA of current with a beam diameter of ~10 mm. Although the total beam current is low relative to the accelerator in Bochum Germany, the beam can be focused to achieve a higher flux density. Future proposed experiments will be performed on the heater assembly using the LBNL accelerator.
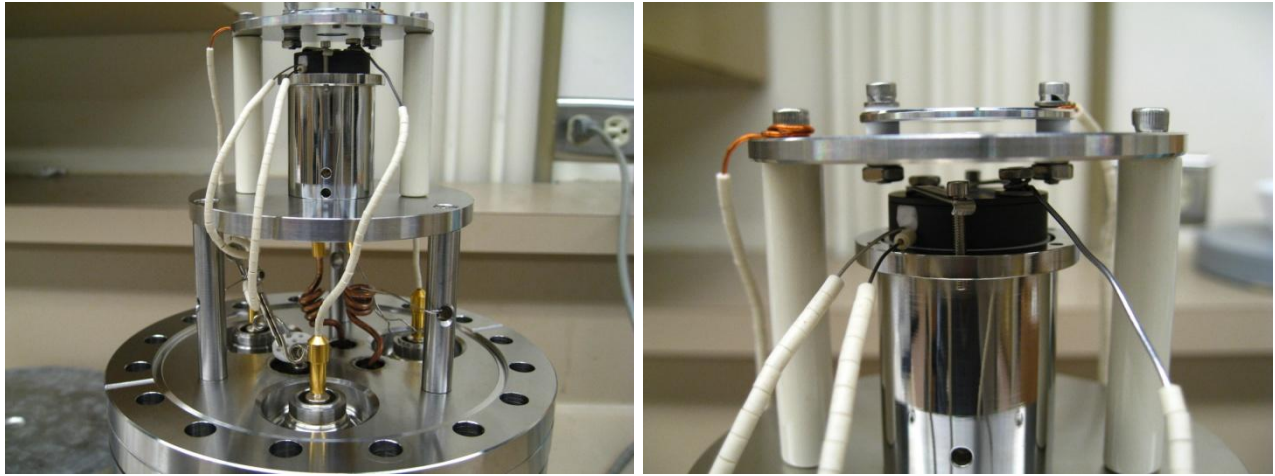
Figure 6.1 Pictures showing the vacuum heater built at LBNL to be attached to a tandem proton accelerator.

Besides boron, carbon is another impurity candidate that is believed to diffuse via the interstitialcy mechanism. Following the correlation between the size of the impurity and its diffusion activation enthalpy, as summarized in Table 5.1, carbon, the smallest isovalent group IV impurity, is expected to diffuse very slowly. The expected high diffusion enthalpy is a good indicator that C diffusion may be interstitial-driven. In fact, previous experiments have shown C to be immobile even at 750°C under equilibrium conditions [100]. Therefore, we propose to study C diffusion in Ge under the non-equilibrium condition of excess self-interstitials created by continuous proton bombardment.

Some preliminary experiments have been performed to study proton radiation enhanced C diffusion in Ge. C was implanted into an ultra pure Ge wafer at 30 keV with a dose of 1×10^{15} cm^{-2}. This light implant is not expected to produce extensive damage to the Ge lattice and introduces point-defect sources affecting diffusion. Similar to the self-diffusion, B diffusion, and P diffusion studies, the C implanted sample was annealed at 570°C and 700°C under 2.5 MeV proton beam with 1.5 μA beam current. Figure 6.2 shows the C concentration profiles for the as-implanted, 570°C irradiated and annealed, 700°C irradiated and annealed, and 700°C annealed

only samples. It is clear from the figure that no observable diffusion occurred for any of the experimental conditions. The result is surprising as orders of magnitude enhancement is expected for the self-interstitial concentration at 570°C under the proton bombardment. Carbon diffusion appears to be even slower than that of B even under the conditions with excess point defects. One possible explanation is that the solubility of C in Ge is so low that immobile clusters are formed. In fact, the C-Ge phase diagram shows C does not become soluble in Ge until temperature reaches 2834°C, well above the Ge melting temperature [122]. Further structural characterization will be performed to clarify this. In addition, experiments with other temperatures will also be carried out to expand the temperature range of the experiments.
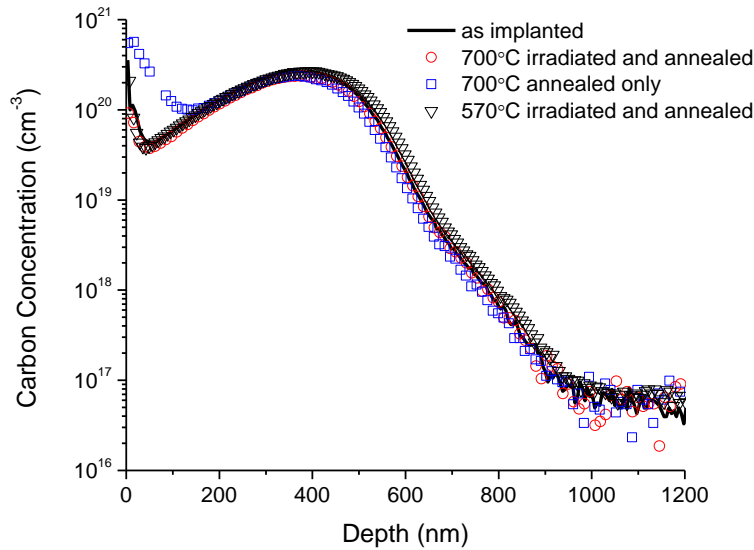
Figure 6.2 Concentration profiles of carbon as measured by SIMS for sample annealed at 570°C and 700°C.

Next, to further pinpoint the dominant diffusion mechanism for B in Ge and the charge states of the impurity-defect pair, the use of a structure with the combination of Ge isotopically enriched layers and B doped layers is proposed. By studying B and Ge self-diffusion simultaneously under proton irradiation, the assumption presented in Equation (5.9) may be eliminated and the determination of supersaturations, S_I and S_V, may be possible from the numerical simulations. Further, by observing both diffusion broadenings as a function of depth, the surface boundary condition for the point defects may be clarified.

Another experiment to study the boundary behavior at the surface is also proposed. A MBE grown structure with impurity doped layers in Ge such as the one (shown in Figure 5.5) used for B diffusion study will be used. The sample can then be implanted by high energy Ge self-atoms to amorphize the top layer and introduce extensive end-of-range defects near the center of the doping modulation structure. It has been found that while the amorphized layer recrystalizes at a relatively mild temperature via the solid phase epitaxy, the end-of-range defects cannot be easily annealed out leaving a source for interstitials [123]. This sample can then be subjected to diffusion anneals with an interstitial source in the middle of the structure. Depending on the nature of the surface, the diffusion broadenings are expected to be different for

the impurity doped layers before and after the end-of-range interstitial source. The sample can be modeled as having an interstitial source sandwiched between a semi-infinite layer and a finite layer with the surface close by. By observing any asymmetry in the diffusion broadenings for impurities before and after this interstitial source, the surface boundary condition for the interstitials may be identified. The difficulty in this experiment is to implant high energy Ge at a high dose. Based on a simulation from SRIM, an implantation energy of 1 MeV is required to have a range of 500 nm necessary for our current B doped Ge structure.

Finally, we propose to extend the study of P and other donor diffusion under proton irradiation. Ideally, a MBE grown structure with donor doped layers similar to the one with B doped layers will be used. This way, not only the enhanced or retarded diffusion as a function of depth can be observed more clearly, the possible surface degradation can be eliminated by capping the donor doped layers with a thick layer of undoped Ge. If the excess self-interstitials created by the proton irradiation do indeed hinder donor diffusion by eliminating vacancies in the system, then defect engineering may be used to form n-type ultra shallow junctions in Ge based devices. Further, the electrical activation may also be improved since the deactivation process is believed to be donors leaving the substitutional sites forming the electrical inactive donor-vacancy $(D_2V)^0$ pairs at high concentrations [100]. By eliminating vacancies in the system by introducing excess self-interstitials, shallow n-type junction with high electrical activation may be achieved in Ge.

Chapter 7 Summary and Conclusion

In summary, although Ge is the semiconductor material used in discovering the first transistor, it has been absent from commercial transistors for the past 40-50 years. However, as the scaling on Si based transistor devices are reaching their limits in performance improvement, Ge is re-introduced into devices. Ge was first re-introduced into the source and drain of the modern MOSFETs, forming SiGe alloys to uniaxially strain the Si channel to enhance carrier mobilities. In addition, it has been proposed to replace Si altogether with Ge as the channel material to take full advantage of its higher carrier mobilities. Regardless of the application, it is clear that understanding diffusion in Ge and SiGe alloys is crucial technologically in advancing device performance. Further, the study of diffusion is also important scientifically. Although indirect, studying diffusion is arguably the best way to study native point defects and their interactions with the lattice atoms and the impurities at elevated temperatures. Thus, the studies of diffusion, the most fundamental matter transport process, in SiGe alloys and Ge are important in understanding point defects in these materials.

Experiments were carried out to study As, one of the most common n-type dopants used in devices, diffusion in SiGe alloys by utilizing isotope engineering. As diffusion experiments in $Si_{0.95}Ge_{0.05}$ were performed using a MBE grown isotopically enriched structure in order to study As and Si and Ge self-diffusions simultaneously. The results show that the diffusion mechanism is very similar to the case of As in pure Si. The only difference is the introduction of $(As_2V)^0$ defect pairs typically found in the diffusion in pure Ge in the numerical simulations to describe the experimentally measured results accurately. The diffusion activation enthalpy is determined to be 4.27 eV within the range expected for this alloy composition. To see the transition of predominant As diffusion mechanism from interstitial and vacancy assisted to vacancy assisted only from pure Si to pure Ge, SiGe alloy samples with different Ge content are required. Pending on the availability of the specialized MBE grown isotopically enriched SiGe layers, the experiments will be performed in the future.

The study of diffusion in Ge is focused on the role of self-interstitials for diffusion. Different from the diffusion in Si, where both the vacancy and the interstitial play important roles, diffusion in Ge is dominated by vacancy-mediated diffusion. This is suspected to be caused by the low equilibrium concentration of self-interstitials. In order to study the effect of self-interstitials on the diffusion in Ge, excess interstitials with concentration well above the equilibrium value are introduced by proton irradiation. The diffusion anneal experiments were carried out under a constant proton irradiation to study Ge self-diffusion, B diffusion, and P diffusion.

The results from the radiation enhanced self-diffusion clearly demonstrate that there is an interstitial-mediated component in Ge self-diffusion. The self-diffusion is observed to be much enhanced under proton irradiation. This confirms that, as in the case of Si self-diffusion, Ge self-diffusion has contributions from both vacancy assistance and interstitial assistance. However, due to the low equilibrium interstitial concentration, the vacancy-mediated diffusion is dominant at equilibrium. Further, the radiation enhanced self-diffusion results suggest that the surface, the Ge/air interface, is not a strong sink for the point defects, at variance with the case in Si. To

ensure accurate numerical simulation and to identify the interstitial-assisted mechanisms, the surface condition must be identified. We propose an experiment to introduce an interstitial source in the middle of the Ge layer of interest in order to further identify the surface condition.

B diffusion in Ge appears to be a special case. B diffusivity is lowest among common impurities in Ge. The B diffusivity is lower than the self-diffusivity by a few orders of magnitude. This low diffusivity and the high diffusion activation enthalpy suggest that B diffusion may be interstitial-mediated. This is confirmed by the radiation enhanced diffusion experiments. The experimental results show that the effective B diffusivity is several orders of magnitude higher than the equilibrium diffusivity at temperatures ranging from 400-550°C. We also found that the radiation enhancement decreases as temperature increases. This is consistent with the fact that the radiation created interstitials and vacancies annihilation rate is higher at high temperature. This annihilation rate increases exponentially as temperature increases, resulting in lower self-interstitial concentration to assist B diffusion. The B diffusion results, again, show diffusion independent of the sample depth, suggesting the surface is not a sink for the excess self-interstitials. In order to identify the exact diffusion mechanism and the charge states of the B-defect pairs, a structure containing isotopically enriched Ge layers as well as B doped layers to study both diffusions simultaneously is proposed for future experiments.

Finally, the results of the radiation effects on P diffusion are elucidated. Unlike the results from the self-diffusion and B diffusion under proton irradiation, P diffusion is found to be retarded by 20× at 570°C under proton irradiation. This retardation is unexpected as the proton irradiation creates excess vacancies as well. Therefore, one should expect to observe a slight diffusion enhancement for P diffusion, which is mediated mainly by vacancies. One possible explanation for the retarded P diffusion is the high supersaturation of interstitials near the surface due to a reflecting boundary condition. Again, this generates a need to understand the surface boundary condition. The exact surface condition is still under investigation. Nevertheless, the slowed P diffusion provides a possibility for reducing donor diffusion in forming shallow junctions in n-type Ge MOSFETs.

In conclusion, the diffusion studies are important both technologically and scientifically. As diffusion processes are dominated by impurity-defect interactions, the understanding of point defects behavior is crucial in predicting diffusion behaviors. This work presents different methods in identifying the diffusion mechanisms and studying defect-impurity interactions in SiGe alloys and in Ge. This work successfully demonstrates that self-interstitials does play an important role in Ge diffusion. Most noticeably, for B diffusion in Ge, interstitial-assisted diffusion is found to be the predominant mechanism. While the identification of the detailed diffusion mechanisms and the surface condition require additional experiments, our work has provided a basis and direction for future experiments.

Appendix A Diffusion Fittings

This appendix includes some of the numerical diffusion fitting results. For the first part, numerical diffusion fitting results performed on the As in $Si_{0.95}Ge_{0.05}$ diffusion profiles are presented. The second part shows the numerical diffusion fittings performed on B diffusion in Ge under proton irradiation.

A.1 Numerical fittings on As diffusion in $Si_{0.95}Ge_{0.05}$

The numerical fitting of the profiles of the simultaneous As, Si, and Ge diffusion in $Si_{0.95}Ge_{0.05}$ were performed by Professor Hartmut Bracht of the University of Münster in Germany. The reactions he considered are presented in Equations (4.9a)-(4.11) and reproduced below:

$$(AsV)^0 \Leftrightarrow As_s^+ + V^- \qquad (4.9a)$$

$$(AsV)^- \Leftrightarrow As_s^+ + V^{--} \qquad (4.9b)$$

$$(AsI)^0 \Leftrightarrow As_s^+ + I^0 + e^- \qquad (4.10)$$

$$(As_2V)^0 \Leftrightarrow 2As_s^+ + V^{--} \qquad (4.11)$$

Here, the interstitials, I, can be either Si or Ge self-atoms. Besides these reactions, Ge is also allowed to leave the surface to simulate the surface depletion observed in many samples. The diffusion profiles with numerical fittings for samples appear to diffuse in intrinsic conditions are shown in Figure A.1 below. Figure A.2 shows the diffusion profiles with numerical fittings for samples in extrinsic diffusion conditions.
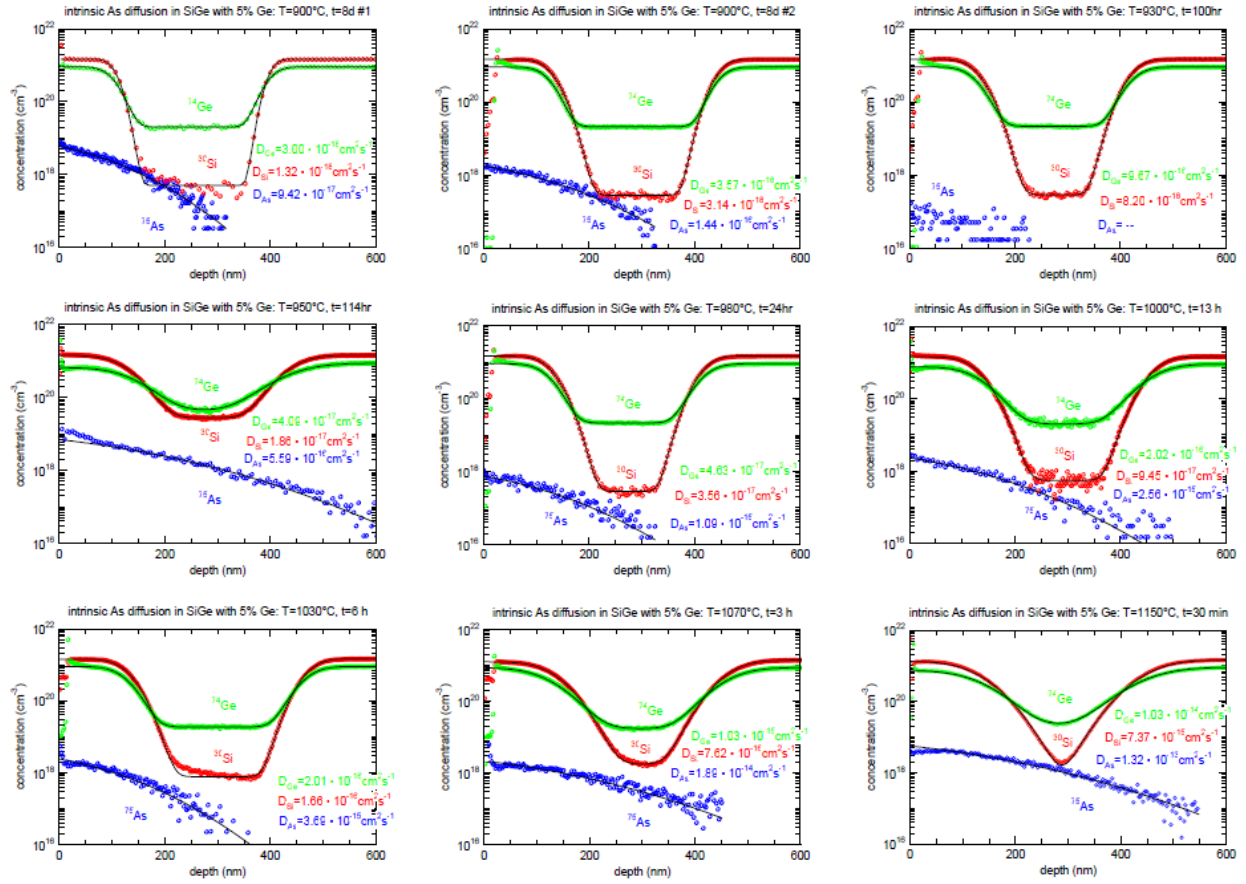
Figure A.1 Experimentally measured diffusion profiles for ^{30}Si (red), ^{74}Ge (green), and ^{75}As (blue) under intrinsic diffusion conditions along with numerical fitting results (solid black lines) for As diffusion in Si$_{0.95}$Ge$_{0.05}$.
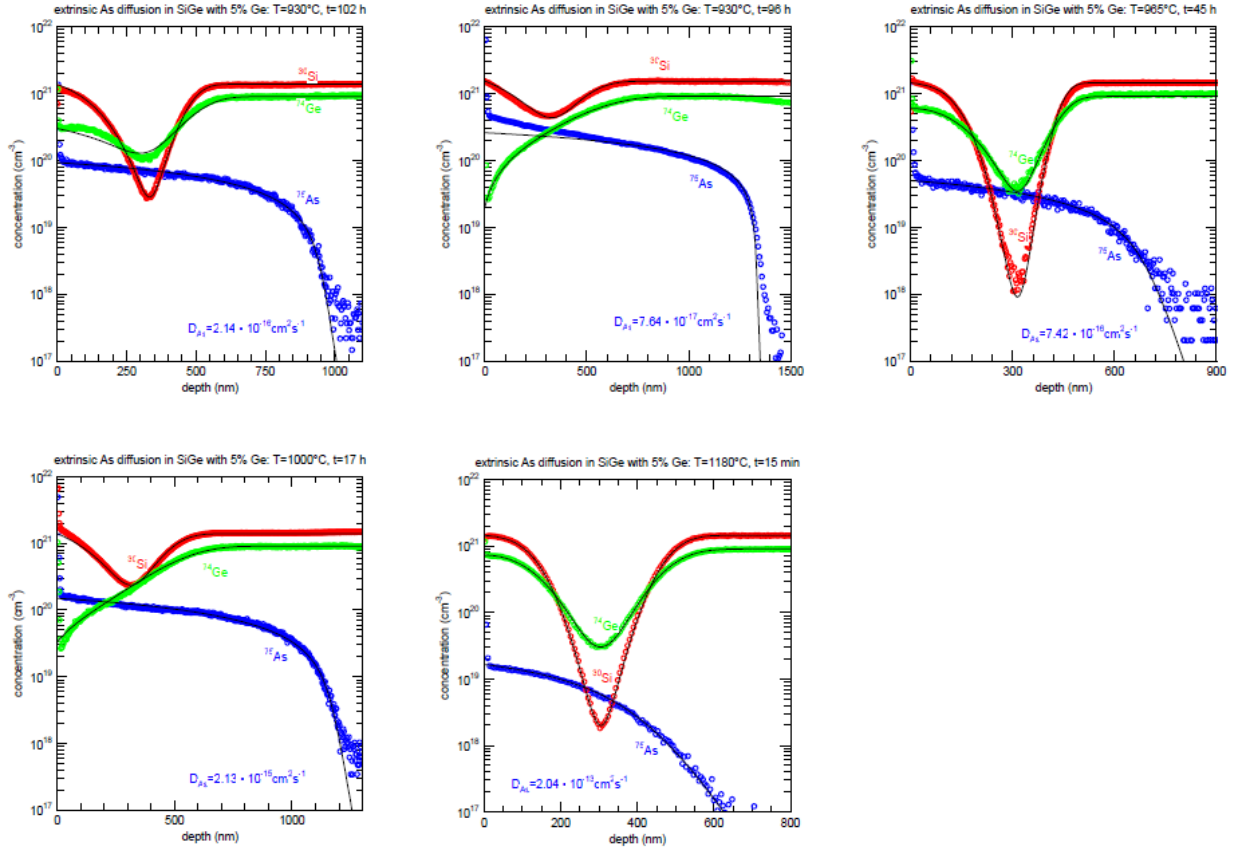
Figure A.2 Experimentally measured diffusion profiles for ^{30}Si (red), ^{74}Ge (green), and ^{75}As (blue) under extrinsic diffusion conditions along with numerical fitting results (solid black lines) for As diffusion in Si$_{0.95}$Ge$_{0.05}$.

The As diffusion coefficient as a function of temperature can then be obtained. The results are plotted in Figure 4.8 while the Arrhenius relationship is presented in Equation (4.12).

A.2 Numerical fittings on radiation enhanced B diffusion in Ge

The numerical fittings for the B profiles in the radiation enhanced diffusion studies in Ge were performed by Cosima Boswell of the Computational Materials Science group at the Department of Materials Science and Engineering at UC Berkeley. As mentioned in Chapter 5, only the first of the six B-doped peaks was fitted because the diffusion broadening is homogeneous throughout the sample thickness. The fitting was performed using Mathematica by first modeling the profile of the first B-doped peak in the as-grown structure as a sum of two error functions. The choice of the error functions fitting is arbitrary to optimize the speed of the fitting and does not represent any physical meaning. The as-grown profiles were then allowed to diffuse numerically by following the Fick's Second Law differential equation in one-dimension (Equation A.1) with D_B as the fitting parameter until least-square best fits were obtained.

$$\frac{\partial C_B}{\partial t} = D_B \frac{\partial^2 C_B}{\partial x^2} \qquad\qquad (A.1)$$

The experimentally measured B profiles of the first peak in the samples annealed and irradiated at different temperatures were normalized to 100 nm and results were fitted numerically. The fitting results along with the measured profiles for samples annealed at different temperatures are presented in the figures below.

a)

b)

c)

d)
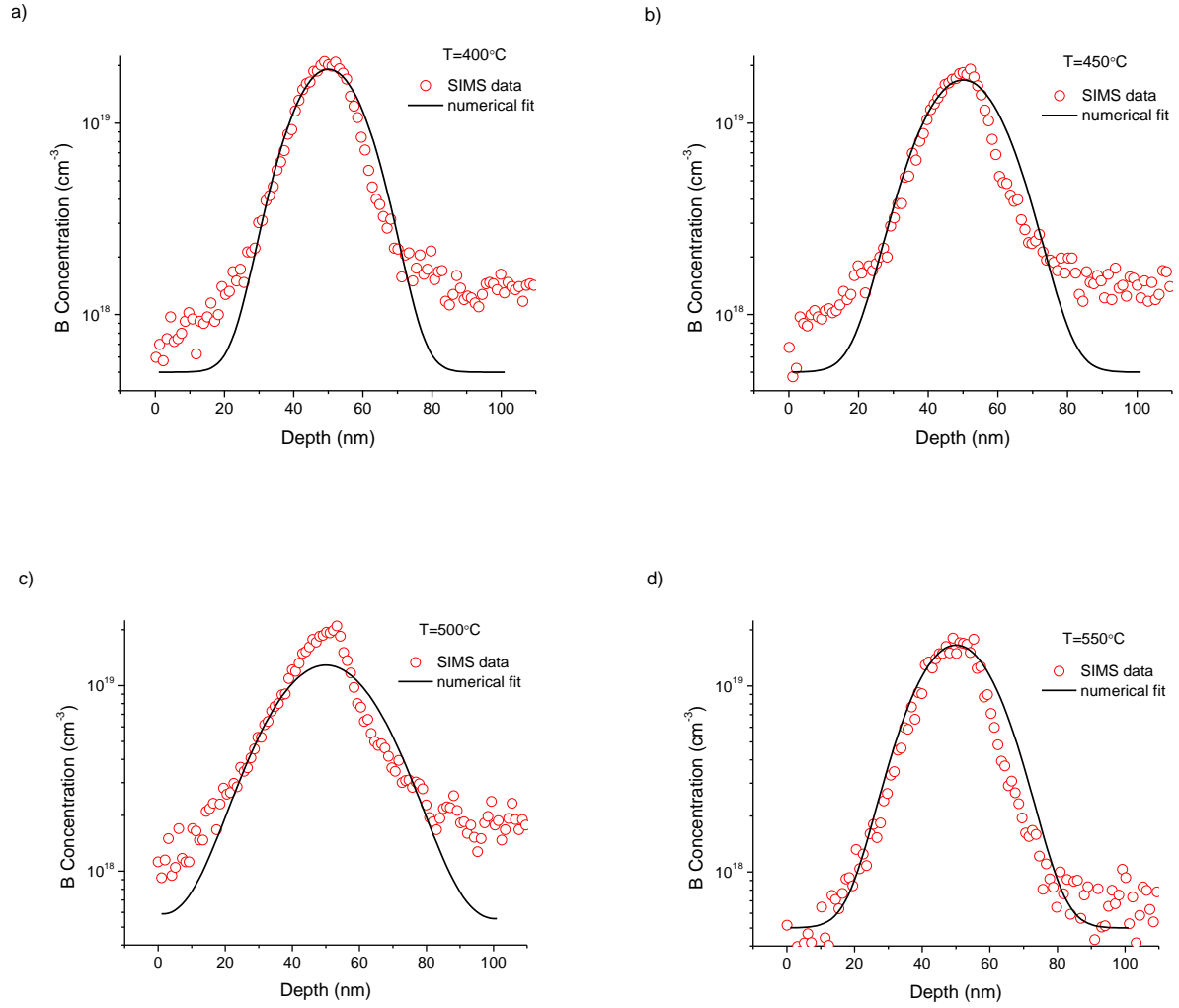
e)
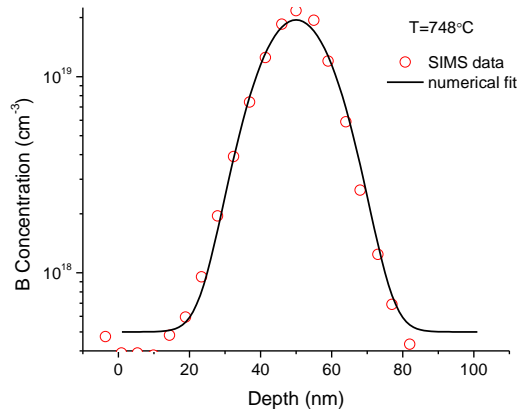
Figure A.3 Numerical fitting of the first B doping peak in Ge for sample annealed and irradiated at (a) 400°C, (b) 450°C, (c) 500°C, (d) 550°C, and (e) 748°C.

The effective B diffusivity as a function of inverse temperature is then plotted in Figure 5.7. The entirety of the Mathematica notebook is reproduced below.

```
numx = 101;
numt = 50 000;
dx = 1 / (numx - 1);
dt = 0.1; (* given in seconds *)

dt * numt (* Total simulation time given in seconds *)

5000.

3600 (* 1 hr experimental time given in seconds *) / dt

36 000.

f[i_] := (i - 1) * dx

x = Array[f, numx];

Conc = ConstantArray[0, {numx, numt}];

t[1] := 0;
a = 2.7 * 10^19;
b = 5 * 10^17;
```

Thetafunction approximation of as - grown distribution

```
For[i = 1, i ≤ numx, i++,
  If[i ≤ 42, Conc[[i, 1]] = b, If[i ≤ 58, Conc[[i, 1]] = a, Conc[[i, 1]] = b]]]
```

Errorfunction approximation of as - grown distribution

```
For[i = 1, i ≤ numx, i++, If[i ≤ 50, Conc[[i, 1]] = (a - b) * (Erf[(i - 41.5) * 3 / 10] + 1) / 2 + b,
  Conc[[i, 1]] = (a - b) * (-Erf[(i - 58.5) * 3 / 10] + 1) / 2 + b]]

Clear[i]

TimeInit = Table[{k, Conc[[k, 1]]}, {k, 1, 101}];
TimeInitPlot = ListPlot[TimeInit, PlotRange → All]
```
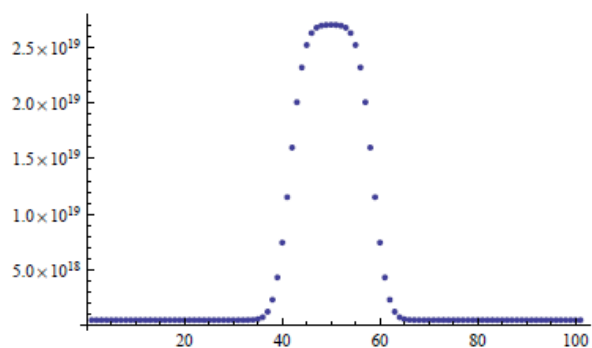
```
D0 = 0.0000008

8. × 10^-7

For[j = 1, j ≤ numt - 1, j++,
 (t[j_ + 1] := t[j] + dt;
  For [i = 2, i ≤ numx - 1, i++,
   (Conc[[i, j + 1]] =
      Conc[[i, j]] + D0 * (dt / dx^2) * (Conc[[i + 1, j]] - 2 * Conc[[i, j]] + Conc[[i - 1, j]]))];
  Conc[[1, j + 1]] = Conc[[2, j + 1]];
  Conc[[numx, j + 1]] = Conc[[numx - 1, j + 1]]
 )]

Time[l_] := Table[{k, Conc[[k, l]]}, {k, 1, 101}];
TimePlot[l_] := ListPlot[Time[l], PlotRange → All]

DataAsGrown = Import["/Users/CosimaBoswell/Desktop/Boron in Ge/as-grown", "Table"];

AsGrown =
  Table[{1.01 * DataAsGrown[[i, 1]] - 43, DataAsGrown[[i, 2]]}, {i, 1, Length[DataAsGrown]}];

PlotAsGrown = ListPlot[{AsGrown}, Joined → True,
   BaseStyle → {FontFamily → "Helvetica", FontSize → 16}, AxesLabel → {"Depth (nm)", "B conc
[nm^-3]"}, PlotRange → {{0, 100}, {10^15, 3 * 10^19}}, AxesOrigin → {0, 10^15}, PlotStyle → Red];

Data1 = Import["/Users/CosimaBoswell/Desktop/Boron in Ge/400C-60min-1500nA", "Table"];
Data2 = Import["/Users/CosimaBoswell/Desktop/Boron in Ge/450C-60min-1500nA", "Table"];
Data3 = Import["/Users/CosimaBoswell/Desktop/Boron in Ge/500C-60min-1500nA", "Table"];
Data4 = Import["/Users/CosimaBoswell/Desktop/Boron in Ge/500C-180min-1500nA", "Table"];
Data5 = Import["/Users/CosimaBoswell/Desktop/Boron in Ge/550C-60min-1500nA", "Table"];
Data6 = Import["/Users/CosimaBoswell/Desktop/Boron in Ge/748C-60min-3200nA", "Table"];


Profile[1] = Table[{Data1[[i, 1]] - 42, Data1[[i, 2]]}, {i, 1, Length[Data1]}];
Profile[2] = Table[{Data2[[i, 1]] - 43, Data2[[i, 2]]}, {i, 1, Length[Data2]}];
Profile[3] = Table[{0.96 * Data3[[i, 1]] - 43, Data3[[i, 2]]}, {i, 1, Length[Data3]}];
Profile[4] = Table[{0.97 * Data4[[i, 1]] - 43, Data4[[i, 2]]}, {i, 1, Length[Data4]}];
Profile[5] = Table[{Data5[[i, 1]] - 41, Data5[[i, 2]]}, {i, 1, Length[Data5]}];
Profile[6] = Table[{Data6[[i, 1]] - 55, Data6[[i, 2]]}, {i, 2, Length[Data6]}];


For[i = 1, i ≤ 6, i++, PlotData[i] = ListPlot[{Profile[i]}, Joined → True,
   BaseStyle → {FontFamily → "Helvetica", FontSize → 16}, AxesLabel → {"Depth (nm)", "B conc
[nm^-3]"}, PlotRange → {{100, 200}, {10^15, 3 * 10^19}}, AxesOrigin → {100, 10^15}]]
```
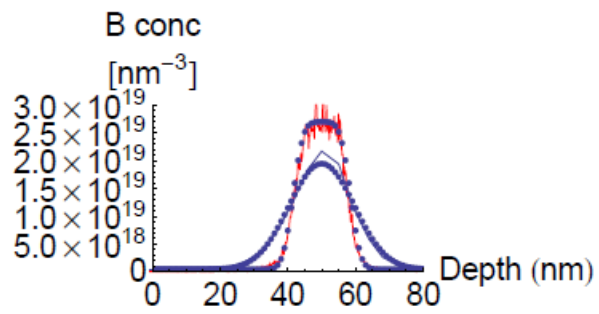
```
Show[{PlotAsGrown, TimePlot[1], TimePlot[36000], PlotData[6]},
 PlotRange → {{0, 80}, {10^15, 3 * 10^19}}]
```

B conc
$[nm^{-3}]$



```
Export["748C60min.xls", Time[36000]]

748C60min.xls
```

Appendix B Secondary Ion Mass Spectrometry

Secondary Ion Mass Spectrometry (SIMS) is used as the primary characterization technique in determining the diffusion profiles of different species in the samples. Compared to traditional methods of p-n junction or sheet-resistance measurements in combination with mechanical sectioning and radiotracer technique, SIMS offers a vast improvement in accurate depth profiling for impurities and self-atoms in semiconductor samples. This appendix aims to provide a brief overview of the SIMS technique with emphasis on the different mass spectrometry methods. Most of the details of this appendix are taken from references [124] and [125] by Vickerman *et al*. Some discussions are from ref. [126]. More detailed physical descriptions of the technique can be found in those references.

B.1 Introduction

SIMS is a technique that mass analyzes ionized particles which are emitted when the surface of a sample is bombarded by energetic primary ions. A primary ion impinges on the sample surface and secondary electrons, neutral species, ions, cluster ions, and molecules are ejected by this sputtering process. While most of the secondary species are neutral and cannot be detected by a mass analyzer, a small fraction (~1%) ejects as charged ions and can be mass separated and detected by the mass spectrometer. Figure B.1 below shows a schematic of the SIMS process where a primary ion loses energy and sputters off secondary species. There are two main types of SIMS operation mode, dynamic SIMS and static SIMS. In the dynamic SIMS mode, a higher energy and intensity primary ion beam is used (5-20 keV with beam current in µA range) to have a higher sputtering rate (> 1 monolayer per second) and the secondary ions are recorded as a function of the sputtering time. This way, the depth profile can be obtained by detecting the secondary ions while sputter-etching the sample if the sputtering rate is known. On the other hand, in the static SIMS mode, low energy and current primary ion beam (0.5-5 keV with ~nA beam current range) is used allowing for very sensitive surface analysis.
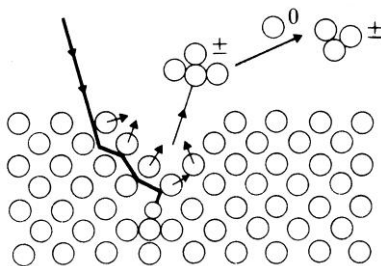
Figure B.1 A schematic of SIMS process showing the primary ion impacting on the sample resulting in the emission of secondary surface ions, charged clusters, and neutral particles. (from ref. [124]).

Without doubt, quantitative depth profiling using dynamic SIMS is the major strength of the technique for characterization of semiconductor materials. Under typical operating conditions in detecting impurities in Si, detection limits in the 10^{14} to 10^{15} cm^{-3} range can be achieved with depth resolution of about 1 nm. The accurate quantitative analysis of the secondary ion signals, however, requires careful calibration of the sputtering rate. This is often

done with standard samples with the same or similar matrix material with ion implanted impurities. When such a standard with known ion implanted impurity profile is measured, the sputter rate can be calibrated for the system to ensure accurate measurements for the unknown impurity profiles.

Fundamentally, a SIMS system consists of a primary ion source to sputter the sample and a mass spectrometer to analyze the emitted secondary ions. There are three types of mass analyzers generally used in modern SIMS systems: quadrupole, magnetic sector, and time-of-flight mass analyzers. While the quadrupole and magnetic sector mass analyzers dominated the field for years, the emergence of the time-of-flight (TOF) mass spectrometer recently has proven to be a useful addition in analysis of a wide range of materials, including organics and inorganics, in many different fields. Since all three types are used in our experiments (quadrupole mass spectrometry and magnetic sector mass spectrometry from Evans Analytical Group in Sunnyvale, CA and East Windsor, NJ and TOF SIMS from Ion-TOF in Münster, Germany), their differences are discussed briefly below. The discussion of the different mass spectrometry techniques are preceded by the discussion of the primary ions.

B.2   Primary ions

The primary particles used to generate the secondary ion yields from the sample may be electrons, ions, neutral atoms, or photons, however, Ar^+, Ga^+ or alkali metal ions are historically used because they are easily available. The sputter yield, the average number of atoms sputtered per incident primary ion, depends on the sample material, its crystallographic orientation, and the nature, energy, and incident angle of the primary ions. The sputter yield can be enhanced by orders of magnitude if a reactive ion is used instead of the traditional ions mentioned above. In particular for semiconductor characterization, electronegative O^- or O_2^+ are often used in enhancing the sputter yield of electropositive elements (e.g., B and Al in Si) while electropositive Cs^+ is used to enhance the sputter yield of electronegative elements (e.g., P, As, and Sb in Si). More recently, clustered ion sources such as C_{60} are used in TOF-SIMS in static mode to detect the surface of complex organic molecules [127]. These exotic primary sources are typically not used in the depth profiling in semiconductor materials.

B.3   Mass analyzers

The secondary ions sputtered off by the primary ions are collected by the mass spectrometer, which consists of a mass analyzer and an ion detector. The ion detector in most cases is an electron multiplier, or, for direct observation, a phosphor coated screen. As discussed above, there are three main types of mass analyzers used in modern SIMS systems.

The quadrupole mass analyzer consists of four symmetric rods, connected together with two opposite pairs. Each pair of rods is held at a d.c. bias with an oscillating r.f. (a.c.) voltage superimposed on them. An equal but opposite voltage is applied to the other pair. As the secondary ions enter the pass analyzer, they undergo unstable oscillations due to the electric fields from the two pairs of rods. Only secondary ions with a specific mass/charge ratio can pass through the analyzer tube with a periodic but stable trajectory of limited amplitude while the other ions will hit one of the rods and be annihilated. This resonant condition and therefore mass selection is dependent only on the voltages applied to the rods; thus, rapid switching between

different masses is readily achieved. In practice, up to 16 different masses can be detected for a single run with the quadrupole mass SIMS system at Evans Analytical Group. While mass switching and detection is fast in this type of mass analyzer, the mass resolving power or mass resolution, defined by m/Δm, is often very low. This implies that, while many species can be detected in the same run, it is difficult to discern species very close in mass (e.g., ^{31}P and ^{30}Si + ^{1}H). This presents a problem for our As in SiGe samples as the mass of ^{75}As (74.9216 amu) and ^{74}Ge+H (74.9290 amu) only differ by about 0.01%. As a result, the detection limit in concentration using this mass analyzer is only around 10^{17} cm^{-3}. Better mass resolution and therefore better detection limit can be achieved with a magnetic sector SIMS system.

The magnetic sector mass analyzer utilizes the Lorentz force on a moving charged ion traveling through a magnetic field. The force acting on a moving charged ion is orthogonal to both the magnetic field direction and the direction of motion, resulting in a circular trajectory. The radius, R, of this circular path depends on the velocity, therefore, the mass/charge ratio, of the charged species. The radius can be described by:

$$R = \frac{1}{B}\left(\frac{2mV}{z}\right)^{1/2} \qquad\qquad (B.1)$$

where B is the magnitude of the magnetic field, V is the accelerating potential for the ions, and m/z is the mass/charge ratio. Figure B.2 below schematically shows the mechanism of magnetic sector mass analyzer separating the mass of different ions. In theory, all the separated mass can be detected. In practice, however, only ions with a specific mass are detected by allowing the ions through an aperture to reach the detector. In order to detect ions of different masses, sequential magnetic field switching is required. This substantially slows the detection process, resulting in only one specific mass is detected for one experimental run. The major advantage for this mass analyzer is the unsurpassed mass resolution. The mass resolving power is generally higher than 10^4, making the mass analyzer ideal for distinguishing ions such as ^{75}As and ^{74}Ge+H. For our work, the magnetic sector SIMS runs were performed at Evans Analytical Group on some of the As in SiGe samples with As concentrations below 10^{16} cm^{-3}.
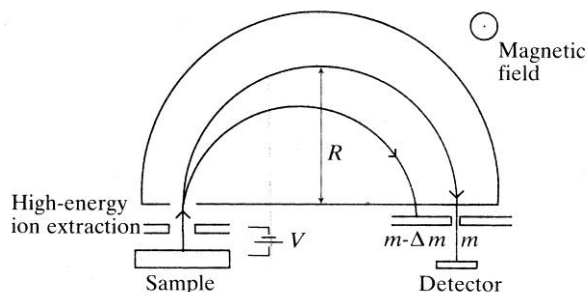
Figure B.2 A schematic showing the mass separation process of a magnetic sector mass analyzer. With magnetic field coming out of the page, only ions accelerated by voltage V with mass m can pass through the aperture and be detected.

Finally, the time-of-flight (TOF) mass analyzer functions by the fact that the ions with different masses travel at different velocities when they are accelerated by the same potential. If these ions then pass through a field-free region, they will spread out in time, with heavier ions arriving later than lighter ions. The transit time, or the time-of-flight, t, can be expressed as:

$$t = L \left(\frac{m}{2zV} \right)^{1/2} \qquad \text{(B.2)}$$

Here, L is the length of the flight path in the field-free zone, V is the accelerating voltage and m/z is, again, the mass/charge ratio. Instead of continuous sputtering by an ion beam, in TOF-SIMS the incident primary ions are pulsed. The samples are sputtered in a brief burst and the time of these secondary ions to traverse to the detector is measured. One major advantage of this method is the absence of narrow apertures in which ions have to pass through to be collected as in the case of quadrupole and magnetic sector methods. This allows 50-100% of the ions to be collected in one pulse. As a result, the primary ion current can be greatly reduced, making the method ideal for sensitive surface analysis in the static SIMS mode. More recently, TOF-SIMS is also used in the dynamic mode to obtain depth profiles. Another added advantage for the method is that all the species, regardless of the mass, are detected at once. The raw data usually consist of the time-of-flight information for all species, resulting in data files close to terabytes range [127]. This way, all the information are contained and can be processed at a later time.

In summary, different mass analyzers have their distinct advantages and drawbacks. The quadrupole mass analyzers are usually cheaper to operate, fast, and capable of detecting multiple species at the same time. However, they have limited mass resolution and detectable mass range. The magnetic sector mass analyzers have extremely high mass resolution and are capable at detecting masses of molecules higher than 10^4 amu, but, they are slow in switching between detecting different masses. The time-of-flight system offers the advantage of detecting all species at once with low primary ion current. However, the mass sensitivity is a bit lower than the magnetic sector system. Table B.1 summarizes the different aspects of the different mass

analyzers. A comparison with different commercially available SIMS systems are summarized in ref. [127].

Table B.1 Comparison of mass analyzers for SIMS. From ref. [125].

Type	Mass Resolution	Mass Range (amu)	Transmission (%)	Mass Detection
Quadrupole	100-1000	<1000	1-10	Sequential
Magnetic sector	10000	>10000	10-50	Sequential
Time-of-flight	>1000	1000-10000	50-100	Parallel

References

[1]   E. E. Haller, "Germanium: From its discovery to SiGe devices," *Materials Science in Semiconductor Processing,* vol. 9, pp. 408-422, 2006.

[2]   R. W. Cahn, "The science of dirt," *Nature Materials,* vol. 1, pp. 3-4, 2002.

[3]   F. Seitz, "Research on Silicon and Germanium in World War II," *Physics Today,* vol. 48, pp. 22-27, 1995.

[4]   J. Bardeen and W. H. Brattain, "The Transistor, A Semi-Conductor Triode," *Physical Review,* vol. 74, p. 230, 1948.

[5]   W. Shockley, "Circuit element utilizing semiconductive material," US Patent, 1948.

[6]   G. K. Teal*, et al.*, "Growth of Germanium Single Crystals Containing p-n Junctions," *Physical Review,* vol. 81, p. 637, 1951.

[7]   G. K. Teal and E. Buehler, "Single-Crystal Germanium," *Proceedings of the IRE,* vol. 40, pp. 906-909, 1952.

[8]   J. S. Kilby, "Invention of the integrated circuit," *Electron Devices, IEEE Transactions on,* vol. 23, pp. 648-654, 1976.

[9]   R. N. Noyce, "Semiconductor device and lead structure," US Patent, 1961.

[10]   R. F. Pierret, *Semiconductor device fundamentals*. Reading, Mass.: Addison-Wesley, 1996.

[11]   D. A. Antoniadis*, et al.*, "Continuous MOSFET performance increase with device scaling: the role of strain and channel material innovations," *IBM Journal of Research and Development,* vol. 50, pp. 363-76, 2006.

[12]   K. C. Saraswat*, et al.*, "High Mobility Materials and Novel Device Structures for High Performance Nanoscale MOSFETs," in *Electron Devices Meeting, 2006. IEDM '06. International*, 2006, pp. 1-4.

[13]   *International Technology Roadmap for Semiconductors*, 2009.

[14]   C. Claeys*, et al.*, "Si versus Ge for future microelectronics," *Thin Solid Films,* vol. 518, pp. 2301-2306, 2010.

[15]   S. Thompson*, et al.*, "MOS Scaling: Transistor Challenges for the 21st Century," *Intel Technology Journal,* vol. 2, 1998.

[16]   E. P. Gusev*, et al.*, "Ultrathin high-K gate stacks for advanced CMOS devices," in *Electron Devices Meeting, 2001. IEDM Technical Digest. International*, 2001, pp. 20.1.1-20.1.4.

[17]   J. C. Lee*, et al.*, "High-k dielectrics and MOSFET characteristics," in *Electron Devices Meeting, 2003. IEDM '03 Technical Digest. IEEE International*, 2003, pp. 4.4.1-4.4.4.

[18]   M. V. Fischetti*, et al.*, "Effective electron mobility in Si inversion layers in metal-oxide-semiconductor systems with a high-kappa insulator: The role of remote phonon scattering," *Journal of Applied Physics,* vol. 90, pp. 4587-4608, 2001.

[19]   S. Datta*, et al.*, "High mobility Si/SiGe strained channel MOS transistors with HfO_2/TiN gate stack," in *Electron Devices Meeting, 2003. IEDM '03 Technical Digest. IEEE International*, 2003, pp. 28.1.1-28.1.4.

[20]   M. L. Lee*, et al.*, "Strained Si, SiGe, and Ge channels for high-mobility metal-oxide-semiconductor field-effect transistors," *Journal of Applied Physics,* vol. 97, p. 011101, 2005.

[21]   C. K. Maiti and et al., "Strained-Si heterostructure field effect transistors," *Semiconductor Science and Technology,* vol. 13, p. 1225, 1998.

[22]   G. Abstreiter, *et al.*, "Strain-Induced Two-Dimensional Electron Gas in Selectively Doped Si/Si$_x$Ge$_{1-x}$ Superlattices," *Physical Review Letters,* vol. 54, p. 2441, 1985.

[23]   E. A. Fitzgerald, *et al.*, "Relaxed Ge$_x$Si$_{1-x}$ structures for III--V integration with Si and high mobility two-dimensional electron gases in Si," 1992, pp. 1807-1819.

[24]   F. Schaffler and et al., "High-electron-mobility Si/SiGe heterostructures: influence of the relaxed SiGe buffer layer," *Semiconductor Science and Technology,* vol. 7, p. 260, 1992.

[25]   J. Welser, *et al.*, "NMOS and PMOS transistors fabricated in strained silicon/relaxed silicon-germanium structures," in *Electron Devices Meeting, 1992. Technical Digest., International*, 1992, pp. 1000-1002.

[26]   J. Welser, *et al.*, "Electron mobility enhancement in strained-Si n-type metal-oxide-semiconductor field-effect transistors," *Electron Device Letters, IEEE,* vol. 15, pp. 100-102, 1994.

[27]   D. K. Nayak, *et al.*, "High-mobility p-channel metal-oxide-semiconductor field-effect transistor on strained Si," *Applied Physics Letters,* vol. 62, pp. 2853-2855, 1993.

[28]   D. K. Nayak and S. K. Chun, "Low-field hole mobility of strained Si on (100) Si$_{1-x}$Ge$_x$ substrate," *Applied Physics Letters,* vol. 64, pp. 2514-2516, 1994.

[29]   D. K. Nayak, *et al.*, "High-mobility strained-Si PMOSFET's," *Electron Devices, IEEE Transactions on,* vol. 43, pp. 1709-1716, 1996.

[30]   K. Rim, *et al.*, "Characteristics and device design of sub-100 nm strained Si N- and PMOSFETs," in *VLSI Technology, 2002. Digest of Technical Papers. 2002 Symposium on*, 2002, pp. 98-99.

[31]   Y. Sun, *et al.*, "Physics of strain effects in semiconductors and metal-oxide-semiconductor field-effect transistors," *Journal of Applied Physics,* vol. 101, pp. 104503-22, 2007.

[32]   S. Thompson, *et al.*, "A 90 nm logic technology featuring 50 nm strained silicon channel transistors, 7 layers of Cu interconnects, low k ILD, and 1 mm^2 SRAM cell," in *Electron Devices Meeting, 2002. IEDM '02. Digest. International*, 2002, pp. 61-64.

[33]   S. E. Thompson, *et al.*, "A logic nanotechnology featuring strained-silicon," *Electron Device Letters, IEEE,* vol. 25, pp. 191-193, 2004.

[34]   C. L. Claeys and E. Simoen, *Germanium-based technologies from materials to devices*. Amsterdam; London: Elsevier, 2007.

[35]   A. K. Okyay, *et al.*, "High-efficiency metal-semiconductor-metal photodetectors on heteroepitaxially grown Ge on Si," *Opt. Lett.,* vol. 31, pp. 2565-2567, 2006.

[36]   K. Kita, *et al.*, "Growth mechanism difference of sputtered HfO$_2$ on Ge and on Si," *Applied Physics Letters,* vol. 85, pp. 52-54, 2004.

[37]   S. W. Bedell, *et al.*, "Mobility Scaling in Short-Channel Length Strained Ge-on-Insulator P-MOSFETs," *Electron Device Letters, IEEE,* vol. 29, pp. 811-813, 2008.

[38]   T. Krishnamohan and K. Saraswat, "High mobility Ge and III-V materials and novel device structures for high performance nanoscale MOSFETS," in *Solid-State Device Research Conference, 2008. ESSDERC 2008. 38th European*, 2008, pp. 38-46.

[39]   J. Mitard, *et al.*, "Record I$_{ON}$/I$_{OFF}$ performance for 65nm Ge pMOSFET and novel Si passivation scheme for improved EOT scalability," in *Electron Devices Meeting, 2008. IEDM 2008. IEEE International*, 2008, pp. 1-4.

[40]   L. Hutin, *et al.*, "GeOI pMOSFETs Scaled Down to 30-nm Gate Length With Record Off-State Current," *Electron Device Letters, IEEE,* vol. 31, pp. 234-236, 2010.

[41]   S. Brotzmann and H. Bracht, "Intrinsic and extrinsic diffusion of phosphorus, arsenic, and antimony in germanium," *Journal of Applied Physics,* vol. 103, pp. 033508-7, 2008.

[42]   H. Bracht*, et al.*, "Interstitial-Mediated Diffusion in Germanium under Proton Irradiation," *Physical Review Letters,* vol. 103, p. 255501, 2009.

[43]   E. Simoen*, et al.*, "Source/Drain junction integration issues in submicron Ge MOSFETs," in *Solid-State and Integrated-Circuit Technology, 2008. ICSICT 2008. 9th International Conference on*, 2008, pp. 211-214.

[44]   H. Bracht, "Self- and foreign-atom diffusion in semiconductor isotope heterostructures. I. Continuum theoretical calculations," *Physical Review B,* vol. 75, p. 035210, 2007.

[45]   A. Fick, "On liquid diffusion," *Philosophical Magazine Series 4,* vol. 10, pp. 30 - 39, 1855.

[46]   T. N. Narasimhan, "Fourier's Heat Conduction Equation: History, Influence, and Connections," *Rev. Geophys.,* vol. 37, pp. 151-172, 1999.

[47]   H. H. Silvestri, "Diffusion in Silicon Isotope Heterostructures," Ph.D. Dissertation, Materials Science and Engineering, University of California at Berkeley, Berkeley, CA USA, 2004.

[48]   E. R. Weber, "Transition metals in silicon," *Applied Physics A: Materials Science & Processing,* vol. 30, pp. 1-22, 1983.

[49]   E. E. Haller, "Isotopically engineered semiconductors," *Journal of Applied Physics,* vol. 77, pp. 2857-2878, 1995.

[50]   H. A. Bracht*, et al.*, "Advanced diffusion studies with isotopically controlled materials," *Solid State Communications,* vol. 133, pp. 727-735, 2005.

[51]   H. Bracht*, et al.*, "Self- and foreign-atom diffusion in semiconductor isotope heterostructures. II. Experimental results for silicon," *Physical Review B,* vol. 75, p. 035211, 2007.

[52]   A. Seeger and K. P. Chik, "Diffusion Mechanisms and Point Defects in Silicon and Germanium," *physica status solidi (b),* vol. 29, pp. 455-542, 1968.

[53]   D. Shaw, "Self- and impurity diffusion in Ge and Si," *physica status solidi (b),* vol. 72, pp. 11-39, 1975.

[54]   K. Compaan and Y. Haven, "Correlation factors for diffusion in solids," *Transactions of the Faraday Society,* vol. 52, pp. 786-801, 1956.

[55]   K. Compaan and Y. Haven, "Correlation factors for diffusion in solids 2: indirect interstitial mechanism," *Transactions of the Faraday Society,* vol. 54, pp. 1498-1508, 1958.

[56]   G. D. Watkins, in *Deep centers in semiconductors : a state of the art approach*, S. T. Pantelides, Ed., ed New York: Gordon and Breach, 1986, p. 147.

[57]   H. Bracht, "Fast metal diffusion in silicon under intrinsic and extrinsic doping conditions," *Defect and Diffusion Forum,* vol. 143, pp. 979-991, 1997.

[58]   H. Haesslein*, et al.*, "Vacancies and Self-Interstitials in Germanium Observed by Perturbed Angular Correlation Spectroscopy," *Physical Review Letters,* vol. 80, p. 2626, 1998.

[59]   C. Y. Liao, "Neutron Transmutation Doping of Isotopically Enriched Silicon," M.S. Thesis, Department of Materials Science and Engineering, University of California, Berkeley, CA USA, 2006.

[60]   T. D. Ladd*, et al.*, "All-Silicon Quantum Computer," *Physical Review Letters,* vol. 89, p. 017901, 2002.

[61]	K. M. Itoh, "An all-silicon linear chain NMR quantum computer," *Solid State Communications,* vol. 133, pp. 747-752, 2005.

[62]	H. Hayashi*, et al.*, "Dynamic nuclear polarization of ^{29}Si nuclei in isotopically controlled phosphorus doped silicon," *Physical Review B,* vol. 80, p. 045201, 2009.

[63]	B. E. Kane, "A silicon-based nuclear spin quantum computer," *Nature,* vol. 393, pp. 133-137, 1998.

[64]	H. D. Fuchs*, et al.*, "Germanium ^{70}Ge/^{74}Ge isotope heterostructures: an approach to self-diffusion studies," *Physical Review B-Condensed Matter,* vol. 51, pp. 16817-21, 1995.

[65]	L. Wang*, et al.*, "Gallium self-diffusion in gallium phosphide," *Applied Physics Letters,* vol. 70, pp. 1831-1833, 1997.

[66]	H. Bracht*, et al.*, "Enhanced and retarded Ga self-diffusion in Si and Be doped GaAs isotope heterostructures," *Solid State Communications,* vol. 112, pp. 301-314, 1999.

[67]	H. Bracht*, et al.*, "Self-diffusion in ^{69}Ga^{121}Sb/^{71}Ga^{123}Sb isotope heterostructures," *Journal of Applied Physics,* vol. 89, pp. 5393-5399, 2001.

[68]	P. M. Fahey*, et al.*, "Point defects and dopant diffusion in silicon," *Reviews of Modern Physics,* vol. 61, p. 289, 1989.

[69]	H. H. Silvestri*, et al.*, "Diffusion of silicon in crystalline germanium," *Semiconductor Science and Technology,* vol. 21, pp. 758-62, 2006.

[70]	A. Carvalho*, et al.*, "Self-Interstitial in Germanium," *Physical Review Letters,* vol. 99, p. 175502, 2007.

[71]	J. Vanhellemont*, et al.*, "On the solubility and diffusivity of the intrinsic point defects in germanium," *Journal of Applied Physics,* vol. 101, pp. 036103-3, 2007.

[72]	T. Soma*, et al.*, "Stable Configuration of an Interstitial Atom with Relaxation Effect in Si and Ge," *physica status solidi (b),* vol. 149, pp. 477-482, 1988.

[73]	J. C. Bourgoin and M. Lannoo, "On self-diffusion in silicon and germanium," *Radiation Effects,* vol. 46, pp. 157-161, 1980 1980.

[74]	D. J. Eaglesham*, et al.*, "Implantation and transient B diffusion in Si: The source of the interstitials," *Applied Physics Letters,* vol. 65, pp. 2305-2307, 1994.

[75]	S. C. Jain*, et al.*, "Transient enhanced diffusion of boron in Si," *Journal of Applied Physics,* vol. 91, pp. 8919-8941, 2002.

[76]	H. J. Gossmann*, et al.*, "Oxidation enhanced diffusion in Si B-doping superlattices and Si self-interstitial diffusivities," *Applied Physics Letters,* vol. 63, pp. 639-641, 1993.

[77]	E. Simoen*, et al.*, "Ion-implantation issues in the formation of shallow junctions in germanium," *Materials Science in Semiconductor Processing,* vol. 9, pp. 634-639, 2006.

[78]	S. Uppal*, et al.*, "Diffusion of boron in germanium at 800-900°C," *Journal of Applied Physics,* vol. 96, pp. 1376-1380, 2004.

[79]	M. Posselt*, et al.*, "P implantation into preamorphized germanium and subsequent annealing: Solid phase epitaxial regrowth, P diffusion, and activation," in *International Workshop on Insight in Semiconductor Device Fabrication, Metrology and Modeling (Insight 2007)*, Napa, California, 2008, pp. 430-434.

[80]	D. Alloyeau*, et al.*, "Atomic-resolution three-dimensional imaging of germanium self-interstitials near a surface: Aberration-corrected transmission electron microscopy," *Physical Review B,* vol. 80, pp. 014114-6, 2009.

[81]	J. F. Ziegler*, et al.*, "The Stopping and Range of Ions in Solids," SRIM-2010 ed. New York: Pergamon, 1985.

[82]   D. J. Paul, "Si/SiGe heterostructures: from material and physics to devices and circuits," *Semiconductor Science and Technology,* vol. 19, pp. R75-R108, 2004.

[83]   J. D. Cressler, "SiGe HBT technology: a new contender for Si-based RF and microwave circuit applications," *Microwave Theory and Techniques, IEEE Transactions on,* vol. 46, pp. 572-589, 1998.

[84]   J. Jongwan*, et al.*, "Implementation of both high-hole and electron mobility in strained Si/strained $Si_{1-y}Ge_y$ on relaxed $Si_{1-x}Ge_x$ (x<y) virtual substrate," *Electron Device Letters, IEEE,* vol. 24, pp. 460-462, 2003.

[85]   P. Kuo*, et al.*, "Comparison of boron diffusion in Si and strained Si[sub 1 - x]Ge[sub x] epitaxial layers," *Applied Physics Letters,* vol. 62, pp. 612-614, 1993.

[86]   N. Moriya*, et al.*, "Boron diffusion in strained $Si_{1-x}Ge_x$ epitaxial layers," *Physical Review Letters,* vol. 71, p. 883, 1993.

[87]   S. Eguchi*, et al.*, "Germanium-concentration dependence of arsenic diffusion in silicon germanium alloys," *Applied Physics Letters,* vol. 84, pp. 368-370, 2004.

[88]   S. Eguchi*, et al.*, "Comparison of arsenic and phosphorus diffusion behavior in silicon-germanium alloys," *Applied Physics Letters,* vol. 80, pp. 1743-5, 2002.

[89]   V. S. Tishkov*, et al.*, "Rapid thermal annealing of arsenic-implanted $Si_{0.6}Ge_{0.4}$ alloys: Temperature effects," *Applied Physics Letters,* vol. 68, pp. 655-657, 1996.

[90]   A. Nylandsted Larsen*, et al.*, "Rapid thermal annealing of arsenic implanted relaxed $Si_{1-x}Ge_x$," *Nuclear Instruments and Methods in Physics Research Section B: Beam Interactions with Materials and Atoms,* vol. 120, pp. 161-164, 1996.

[91]   P. Laitinen*, et al.*, "Arsenic diffusion in relaxed $Si_{1-x}Ge_x$," *Physical Review B-Condensed Matter,* vol. 68, pp. 155209-1-6, 2003.

[92]   A. Strohm*, et al.*, "Self-diffusion of [71]Ge in Si-Ge," *Physica B: Condensed Matter,* vol. 308-310, pp. 542-545, 2001.

[93]   N. R. Zangenberg*, et al.*, "Ge Self-Diffusion in Epitaxial $Si_{1-x}Ge_x$ Layers," *Physical Review Letters,* vol. 87, p. 125901, 2001.

[94]   P. Laitinen*, et al.*, "Self-Diffusion of [31]Si and [72]Ge in Relaxed $Si_{0.20}Ge_{0.80}$ Layers," *Physical Review Letters,* vol. 89, p. 085902, 2002.

[95]   R. Kube*, et al.*, "Simultaneous diffusion of Si and Ge in isotopically controlled $Si_{1-x}Ge_x$ heterostructures," *Materials Science in Semiconductor Processing,* vol. 11, pp. 378-383, 2008.

[96]   H. Bracht*, et al.*, "Silicon Self-Diffusion in Isotope Heterostructures," *Physical Review Letters,* vol. 81, p. 393, 1998.

[97]   A. Chroneos*, et al.*, "Vacancy-arsenic clusters in germanium," *Applied Physics Letters,* vol. 91, p. 192106, 2007.

[98]   A. Chroneos*, et al.*, "Atomic scale simulations of donor–vacancy pairs in germanium," *Journal of Materials Science: Materials in Electronics,* vol. 18, pp. 763-768, 2007.

[99]   M. Naganawa*, et al.*, "Charge states of vacancies in germanium investigated by simultaneous observation of germanium self-diffusion and arsenic diffusion," *Applied Physics Letters,* vol. 93, pp. 191905-3, 2008.

[100] S. Brotzmann*, et al.*, "Diffusion and defect reactions between donors, C, and vacancies in Ge. I. Experimental results," *Physical Review B,* vol. 77, p. 235207, 2008.

[101] M. Werner*, et al.*, "Effect of hydrostatic pressure, temperature, and doping on self-diffusion in germanium," *Physical Review B,* vol. 32, p. 3930, 1985.

[102] N. A. Stolwijk and H. Bracht, Eds., *Diffusion in Silicon, Germanium and Their Alloys* (Landolt-Börnstein New Series Vol. III/33 A). New York: Sringer, 1998,

[103] R. Kube*, et al.*, "Intrinsic and extrinsic diffusion of indium in germanium," *Journal of Applied Physics,* vol. 106, pp. 063534-7, 2009.

[104] E. Vainonen-Ahlgren*, et al.*, "Identification of vacancy charge states in diffusion of arsenic in germanium," *Applied Physics Letters,* vol. 77, pp. 690-692, 2000.

[105] I. Riihimaki*, et al.*, "Vacancy-impurity complexes and diffusion of Ga and Sn in intrinsic and p-doped germanium," *Applied Physics Letters,* vol. 91, pp. 091922-3, 2007.

[106] H. Bracht, "Copper related diffusion phenomena in germanium and silicon," *Materials Science in Semiconductor Processing,* vol. 7, pp. 113-124, 2004.

[107] H. Bracht and S. Brotzmann, "Atomic transport in germanium and the mechanism of arsenic diffusion," *Materials Science in Semiconductor Processing,* vol. 9, pp. 471-476, 2006.

[108] H. Bracht*, et al.*, "Properties of intrinsic point defects in silicon determined by zinc diffusion experiments under nonequilibrium conditions," *Physical Review B,* vol. 52, p. 16542, 1995.

[109] A. Chroneos, "Dopant-vacancy cluster formation in germanium," *Journal of Applied Physics,* vol. 107, pp. 076102-3, 2010.

[110] P. Dorner*, et al.*, "Sims-untersuchungen zur volumendiffusion von Al in Ge," *Acta Metallurgica,* vol. 30, pp. 941-946, 1982.

[111] H. H. Silvestri and et al., "Diffusion of silicon in crystalline germanium," *Semiconductor Science and Technology,* vol. 21, p. 758, 2006.

[112] H. D. Fuchs*, et al.*, "Germanium ^{70}Ge/^{74}Ge isotope heterostructures: An approach to self-diffusion studies," *Physical Review B,* vol. 51, p. 16817, 1995.

[113] P. Delugas and V. Fiorentini, "Energetics of transient enhanced diffusion of boron in Ge and SiGe," *Physical Review B,* vol. 69, p. 085203, 2004.

[114] C. Janke*, et al.*, "Ab initio investigation of boron diffusion paths in germanium," *Physical Review B,* vol. 77, pp. 075208-6, 2008.

[115] A. Satta*, et al.*, "Shallow Junction Ion Implantation in Ge and Associated Defect Control," *Journal of The Electrochemical Society,* vol. 153, pp. G229-G233, 2006.

[116] M. Posselt*, et al.*, "P implantation into preamorphized germanium and subsequent annealing: Solid phase epitaxial regrowth, P diffusion, and activation," Napa, California, 2008, pp. 430-434.

[117] H. Bracht*, et al.*, "Radiation Enhanced Silicon Self-Diffusion and the Silicon Vacancy at High Temperatures," *Physical Review Letters,* vol. 91, p. 245502, 2003.

[118] S. Schneider*, et al.*, "Proton irradiation of germanium isotope multilayer structures at elevated temperatures," *Journal of Applied Physics,* vol. 103, pp. 033517-5, 2008.

[119] E. Bruno*, et al.*, "Mechanism of B diffusion in crystalline Ge under proton irradiation," *Physical Review B,* vol. 80, pp. 033204-4, 2009.

[120] W. Jungling*, et al.*, "Simulation of critical IC fabrication processes using advanced physical and numerical methods," *Electron Devices, IEEE Transactions on,* vol. 32, pp. 156-167, 1985.

[121] A. Chroneos*, et al.*, "Nonlinear stability of E centers in $Si_{1-x} Ge_x$: Electronic structure calculations," *Physical Review B,* vol. 78, p. 195201, 2008.

[122] R. Olesinski and G. Abbaschian, "The C−Ge (Carbon-Germanium) system," *Journal of Phase Equilibria,* vol. 5, pp. 484-486, 1984.

[123] S. Koffel, *et al.*, "End of range defects in Ge," *Journal of Applied Physics,* vol. 105, pp. 126110-3, 2009.

[124] J. C. Vickerman*, et al.*, *Secondary ion mass spectrometry : principles and applications*. Oxford, New York: Clarendon Press; Oxford University Press, 1989.

[125] J. C. Vickerman*, et al.*, *ToF-SIMS : surface analysis by mass spectrometry*. Chichester: IM, 2001.

[126] D. K. Schroder, *Semiconductor material and device characterization*, 3rd ed ed. [Piscataway, NJ]; Hoboken, N.J.: IEEE Press; Wiley, 2006.

[127] J. Griffiths, "Secondary Ion Mass Spectrometry," *Analytical Chemistry,* vol. 80, pp. 7194-7197, 2008.